A Boundary Integral Method for Modeling Axisymmetric Flow Around a Rising Bubble in a Vertical Tube and Accurate Numerical Evaluation of Orthogonal Polynomials

by

Yanhe Huang

A dissertation submitted in partial satisfaction of the

requirements for the degree of

Doctor of Philosophy

in

Mathematics

in the

Graduate Division

of the

University of California, Berkeley

Committee in charge:

Professor Jon Wilkening, Chair
Professor Richard Bamler
Professor Panayiotis Papadopoulos

Fall 2020

A Boundary Integral Method for Modeling Axisymmetric Flow Around a Rising Bubble in a Vertical Tube and Accurate Numerical Evaluation of Orthogonal Polynomials

Abstract

A Boundary Integral Method for Modeling Axisymmetric Flow Around a Rising Bubble in a Vertical Tube and Accurate Numerical Evaluation of Orthogonal Polynomials

by

Yanhe Huang

Doctor of Philosophy in Mathematics

University of California, Berkeley

Professor Jon Wilkening, Chair

Axisymmetric flow around a bubble rising in a 3D fluid has been studied intensively both numerically and experimentally over the years, but in the high Reynolds number regime, no matter for small oblate or elongated bubbles, current mathematical models face problems such as introducing an unnecessary singularity at the stagnation point, missing proper lower boundary conditions, and solving with low order finite difference methods, which leads to large numerical errors. Modeling the problem by both potential flow and viscous potential flow, we can represent the velocity potential using layer potentials and compute the bubble shape with spectral accuracy, with average numerical errors around 10^{-9}. A dimensionless inviscid model is first built to study steady flow around a bubble in an infinitely long tube in the case of zero gravity. With a comprehensive discussion on parametrization, singular integrals, and numerical quadrature, we solve both oblate and elongated bubble shapes accurately and find different solution branches of bubble shapes characterized by the number of humps. These solution branches relating the Weber number and cross-section arc-length suggest that for any nonzero surface tension, there exists a countably infinite number of solutions. When there is gravity, kinematic viscosity is introduced to balance out the normal stress on the bubble surface. Different shapes of steadily rising bubbles under different Froude numbers are presented.

We also study the corresponding time-dependent problem to illustrate the dynamics of unsteady bubbles, both small and elongated, and to confirm the non-existence of steadily rising bubbles in the inviscid model with nonzero gravity. The approximation of dipole density by spherical harmonics is computed to remove the hyper-singularity in the normal derivatives of the double layer potential on the bubble surface.

Due to the importance of accurate evaluation of orthogonal polynomials in the boundary integral method, we introduce a new way to evaluate orthogonal polynomials more accurately near the endpoints of the integration interval by evaluating a newly created set of associated orthogonal polynomials at corresponding points. Various ways to evaluate the associated orthogonal polynomials are discussed and implemented. Among them, the best method can

achieve round-off error accuracy even for end-point evaluation of generic high-degree Jacobi polynomials and generalized Laguerre polynomials, which is 3 digits more accurate than the classic recurrence method in double precision when the degree is around 400. Based on the accurate evaluation, we perform one iteration of Newton's method to achieve more accurate quadrature abscissas near endpoints. We also calculate quadrature weights using the Christoffel formula based on our accurate evaluation. The resulting errors in abscissas and weights are compared to those of the Golub-Welsch algorithm, with our method being more accurate. Strategies on generic weight functions are given and tested on Maxwell polynomials of current interest in plasma physics.

To Mom, Dad and Chuanhong

Contents

Contents **ii**

List of Figures **iv**

1 Introduction **1**
1.1 Single axisymmetric bubble rising in an infinitely long vertical tube in 3D . . 1
1.2 Accurate evaluation of orthogonal polynomials near endpoints of the integration interval 3

2 Single axisymmetric bubble rising steadily in an infinitely long vertical tube in 3D **5**
2.1 Mathematical formulation 5
2.2 Non-dimensionalization 7
2.3 Potential theory 8
2.4 Representing the steady velocity potential using a single layer potential . . . 11
2.5 Solvability of the integral equation 12
2.6 Two parametrizations: radial and HLS 13
2.7 Analyzing the singularities 18

3 Numerical procedure and results **21**
3.1 Numerical discretization and integration 21
3.2 Numerical procedure 24
3.3 Numerical solution branches 26
3.4 Time complexity and parallel computing 31

4 The viscous model **32**
4.1 Introduction 32
4.2 Mathematical formulation 32
4.3 Numerical solution 34

5 Time-dependent problem **36**
5.1 Mathematical set up 36
5.2 Representing the solution using single and double layer potentials 37

5.3 Hyper-singularity removal and singularity analysis 39
5.4 Evolution under HLS framework 41
5.5 Numerical computation 43
5.6 Numerical results 47

6 Accurate evaluation of orthogonal polynomials near endpoints of the integration interval 49
6.1 Preliminaries 49
6.2 An associated family of orthogonal polynomials 51
6.3 Connections with continued fractions 55
6.4 Numerical results 57
6.5 Amplification factor analysis 65

7 Conclusion and future work 67

Bibliography 69

List of Figures

2.1 Set up of the (dimensionless) problem in (x, y, z) space 6
2.2 Two ways to parametrize the bubble surface, the radial angle (left) and the HLS framework (right) in a case where radial parametrization breaks down. 14

3.1 Transforming any point $q \in S_2$ to its angle representation τ. 22
3.2 $\mu_1(\alpha)$ with $\alpha \in [0, \pi]$ on a round bubble of radius 0.9 and $\mu_2(\tau)$ with $\tau \in [0, \pi]$ on the infinite tube solved with $N = M = 120$ when Neumann conditions are satisfied on S_1 and S_2. 24
3.3 The right-hand side cross-sectional profile curve of a steadily rising bubble with one (top left), two (bottom left), and three (right) humps. The infinitely long tube wall is always placed at $x = 1$ and the far-field background flow is normalized to $U = -1$. 27
3.4 The magnitude of even Fourier modes $|c_{2n}|$ of $\tilde{\theta}(\alpha)$ with $2n$ the even frequency versus n in the no gravity case. Each relation corresponds to one representative from each solution branch, i.e. $\sigma = 0.5$ from the one hump case, and $\sigma = 1.0$ from the cases with two and three humps. 28
3.5 Three solution branches of different bubble shapes(1, 2, and 3 humps) relating σ and W obtained from numerical continuation. 29
3.6 Comparison of steadily rising bubbles shapes with or without wall at $x = 1$. . . 30

4.1 Right-hand cross-sectional profile of a steadily rising bubble for several values of the Froude number F (left) and the decay of Fourier modes $|c_n|$ $(1 \leq n \leq 198)$ of $\tilde{\theta}(\alpha)$ when $F = 14.14$ with $N = 200$ and $M = 120$ (right). 34

5.1 Two horizontal tangent points q_1 and q_2 characterized by vanishing tangential angle. 44
5.2 Dynamics of the profile curve of a round bubble of radius 0.9 with $F = 1.0$ and $W = 12.3115$ (left) and the displacement of the front stagnation point (right). . 47
5.3 Dynamics of the profile curve of steadily rising bubbles with two humps from the no gravity case under the condition $F = 1.0$ and $\sigma = 0.5$ (left) and the displacement of the front stagnation point (right). 48

6.1 Evaluation error of $P_n^{(-0.5,0.5)}$, $P_n^{(1,2)}$ and $P_n^{(1.7,2.1)}$ using the classic, improved, hybrid quadruple/double, and analytic formula methods; and accuracy of $\tilde{b}_n$ used in the improved and analytic formula methods. 61
6.2 Error in calculating quadrature grids and weights of Jacobi type with $\alpha = 0.5$, $\beta = -0.5$ (first column) and $\alpha = 1.7$, $\beta = 2.1$ (second column). 62
6.3 Evaluation error of $L_n^2(x)$ and $L_n^{2.1}(x)$ using the classic, improved, hybrid and analytic formula methods. 63
6.4 Error of quadrature abscissas and weights for the generalized Laguerre case $\alpha = 2.1$ using classic and analytic formula methods. 64
6.5 Evaluation error of Maxwell polynomial $\varphi_n(x)$ using 4 methods(left). Quadrature abscissas(middle) and weights(right) error using 'direct calculation method' and 'Golub-Welsch'. 65
6.6 Amplification factors of Jacobi polynomial in the $(\alpha, \beta) = (1.7, 2.1)$ case with $n = 8$, 64, 512 and $y \in [-1, -0.5]$ obtained from the old and the new methods. . 66

Acknowledgments

I would like to express my deepest gratitude to my advisor Jon Wilkening for introducing fascinating topics and sharing his large code base with me. He is not only a supervisor that is cheerful, knowledgable, creative, and full of spirit but also a versatile and considerate friend. I continue to learn from his mathematical ideas and numerical techniques in the weekly meeting. Without his support, inspiration, and encouragement, none of the work detailed below could have been done.

I am also grateful to Richard Bamler for his inspiring differential geometry lectures and valuable kind advice on graduate study and research throughout the years. Thanks to Panayiotis Papadopoulos for graciously spending time with this work. Thanks to Daniel Tataru for giving superb lectures on different topics of PDE; Per-Olof Persson for introducing different numerical methods for solving PDEs to me; John Lott, Mark Haiman and Marc Rieffel for opening up my horizon in algebra, geometry, and combinatorics during my first year at Berkeley; Will Filthian, James Demmel and Kathy Yelick for sharing knowledge outside the math department with me. It is through all your lectures and projects that I gain knowledge and build up confidence day by day.

I would also like to thank my friends at Berkeley for making my Ph.D. life such a special journey to me. Thanks to my academic brother and sister Rocky Foster and Xinyu Zhao for research discussion and support. Thanks to my officemates Michael Franco, Luke Corcos and Andrew Shi for help in coding, presentation, and sharing joys and tears in Ph.D. life and I will miss our 'office party' very much. Thanks to my friends Zixin Jiang, Bo Li, Chiao-Yu Yang, Alexander Meli, Ian Gleason, Zixi Hu, Colin Wahl, Jeff Zhang, Jianwei Xiao, Anningzhe Gao, Jimmy Xia, Chris Miller and my roommate Guanghan Meng for making my non-academic life so colorful and enjoyable.

Last but not the least, thanks to funding from National Science Foundation under award number DMS-1716560 and from Applied Scientific Computing Research at Lawrence Berkeley National Lab under award number DE-AC02-05CH11231 for supporting me two semesters and one summer for my research. I also acknowledge the Savio cluster for making it possible to run our parallelized code in OpenMP and MPI.

Chapter 1

Introduction

In this chapter, first we provide an introduction to the rising bubble problem and briefly describe some of the related experimental and numerical studies that have been undertaken over the years. Then we will show the reasoning behind building our new model and how we approach this problem in Chapters 2-5. The connection between numerical accuracy in our problem and Chebyshev expansion leads to the discussion on how to evaluate orthogonal polynomial more accurately. The new algorithm on using associated orthogonal polynomials to get a more accurate evaluation of the original orthogonal polynomials is discussed in Chapter 6.

1.1 Single axisymmetric bubble rising in an infinitely long vertical tube in 3D

The theoretical and experimental study of problems related to a single rising bubble in different regimes has been extensive over the years [1] [32] [41] [33] [49] [4] [43]. Bubbles and drops in free rise or fall in infinite media under the influence of gravity are generally grouped under four categories: spherical, ellipsoidal, spherical-cap or ellipsoidal-cap, and slug flow [7] [47] [43]. The slug flow regime happens when the bubble or drop is sufficiently large and it fills most of the container cross-section. Past experiments have prepared a generalized graphical correlation in terms of the Eötvös number, Morton number, and Reynolds number. We are particularly interested in the regime characterized by large Reynolds number $Re = \rho r_e U/\nu$ with r_e the equivalent radius of the bubble, U the terminal rising velocity, ν the fluid viscosity and ρ the fluid density. It has been shown experimentally people have shown that at high Reynolds number small bubbles are ellipsoidal-cap like, and for a big bubble filling the tube, we have the so-called Taylor bubble [9].

For a small air bubble rising through stagnant liquids with small viscosity, past experiments show that the bubble moves in rectilinear motion and will have a terminal velocity [7]. Moore [36] first studied a single bubble rising with a fixed velocity under the influence of a buoyancy force by approximating the bubble shape to be an oblate spheroid. The aspect

ratio of the spheroid as a function of the Weber number was determined by satisfying the normal stress condition at only two points on the surface of the bubble. Without assuming the shape of the bubble to be ellipsoidal, Miksis, Vanden-Broeck, and Keller [34] [35] convert the potential problem without gravity into a nonlinear system of integro-differential equations and solved it numerically using second-order finite differences and the trapezoidal rule. But with the number of grid points being around 20 and the low order numerical method, it is hard to tell whether a convergent solution is found under this low accuracy. We would like to reformulate the problem to solve for numerical solutions with spectral accuracy.

For a long bubble rising in a cylindrical tube, it has been found experimentally that the rise velocity U is independent of both the length of the bubble and viscous effect in the large Reynolds number regime. In 2D, Vanden-Broeck [48] models the rising of the Taylor bubble using the infinite complex potential plane configuration and solves the problem numerically by series truncations. This accurate method cannot be applied to the real three-dimensional case due to the stream function not being harmonic in 3D. In 3D, Doak and Vanden-Broeck [11] build a similar inviscid infinitely long bubble model and numerically solve it using a second-order finite difference scheme. In both 2D and 3D, they find that for nonzero surface tension T, there exists a countably infinite number of solutions, and each of these solutions corresponds to a different value of Froude number F. Numerically, however, with the missing boundary condition at the lower end of the bubble due to modeling it to be infinitely long, the low order finite difference scheme, various assumption about the bubble curvature and approximating coarsely the nonphysical singularity introduced by their mathematical model at the stagnation point, the error gotten from the numerical scheme in the 3D case is large. This makes the quantitative relation between T and F less convincing.

To study the 3D problem more accurately, we model a closed axisymmetric bubble rising in an infinitely long vertical tube filled with inviscid fluid. Using potential theory to represent the velocity potential and parametrizing the surface using the Hou-Lowengrub-Shelley (HLS) framework [44, 23], we solve for the bubble shape numerically using a spectral method. We find that when there is no gravity, i.e. Froude number is infinite, the bubble shape is wave-like and there is a 1-1 correspondence between the Weber number T and the arc-length of a cross-section of the bubble on each solution branch characterized by the number of humps of the bubble shape. With finite Froude number, we find no solution under our model. This means that viscosity plays an important role in the boundary layer. To add the effect of viscosity in the thin boundary layer while characterizing the flow outside the thin layer to be potential, we use viscous potential flow to model the problem [26] and add the normal viscous stress to the balance equation on the bubble surface. We demonstrate the steady bubble shape under different Froude numbers.

The structure of the first part of the thesis (Chapters 2-5) is as follows. In Chapter 2, we formulate the inviscid Laplacian mathematical system and represent the velocity potential using single layer potentials. We discuss two ways to parameterize the bubble surface and decide to use HLS due to several advantages. Logarithmic singularities that appear in the integral representation of the velocity potential and tangential or normal velocities on the bubble surface are analyzed. In Chapter 3, proper numerical quadratures are chosen based on

the singularity analysis, and the general numerical procedure of solving for the bubble shape is discussed. Parallelizing the code is necessary due to the drastic increase in complexity as the number of grid points on the bubble surface and on the tube increases. In the end, we show quantitative relations between the Weber number and cross-section arc-length when gravity vanishes. No solution can be found by numerical continuity when gravity is non-zero, so we instead use viscous potential flow to solve for the case with gravity in Chapter 4. With normal viscous stress added to the Bernoulli equation, the numerical solution of the viscous model exists and we demonstrate the steady bubble shapes for different Froude numbers. In Chapter 5 we model the dynamic problem of a bubble rising and changing shape in an ideal fluid using a double-layer potential on the bubble surface and a single-layer potential on the infinite tube. Ways to remove the hyper-singularity in the normal velocity on the bubble surface are devised and the evolution equation under HLS parametrization is introduced. Numerical results of a bubble shape deforming in a background flow are shown at the end of the chapter.

1.2 Accurate evaluation of orthogonal polynomials near endpoints of the integration interval

Orthogonal polynomials are the cornerstone of numerical analysis. Most spectral methods and integration schemes rely on the theory of orthogonal polynomials for their derivation and analysis. For example in the rising bubble problem, we will see in Chapter 3 that the support of the charge density on the infinite tube is first changed to $[0, 1]$ using a cotangent transformation and then the charge density is approximated by Chebyshev expansions. Also, the classical Gaussian quadrature that we will use in the numerical integration over the bubble surface and the tube is derived from Legendre polynomial approximations. To solve numerical problems accurately, it is important to minimize the error related to orthogonal polynomial expansions or integrations to ensure that it will not accumulate and contribute to the final solution. Of course, one can run the numerical algorithms in higher precision floating-point arithmetic, like quadruple precision, but it will be very time consuming compared to double precision. Our goal is to find a more accurate numerical algorithm related to orthogonal polynomial evaluations hoping to achieve round-off error accuracy that can be applied in single, double, quadruple or arbitrary precision.

For most orthogonal polynomials such as Legendre, Jacobi, and Laguerre, the classic three-term recurrence is sensitive to rounding errors near the endpoints. Consequently, this always leads to inaccurate Gaussian quadrature weights and abscissas near endpoints where polynomial evaluation is involved.

Another significant source of round-off error in schemes employing numerical quadrature or polynomial interpolation on composite grids with quadrature-based interpolation nodes is the clustering of nodes near the endpoints of the interval. For example, the density of zeros of the Jacobi polynomials $P_n^{(\alpha,\beta)}(x)$ on $[-1, 1]$ as $n \to \infty$ is well-known [14, 46] to approach

$\pi^{-1}/\sqrt{1-x^2}$, which yields grid spacing such that $\Delta_1 = O(\Delta_{n/2}^2)$, where $\Delta_i = x_i - x_{i-1}$.

The goal of the second part of the thesis is to develop alternative recurrence relations for evaluating univariate orthogonal polynomials near an endpoint of the integration interval to improve accuracy when implemented in floating-point arithmetic. These improved recurrence relations also lead to more accurate methods for computing quadrature abscissas and weights. In this second part of the thesis (Chapter 6), instead of evaluating the original orthogonal polynomials $p_n(x)$ directly, we introduce associated orthogonal polynomials $\tilde{p}_n(x)$, where $p_n(t) = \tilde{p}_{2n}(t^2)$. We devise two ways of evaluating $\tilde{p}_n(x)$. The first method is to take advantage of the relations between linear terms of $p_n(x)$ and $\tilde{p}_n(x)$. The second method makes use of the relations between Jacobi matrices of the original and associated orthogonal polynomials. It turns out the new recurrence relation gotten from the second method can be derived using continued fraction, where our 'associated orthogonal polynomials' serve as the counterpart of the 'associated continued fraction' in continued fraction theory. Numerically both methods turn out to be more accurate than the original three-term evaluation. Between the new approaches, the 'Jacobi matrix method' is generally found to be more accurate, so we mostly stick to that approach in the following calculations.

We evaluate Jacobi polynomials and generalized Laguerre polynomials with various parameters near the endpoints using the classic recurrence method, the improved method, the hybrid quadruple-double method, and the analytic formula methods based on the theory presented. We then compare the errors from the different approaches. It turns out that even in the most general case where the analytic formula of $\tilde{b}_n$ is not known, the hybrid quadruple-double method can achieve round-off error accuracy in double precision, which is 3 digits more accurate than the classic recurrence method for the problem sizes considered here.

With polynomial evaluation involved in the calculation of quadrature abscissas and weights, it is not surprising that we get more accurate quadrature abscissas and weights near endpoints by working with the new associated orthogonal polynomials. After applying one-step of the Newton-Raphson method to calculate the abscissas near endpoints more accurately, round-off error accuracy is achieved in both the Jacobi and Laguerre cases, which outperforms the Golub-Welsch algorithm. Moreover, the distances from quadrature nodes near the endpoints to that endpoint are computed with high relative accuracy, which alleviates loss of precision due to the clustering of quadrature nodes near the endpoints.

For general orthogonal polynomials, a strategy is given. As an example, we test it on Maxwell polynomials and get more accurate polynomial evaluations, quadrature abscissas and weights near the endpoint, as hoped. Error analysis carried out in the end by comparing amplification factors from the old method and our new method justifies our new method being more accurate.

Chapter 2

Single axisymmetric bubble rising steadily in an infinitely long vertical tube in 3D

This chapter describes the main theory related to the steady-state problem of axisymmetric potential flow around an air bubble. We first mathematically model a single bubble rising in potential flow inside an infinitely long vertical tube, and proceed with detailed discussion on using potential theory to represent the velocity potential. Two ways to parametrize the problem are discussed and compared, showing that the Hou-Lowengrub-Shelley (HLS) framework is more appropriate in solving our problem. We then analyze the singularities that arise in computations involving complete elliptic integrals in detail, which helps select the proper numerical integration methods in Chapter 3.

2.1 Mathematical formulation

Air bubbles rising in water have been modeled and studied extensively over the years, both experimentally and theoretically [1] [32] [41] [33] [49] [4] [43]. Various approaches in the current literature have their advantages and disadvantages. Vanden-Broeck [48] model it as a 2D inviscid problem and analyze the solution selection mechanism between Froude number and Weber number using an accurate series truncation method, but the use of complex potential in 2D does not generalize, making their method not applicable in the real 3D case. Hua and Lou [24] model the 3D dynamic problem using the Navier-Stokes equation and solve it numerically using a front tracking algorithm and finite volume method, but this is not a systematic or accurate way to show under which conditions the bubble achieves steady state. Doak and Vanden-Broeck [11] model the Taylor bubble as an infinitely long bubble without the lower boundary condition which also has large errors and suffers from the problem that the numerical methods will not converge for small grid sizes. Our goal is to develop a spectrally accurate model of the inviscid problem, trying to analyze how the

surface tension contributes to a steady-state and see under which condition there will exist a solution.

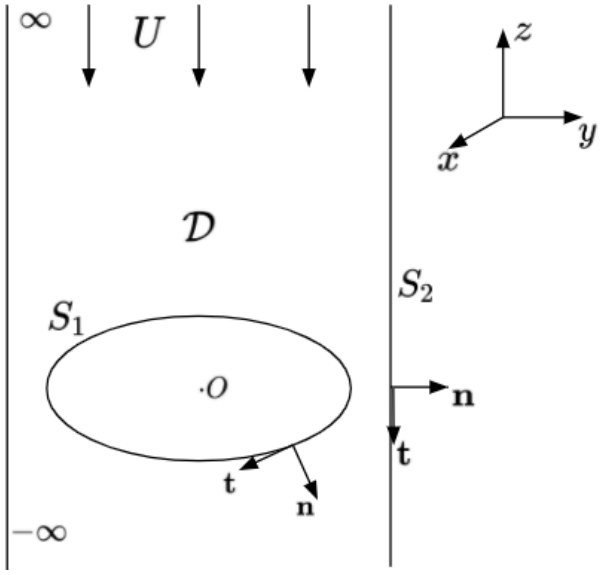

Figure 2.1: Set up of the (dimensionless) problem in (x, y, z) space

Let us consider the following idealized setup: a single bubble rising steadily in a three-dimensional infinitely long vertical tube filled with the incompressible, inviscid and irrotational flow around it. Taking the standard xyz Cartesian coordinate in $\mathbb{R}^3$ with a point O inside the bubble at the origin, we think of the bubble relatively fixed with fluid flowing down around it as in Figure 2.1. Our domain of interest $\tilde{\mathcal{D}}$ is the region bounded by the bubble surface $\tilde{S}_1$ and an infinitely long tube $\tilde{S}_2$. Here we use a tilde to denote variables before non-dimensionalization. The velocity potential $\tilde{\phi}$ satisfies

$$\Delta\tilde{\phi} = 0 \quad \text{in } \tilde{\mathcal{D}}. \tag{2.1.1}$$

Since for now we are considering the steady-state problem with the bubble shape not changing, the flow velocity on $\tilde{S}_1$ and $\tilde{S}_2$ should both be tangential, giving

$$\frac{\partial\tilde{\phi}}{\partial\mathbf{n}} = 0 \quad \text{on } \tilde{S}_1 \cup \tilde{S}_2, \tag{2.1.2}$$

with the unit normal vector $\mathbf{n}$ pointing inside $\tilde{\mathcal{D}}$ on $\tilde{S}_1$ and outside on $\tilde{S}_2$. Ideally, the background flow should be uniform at infinity, which gives

$$\frac{\partial\tilde{\phi}}{\partial\tilde{z}} \to U \quad \text{as } \tilde{z} \to \infty \text{ or } \tilde{z} \to -\infty. \tag{2.1.3}$$

Here the background flow speed U is signed, with negative (positive) sign meaning flowing downward (upward). We also assume that the density of the air inside the bubble is negligible and the pressure is a constant $\tilde{p}_0$. We denote the water-air surface tension by T, the constant density of the fluid by ρ, and the gravity by g. The Young-Laplace condition gives the pressure on the fluid side of the surface as $\tilde{p} = T\tilde{\kappa} + \tilde{p_0} = T(\frac{1}{\tilde{R}_1} + \frac{1}{\tilde{R}_2}) + \tilde{p_0}$ with $\tilde{\kappa}$ the mean curvature of $\tilde{S}_1$ and $\tilde{R}_1$, $\tilde{R}_2$ the principal radii of curvature of $\tilde{S}_1$. Notice that $\tilde{R}_1$ and $\tilde{R}_2$ are counted positive when the centers of curvature lie in $\tilde{\mathcal{D}}$. Combined with the Bernoulli equation on $\tilde{S}_1$ due to conservation of energy, we have

$$\frac{1}{2}\rho|\nabla\tilde{\phi}|^2 + \rho g\tilde{z} + \tilde{\kappa}T = \text{constant}. \tag{2.1.4}$$

Under the above inviscid model, we plan to answer the following questions on steadily rising bubbles:

1. When there is no gravity, how does the existence of the infinite tube affects the shape of steadily rising bubbles?
2. When there is no gravity, under what relations between Weber number and the arc-length of the cross-section of the bubbles does there exist a steadily rising bubble?
3. When there is gravity, does there exist a bubble that rise steadily?

2.2 Non-dimensionalization

Without background flow

We want to first study the case when $U = 0$, i.e. with a stationary bubble in a stagnant fluid. In this case, $\tilde{\phi}$ is a constant, which automatically satisfies the Laplacian equation and all the Neumann boundary condition, so the only equation we are solving is the Bernoulli equation (2.1.4). In this case, it is simplified to be

$$\rho g\tilde{z} + \tilde{\kappa}T = \text{constant}. \tag{2.2.1}$$

We claim that the only solution to (2.2.1) happens when $g = 0$ and $\tilde{\kappa} = c$ with c a constant, i.e. a round bubble remains still under no gravity. First it is easy to check that the above equation holds when $g = 0$ and $\tilde{\kappa} = c$, so this is a solution. Notice that when there is a boundary wall, i.e. the infinite tube $\tilde{S}_2$ is present, the round bubble can only have a radius smaller than tube radius H. Without the tube, theoretically, it can be of any size. In fact when $g = 0$, $\tilde{S}_1$ needs to be a so-called constant-mean-curvature surface. Delaunay proved in 1841 [10] that the only surfaces of revolution with constant mean curvature are the surfaces obtained by rotating the roulettes of the conics. These are the plane, cylinder, sphere, the catenoid, the unduloid, and the nodoid. Since our surface needs to be closed and compact with front and back stagnation point having horizontal tangent planes, it must be a sphere.

When $g \neq 0$, the hydrostatic pressure cannot be balanced out by the effects of surface tension on the bubble interface as the solution of the balanced equation between pressure forces and surface tension forces can only be a meniscus touching the wall [15].

With background flow

To non-dimensionalize the above problem when $U \neq 0$, we normalize the far-field background flow speed U and treat the tube radius H as the unit reference length. Under this remapping, we define $\phi(x, y, z) = \frac{\tilde{\phi}(\tilde{x},\tilde{y},\tilde{z})}{UH}$, $\tilde{x} = Hx$, $\tilde{y} = Hy$, $\tilde{z} = Hz$, $\tilde{R}_1 = HR_1$, $\tilde{R}_2 = HR_2$ and $T = \tilde{T}/H$. Substituting into (2.1.1 – 2.1.4), we build a complete system of equations for the velocity potential ϕ as the following

$$\begin{aligned}
&\Delta\phi = 0 \quad \text{in } \mathcal{D},\\
&\frac{\partial\phi}{\partial\mathbf{n}} = 0 \quad \text{on the free bubble surface } S_1,\\
&\frac{\partial\phi}{\partial\mathbf{n}} = 0 \quad \text{on the cylindrical wall } S_2 = \{x^2 + y^2 = 1\},\\
&\frac{\partial\phi}{\partial z} = -1 \quad \text{at } z = \pm\infty,\\
&|\nabla\phi|^2 + \frac{2}{F^2}z + \frac{2}{W}\kappa = C \quad \text{on } S_1,
\end{aligned} \tag{2.2.2}$$

where $F = \frac{U}{\sqrt{gH}}$ is the Froude number, $W = \frac{U^2H\rho}{T}$ is the Weber number and C is a constant. Note that the constants F and W uniquely define the problem.

A variant of the problem is to remove the infinitely long tube so that the boundary of the flow domain is only the bubble surface. The equations on bubble surface and at infinity remain the same. Due to the removal of the outer wall, we need to find an alternative reference length. One convention is to use the capillary length $L_c = \sqrt{\frac{T}{\rho g}}$ as the reference length, so that the Bernoulli equation is non-dimensionalised to

$$|\nabla\phi|^2 + \frac{2}{W}z + \frac{2}{W}\kappa = C \quad \text{on } S_1,$$

with $W = U^2\sqrt{\frac{Tg}{\rho}}$. Another way is to use the equivalent radius of bubble r_e as the reference length. But for convenience, we choose the arc-length element σ (which is defined in the HLS parameterization in Section 2.6 below) as the reference length. The dimensionless Bernoulli equation will be the same as before except H is replaced by σ in the expression of F and W.

2.3 Potential theory

Potential theory is heavily used when representing the velocity potential in both the steady and unsteady problems, so it is worthwhile to describe the key theorems here for later reference [12, 28, 29, 16, 8, 21].

Let $N(p,q)$ denote the fundamental solution of Laplace's equation in $\mathbb{R}^n$, $n \geq 2$. Particularly, when $n = 3$ as in our case, $N(p,q) = \frac{1}{4\pi|p-q|}$. Let $\mu(q)$ be a continuous function on Γ, where Γ is a closed Lyapunov surface in $\mathbb{R}^n$, separating $\mathbb{R}^n$ into an interior domain $\mathcal{D}^+$ and an exterior domain $\mathcal{D}^-$. The single layer (S), double layer (D), adjoint double layer (D'), and hyper-singular (H) operators with charge density μ are formally defined as

$$S[\mu](p) := \int_\Gamma N(p,q)\mu(q)\, dA_q, \tag{2.3.1a}$$

$$D'[\mu](p) := \int_\Gamma \frac{\partial N(p,q)}{\partial \mathbf{n}_p}\mu(q)\, dA_q, \tag{2.3.1b}$$

$$D[\mu](p) := \int_\Gamma \frac{\partial N(p,q)}{\partial \mathbf{n}_q}\mu(q)\, dA_q, \tag{2.3.1c}$$

$$H[\mu](p) := p.v. \int_\Gamma \frac{\partial^2 N(p,q)}{\partial \mathbf{n}_p \partial \mathbf{n}_q}\mu(q)\, dA_q = \lim_{\epsilon\to 0}\int_{\Gamma - B_\epsilon(p)} \frac{\partial^2 N(p,q)}{\partial \mathbf{n}_p \partial \mathbf{n}_q}\mu(q)\, dA_q, \tag{2.3.1d}$$

where dA_q is the area element on Γ and $B_\epsilon(p)$ is the intersection of Γ with a ball of radius ϵ centered at p. Notice that formally, D' is the normal derivative of S, and H is the normal derivative of D. When $p \notin \Gamma$, the four integrals above are not singular. When $p \in \Gamma$, however, S, D' and D contains $1/|p-q|$ type singularity in the integrand, which is integrable on a 2-d surface in the normal sense. For D, in its integrand we have $\frac{\partial N(p,q)}{\partial \mathbf{n}_q} = \frac{(p-q)\cdot \mathbf{n}_q}{|p-q|^3}$ and $(p-q)\cdot\mathbf{n}_q = \mathcal{O}(|p-q|^2)$ due to $\mathbf{n}_q$ and $(p-q)$ being almost orthogonal as q approaches p along Γ. Similar argument also applies to D'. But H contains $1/|p-q|^3$ type hyper-singularity in the integrand, so it must be understood in the principal value sense as in (2.3.1d) (The principal value symbol can be dropped when $p \notin \Gamma$). Different strategies of dealing with these singularities numerically will be discussed later this chapter and in Chapter 5. The regularity of these four operators regarding Γ and μ has been studied thoroughly over the years. Since we are concentrating on getting spectral accuracy of the numerical solutions, from now on we assume for simplicity that Γ is a smooth surface and μ is C^∞.

The normal derivative of a single-layer potential (2.3.1a) has a discontinuity when passing across the surface S as follows

$$\left(\frac{\partial S[\mu](p)}{\partial \mathbf{n}_p}\right)^+ =: \lim_{p'\to p, p'\in\mathcal{D}^+} \frac{\partial S[\mu](p')}{\partial \mathbf{n}_p} = \frac{\mu(p)}{2} + D'[\mu](p), \tag{2.3.2a}$$

$$\left(\frac{\partial S[\mu](p)}{\partial \mathbf{n}_p}\right)^- =: \lim_{p'\to p, p'\in\mathcal{D}^-} \frac{\partial S[\mu](p')}{\partial \mathbf{n}_p} = -\frac{\mu(p)}{2} + D'[\mu](p), \tag{2.3.2b}$$

where $\left(\frac{\partial S[\mu](p)}{\partial \mathbf{n}_p}\right)^\pm$ are the limiting values of the normal derivatives from $\mathcal{D}^\pm$ as defined above. $D'[\mu](p)$ is sometimes also called the direct value of $\frac{\partial S[\mu](p)}{\partial \mathbf{n}_p}$. The tangential derivative of single layer potential is continuous across S, and is denoted by $\frac{\partial S[\mu](p)}{\partial \mathbf{t}_p}$. In three dimensions, both integrals (2.3.1a) and (2.3.1b) feature weakly singular kernels that will be discussed later in Section 2.6. The tangential derivative, however, has an order one pole in our case,

which will also be discussed in detail in Section 2.6. But the singularity can be removed as explained in Chapter 3.

A double layer potential, when passing across the surface Γ, has a discontinuity

$$D^+[\mu](p) := \lim_{p'\to p, p'\in\mathcal{D}^+} D[\mu](p') = -\frac{\mu}{2} + D[\mu](p), \tag{2.3.3a}$$

$$D^-[\mu](p) := \lim_{p'\to p, p'\in\mathcal{D}^-} D[\mu](p') = \frac{\mu}{2} + D[\mu](p), \tag{2.3.3b}$$

where $D^\pm[\mu](p)$ are the limit values of the double layer potential $\mathcal{D}^\pm$ as defined above. $D[\mu](p)$ in (2.3.1c) denotes the so-called direct value of the double-layer potential calculated over the surface Γ. The kernel in $D[\mu](p)$ features a weak singularity, thus making it integrable. The tangential derivative applying to both sides of (2.3.3) also has a jump, and the formal tangential derivative $\frac{\partial D[\mu](p)}{\partial \mathbf{t}_p}$ has a $1/|p-q|^2$ type singularity, which is integrated similarly in principal value sense as in steady state case. But the normal derivative retains its value when passing across S

$$\left(\frac{\partial D[\mu](p)}{\partial \mathbf{n}_p}\right)^+ := \lim_{p'\to p, p'\in\mathcal{D}^+} \frac{\partial D[\mu](p')}{\partial \mathbf{n}_p} = H[\mu](p) = \lim_{p'\to p, p'\in\mathcal{D}^-} \frac{\partial D[\mu](p')}{\partial \mathbf{n}_p} =: \left(\frac{\partial D[\mu](p)}{\partial \mathbf{n}_p}\right)^-. \tag{2.3.4}$$

Although formally similar, (2.3.1d) is divergent due to the hyper-singular kernel and the Cauchy principal value version of it coincides with the above limiting value. To get spectral accuracy, however, we apply a singularity removal technique. The procedure will be fully discussed in detail in Chapter 4.

It is easy to show by Green's identity that any harmonic function ϕ can be represented by the sum of single and double layer potentials with densities $\frac{\partial \phi(p)}{\partial \mathbf{n}_p}$ and $-\phi(p)$ respectively; however, we are more interested in expressing it using only a single layer or double layer potential. This can be achieved using the Fredholm alternative of compact operators in the following four basic scenarios. We refer to the setup and theorems from [12] in the following. Let $\Omega = \Omega^+$ be an open bounded domain in $\mathbb{R}^n$ with $\mathcal{C}^2$ boundary Γ. Let $\Omega^- = \mathbb{R}^n - (\Omega^+ \cup \Gamma)$. Ω^+ and Ω^- will both be allowed to be disconnected. However, since Γ is differentiable there can only be finitely many components. We denote the connected components of Ω^+ by Ω_1^+, $\cdots$, Ω_m^+, and those of Ω^- by Ω_0^-, Ω_1^- $\cdots$ $\Omega_{m'}^-$, where Ω_0^- is the unbounded component.

Interior Dirichlet: Find a function $\phi(x) \in \mathcal{C}(\Omega^+ \cup \Gamma)$ that is harmonic in Ω^+ and satisfies the boundary condition $\phi(x) = u(x)$ for $x \in \Gamma$, with $u(x) \in \mathcal{C}(\Gamma)$. The solution to this problem always exists, and is unique. Due to the m' dimensional kernel of the left hand side operator in (2.3.3a), a correction of the equation should be made before solving for $\mu(x)$. See the proof of Theorem 3.40 from [12] for details.

Exterior Dirichlet: Find a function $\phi(x) \in \mathcal{C}(\Omega^- \cup \Gamma)$ that is harmonic in Ω^- and regular at infinity i.e.

$$\lim_{|x|\to\infty} |x|^{n-2}\phi(x) = \text{const},$$

and satisfies the boundary condition $\phi(x) = u(x)$ for $x \in \Gamma$, with $u(x) \in \mathcal{C}(\Gamma)$. Here $n = 2$ or 3 is the dimension of physical space. The solution to this problem always exists and

is unique. Due to the m dimensional kernel of the left hand side operator in (2.3.3b), a correction of the equation should be made before solving for $\mu(x)$, similar to the interior Dirichlet case for $n \geq 3$. When $n = 2$, one extra step should be applied.

Interior Neumann: Find a function $\phi(x) \in \mathcal{C}^1(\Omega^+ \cup \Gamma)$ that is harmonic in Ω^+ and satisfies the boundary condition $\frac{\partial \phi(x)}{\partial \mathbf{n}_x} = u(x)$ for $x \in \Gamma$, with $u(x) \in \mathcal{C}(\Gamma)$. A solution to this problem exists if and only if the following condition holds

$$\int_{\partial \Omega_j^+} u(x)\, dA_x = 0 \quad \text{for } j = 1, \cdots, m. \tag{2.3.5}$$

The solution is unique modulo functions which are constant on each Ω_j^+. It can be represented as $S[\mu](x)$ where μ is obtained from (2.3.2a). Its corresponding homogeneous equation has a solution space of dimension m and (2.3.2a) is solvable under the condition (2.3.5).

Exterior Neumann: Find a function $\phi(x) \in \mathcal{C}^1(\Omega^- \cup \Gamma)$ that is harmonic in Ω^- and regular at infinity and satisfies the boundary condition $\frac{\partial \phi(x)}{\partial \mathbf{n}_x} = u(x)$ for $x \in \Gamma$, with $u(x) \in \mathcal{C}(\Gamma)$. A solution exists if and only if

$$\int_{\partial \Omega_j^-} u(x)\, dA_x = 0 \quad \text{for } j = 1, \cdots, m', \tag{2.3.6}$$

and also for $j = 0$ when $n = 2$. The solution is unique modulo functions which are constant on $\Omega_1^-, \cdots, \Omega_{m'}^-$ and also on Ω_0^- when $n = 2$.

In our case, the cylindrical wall is infinite, so the above theorems do not strictly apply, but the arguments can be modified to handle this case, as explained below.

2.4 Representing the steady velocity potential using a single layer potential

Now we are ready to use potential theory to solve the system (2.2.2). Using the notation from the last section, we can divide $\mathbb{R}^3$ into three parts, the connected open bounded set inside S_1, which we denote by Ω_1^-; the connected open set inside S_2 and outside S_1, which is exactly our flow region $\mathcal{D} = \Omega_1$; and the unbounded set outside S_2, denoted by Ω_0^-. So in our case, $m = m' = 1$. When requiring vanishing normal velocity on S_1 and S_2 approaching from inside $\mathcal{D}$, it is an interior Neumann problem. A caveat here is that in this set-up, the inside domain for S_2, i.e. $\Omega_1^- \cup S_1 \cup \mathcal{D}$, is not bounded. But potential theory is based on the divergence theorem, which can be extended to the infinite region with functions regular at infinity [28]. So with smooth charge densities, (2.3.2) and (2.3.3) still hold in our case. We can imagine smoothing out the problem by adding an upper and lower cap far away to the cylindrical tube. This way the modified tube with caps form closed boundary and all the previous theory should still apply. Since charges far away from the bubble contribute very little to the potential near the bubble due to the decaying property of our integrand, solution

to the modified problem should be very close to the original problem and we should expect the interior Neumann problem applicable to our infinitely-long vertical tube case. Although we cannot prove the compactness of D' on the space of continuous axisymmetric functions defined on S_2 with a finite limit at infinity, there can still exist legitimate solutions without the integral operator being compact. We will show in Chapter 3 that the layer potential method works well numerically.

Based on the discussion above, we use single layer potentials to represent the solution. In this normalized setting, the velocity potential ϕ consists of three parts. The first part is the velocity potential ϕ_1 induced by the 'charges' on the bubble surface S_1; the second part ϕ_2 is induced by the 'charges' on S_2; and the third part accounts for the uniform downward flow with unit speed. Mathematically, we can write it as

$$\phi = \phi_1 + \phi_2 - z, \tag{2.4.1}$$

where

$$\begin{aligned} \phi_1(p) &= \int_{S_1} \frac{\mu_1(q)}{4\pi|p-q|}\, dA_q, \\ \phi_2(p) &= \int_{S_2} \frac{\mu_2(q)}{4\pi|p-q|}\, dA_q, \end{aligned} \tag{2.4.2}$$

with μ_i unknown charge densities on S_i to be found. With exterior Neumann boundary condition on S_1 and the interior Neumann boundary condition on S_2, using (2.3.2b) and (2.3.2a) respectively, we get

$$-2\pi\mu_1(p) + \int_{S_1} \frac{(q-p)\cdot\mathbf{n}(p)}{|p-q|^3}\mu_1(q)\, dA_q + \int_{S_2} \frac{(q-p)\cdot\mathbf{n}(p)}{|p-q|^3}\mu_2(q)\, dA_q = 4\pi n_3(p), \quad p \in S_1, \tag{2.4.3a}$$

$$2\pi\mu_2(p) + \int_{S_1} \frac{(q-p)\cdot\mathbf{n}(p)}{|p-q|^3}\mu_1(q)\, dA_q + \int_{S_2} \frac{(q-p)\cdot\mathbf{n}(p)}{|p-q|^3}\mu_2(q)\, dA_q = 0, \quad p \in S_2, \tag{2.4.3b}$$

with $\mathbf{n}(p) = (n_1(p), n_2(p), n_3(p))$ the outward normal vector for any $p \in S_1 \cup S_2$.

2.5 Solvability of the integral equation

Since one main step in the calculation is solving for charge densities μ_1 and μ_2 from (2.4.3), we want to prove that the equation is solvable with the given right hand side data. Since it is an interior Neumann problem with $m = m' = 1$ as discussed at the beginning of Section 2.4, it has a one dimensional kernel in $\mathcal{C}(S_1 \cup S_2)$ and the problem is solvable if and only if the right hand side function in (2.4.3) has vanishing mean, i.e. $\int_{S_1} 4\pi n_3(p)\, dA_p = 0$, which is easily seen to hold. Now we prove that the one-dimensional kernel is the constant function on S_2. Fixing $\mu_1(q) = 0$ for any $q \in S_1$ and $\mu_2(q) = 1$ for any $q \in S_2$, evaluating (2.4.3b) at

$p = (1, 0, z)$ for any z gives zero:

$$\begin{aligned}
&2\pi + \int_{-\infty}^{\infty}\int_{0}^{2\pi} \frac{-1+\cos\varphi}{\left((z-y)^2+2-2\cos\varphi\right)^{3/2}}\, d\varphi dy \\
&= 2\pi + \int_{-\infty}^{\infty}\int_{0}^{2\pi} \frac{-1+\cos\varphi}{\left(y^2+2-2\cos\varphi\right)^{3/2}}\, d\varphi dy \\
&= 2\pi - 4\int_{-\infty}^{\infty}\int_{0}^{\pi} \frac{\sin^2\varphi}{\left(y^2+4\sin^2\varphi\right)^{3/2}}\, d\varphi dy \\
&= 2\pi - 4\int_{0}^{\pi}\int_{-\infty}^{\infty} \frac{\sin^2\varphi}{\left(y^2+4\sin^2\varphi\right)^{3/2}}\, dy d\varphi \\
&= 2\pi - \int_{0}^{\pi} \frac{y}{\sqrt{y^2+4\sin^2\varphi}}\Big|_{y=-\infty}^{\infty} d\varphi = 0.
\end{aligned}$$

Here the integration order can be swapped in the second line due to the non-negativity of the integrand and Fubini's theorem. Similarly it is easy to show that $\nabla\phi_2(p)\cdot(0,1,0) = (0,0,0)$ for any $p \in S_1$, so evaluating (2.4.3a) gives $\int_{S_2} \frac{(q-p)\cdot\mathbf{n}(p)}{|p-q|^3}\, dA_q = \frac{\partial}{\partial \mathbf{n}_p}(\int_{S_2} \frac{1}{|p-q|}\, dA_q) = 0$ for any $p \in S_1$. We proved that $[\mu_1(q), \mu_2(q)]$ in (2.4.3) can be uniquely solved up to a constant function on S_2.

2.6 Two parametrizations: radial and HLS

Due to the problem being axisymmetric about the z-axis, instead of studying the whole surface S_1, from now on, unless stated otherwise, we concentrate on the profile curve of a cross-section, i.e. $S_1 \cap \{y = 0\}$. A natural parametrization is to use the polar angle τ to describe the profile curve as the radial function $R(\tau)$, as shown in the left figure of 2.2. Points on the profile curve can be written as $(x, y, z) = (R(\tau)\sin\tau, 0, R(\tau)\cos\tau,)$ and the mean curvature in the Bernoulli equation is $\kappa = \frac{RR''-R^2-2R'^2}{(R^2+R'^2)^{3/2}} + \frac{R'\cot\tau/R-1}{(R^2+R'^2)^{1/2}}$. $R(\tau)$ is 2π periodic and also even around $k\pi$ for any $k \in \mathbb{Z}$, thus is expanded as a Fourier cosine series. Radial parametrization works well for profile curves that are close to a circle, but the following drawbacks are difficult to deal with:

1. For elongated or very oblate bubbles, a uniform grid on τ cannot resolve the profile curve evenly, making it hard for spectral modes to decay when its arclength element $\sqrt{R^2(\tau) + R'^2(\tau)}$ changes rapidly.

2. Since second derivatives are involved in calculating κ, high order differentiation brings in more numerical error.

3. It is impossible to describe profile curves with 'overturns'. If more than one point corresponds to a certain radial angle τ, $R(\tau)$ is not a well-defined function. See the right panel in Figure 2.2.

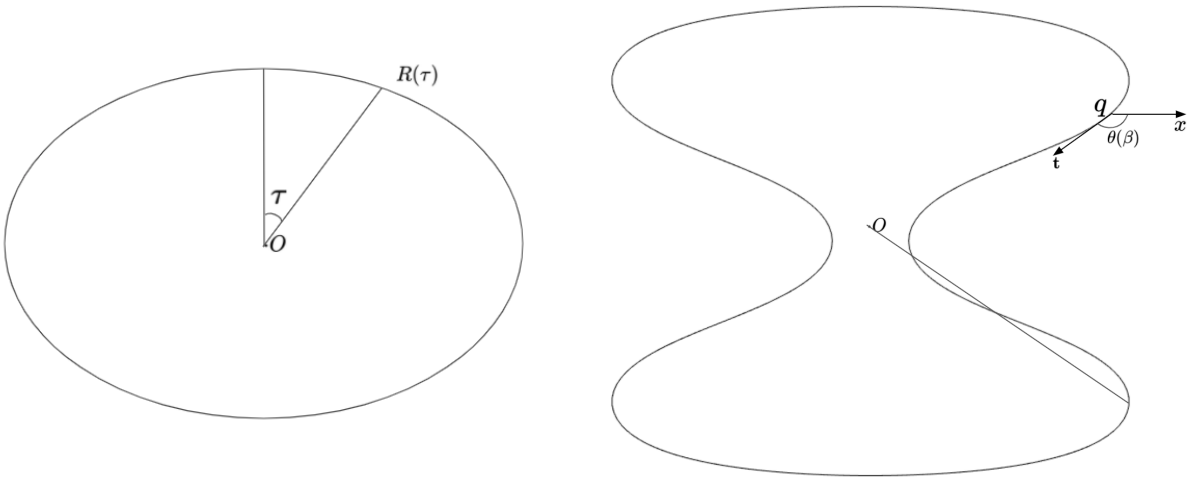

Figure 2.2: Two ways to parametrize the bubble surface, the radial angle (left) and the HLS framework (right) in a case where radial parametrization breaks down.

Alternatively, we can follow the approach of Hou, Lowengrub, and Shelley (HLS) [44, 23]. We will show below that the above three issues can be solved naturally by HLS. The profile curve can be parametrized as $\{(\xi(\alpha), 0, \eta(\alpha)), \alpha \in [0, 2\pi]\}$. For any point $q \in S_1$ we can write it as $q = \big(\xi(\alpha)\cos\varphi, \xi(\alpha)\sin\varphi, \eta(\alpha)\big)$ with $\alpha \in [0, 2\pi]$ and $\varphi \in [0, 2\pi]$. Given $\xi(\alpha)$ and $\eta(\alpha)$, we can find another pair of variables: the arc length element $s'(\alpha) = \sqrt{\xi'^2 + \eta'^2}$, and the tangential angle $\theta(\alpha) = \arctan\big(\frac{\eta'(\alpha)}{\xi'(\alpha)}\big)$. On the other hand, we can treat s' and θ as the pair of free variable describing the bubble, and represent $\xi(\alpha)$ and $\eta(\alpha)$ easily as

$$\xi(\alpha) = \xi(0) + \int_0^\alpha \cos(\theta(\beta))s'(\beta)\,d\beta, \quad \eta(\alpha) = \eta(0) + \int_0^\alpha \sin(\theta(\beta))s'(\beta)\,d\beta. \tag{2.6.1}$$

This shows that problem 3 listed above is not an issue anymore in the HLS framework. Notice that the problem we are working on is a steady-state problem, so we do not have time variables involved in any calculation and the differentiation is with respect to the parameter β by default. Due to the time-invariant nature of the problem, $s'(\beta)$ is fixed as a constant σ to make sure that the uniform grid points of β are spreading out uniformly with respect to arc length. This solves problem 1 listed above.

Now let us fully expand (2.4.3) according to the above parametrization. Since S_1 and S_2 are both axisymmetric, charge densities μ_1 and μ_2 in (2.4.2) do not depend on φ and can also be parametrized as $\mu_1(\alpha)$ with $\alpha \in [0, \pi]$, $\mu_2(y)$ with $y \in (-\infty, \infty)$. Also, to enforce (2.4.3) we only need to evaluate it at $\big(\xi(\alpha), 0, \eta(\alpha)\big) \in S_1$ and $(1, 0, z) \in S_2$. To make the

notation cleaner, we use $G[a,b,c,d]$ to denote the following integral

$$\begin{aligned} G[a,b,c,d] :&= \int_0^{2\pi} \frac{a - b\cos\varphi}{(c - d\cos\varphi)^{3/2}}\, d\varphi \\ &= \frac{4b}{d\sqrt{c-d}} K\left(-\frac{2d}{c-d}\right) - 4\frac{(bc-ad)}{(c+d)d\sqrt{c-d}} E\left(-\frac{2d}{c-d}\right), \end{aligned} \tag{2.6.2}$$

where K and E are the complete elliptic integrals of the first and second kind. When $d = 0$, the above integral can be easily computed to have analytic expression $\frac{2\pi a}{c^{3/2}}$.

In (2.4.3a), for any fixed $p = \big(\xi(\alpha), 0, \eta(\alpha)\big) \in S_1$ and any $q = \big(\xi(\beta)\cos\varphi, \xi(\beta)\sin\varphi, \eta(\beta)\big) \in S_1$, we have $\mathbf{n}(p) = (-\sin\theta(\alpha), 0, \cos\theta(\alpha))$, $(q-p)\cdot\mathbf{n}(p) = -(\eta(\alpha)-\eta(\beta))\cos\theta(\alpha) + \xi(\alpha)\sin\theta(\alpha) - \xi(\beta)\sin\theta(\alpha)\cos\varphi$ and $|p-q|^2 = \xi^2(\alpha)+\xi^2(\beta)+(\eta(\alpha)-\eta(\beta))^2 - 2\xi(\alpha)\xi(\beta)\cos\varphi$. With notation (2.6.2), we can rewrite the following integral as

$$\int_{S_1} \frac{(q-p)\cdot\mathbf{n}(p)}{|p-q|^3}\mu_1(q)\, dA_q = \int_0^{\pi} \mu_1(\beta)\xi(\beta)s'(\beta)G[a_1,b_1,c_1,d_1]\, d\beta,$$

with

$$\begin{aligned} a_1 &= -(\eta(\alpha)-\eta(\beta))\cos\theta(\alpha) + \xi(\alpha)\sin\theta(\alpha), \\ b_1 &= \xi(\beta)\sin\theta(\alpha), \\ c_1 &= \xi^2(\alpha) + \xi^2(\beta) + (\eta(\alpha)-\eta(\beta))^2, \\ d_1 &= 2\xi(\alpha)\xi(\beta). \end{aligned}$$

For any $q = (\cos\varphi, \sin\varphi, y) \in S_2$, we have $(q-p)\cdot\mathbf{n}(p) = -(\eta(\alpha)-y)\cos\theta(\alpha) + \xi(\alpha)\sin\theta(\alpha) - \sin\theta(\alpha)\cos\varphi$ and $|p-q|^2 = (y-\eta(\alpha))^2 + 1 + \xi^2(\alpha) - 2\xi(\alpha)\cos\varphi$. Using this, we can rewrite the following integral as

$$\int_{S_2} \frac{(q-p)\cdot\mathbf{n}(p)}{|p-q|^3}\mu_2(q)\, dA_q = \int_{-\infty}^{\infty} \mu_2(y)G[e_1,f_1,g_1,h_1]\, dy,$$

with

$$\begin{aligned} e_1 &= -(\eta(\alpha)-y)\cos\theta(\alpha) + \xi(\alpha)\sin\theta(\alpha), \\ f_1 &= \sin\theta(\alpha), \\ g_1 &= (y-\eta(\alpha))^2 + 1 + \xi^2(\alpha), \\ h_1 &= 2\xi(\alpha). \end{aligned}$$

Similarly, in the (2.4.3b), for any fixed $p = (1,0,z)$, we have $\mathbf{n}(p) = (1,0,0)$. For any $q = \big(\xi(\beta)\cos\varphi, \xi(\beta)\sin\varphi, \eta(\beta)\big)$, we have $(q-p)\cdot\mathbf{n}(p) = \xi(\beta)\cos\varphi - 1$ and $|p-q|^2 = \xi^2(\beta) + 1 + (\eta(\beta)-x)^2 - 2\xi(\beta)\cos\varphi$. With notation in (2.6.2), we have

$$\int_{S_1} \frac{(q-p)\cdot\mathbf{n}(p)}{|p-q|^3}\mu_1(q)\, dA_q = \int_0^{\pi} \mu_1(\beta)\xi(\beta)s'(\beta)G[a_2,b_2,c_2,d_2]\, d\beta,$$

with

$$a_2 = -1, \quad b_2 = -\xi(\beta), \quad c_2 = \xi^2(\beta) + 1 + (\eta(\beta)-z)^2, \quad d_2 = 2\xi(\beta).$$

For any $q = (\cos\varphi, \sin\varphi, y) \in S_2$, we have $(q-p)\cdot\mathbf{n}(p) = \cos\varphi - 1$ and $|p-q|^2 = (y-z)^2 + 2 - 2\cos\varphi$. Using this, we have

$$\int_{S_2} \frac{(q-p)\cdot\mathbf{n}(p)}{|p-q|^3}\mu_2(q)\,dA_q = \int_{-\infty}^{\infty} \mu_2(y)G[e_2, f_2, g_2, h_2]\,dy,$$

with

$$e_2 = -1, \quad f_2 = -1, \quad g_2 = (y-z)^2 + 2, \quad h_2 = 2.$$

Combining the above, the Neumann condition (2.4.3) can be written as

$$\begin{aligned} &2\pi\mu_1(\alpha) + \underbrace{\int_0^{\pi} \mu_1(\beta)\xi(\beta)s'(\beta)G[a_1, b_1, c_1, d_1]\,d\beta}_{\Pi_1} + \int_{-\infty}^{\infty} \mu_2(y)G[e_1, f_1, g_1, h_1]\,dy \\ &\quad = -4\pi\cos\theta(\alpha), \quad \alpha \in [0,\pi], \\ &2\pi\mu_2(z) + \int_0^{\pi} \mu_1(\beta)\xi(\beta)s'(\beta)G[a_2, b_2, c_2, d_2]\,d\beta + \underbrace{\int_{-\infty}^{\infty} \mu_2(y)G[e_2, f_2, g_2, h_2]\,dy}_{\Pi_2} \\ &\quad = 0, \quad z \in (-\infty, \infty), \end{aligned} \tag{2.6.3}$$

with a_i, b_i, c_i, d_i, e_i, f_i, g_i, h_i with $i = 1, 2$ as listed out previously. With the given initial bubble shape, μ_1 and μ_2 can be solved using (2.6.3) and the velocity potential ϕ is uniquely determined by (2.7.3) (2.4.2). Furthermore, at any $p = \big(\xi(\alpha), 0, \eta(\alpha)\big) \in S_1$, the velocity potential can be evaluated as

$$\phi(p) = \frac{1}{4\pi}\int_0^{\pi} \mu_1(\beta)\xi(\beta)s_\beta \frac{4K\big(\frac{-2c_1}{c_1-d_1}\big)}{\sqrt{c_1-d_1}}\,d\beta + \frac{1}{4\pi}\int_{-\infty}^{\infty} \mu_2(y)\frac{4K\big(\frac{-2h_1}{g_1-h_1}\big)}{\sqrt{g_1-h_1}}\,dy - \eta(\alpha). \tag{2.6.4}$$

Now we are only left with one more constraint: the Bernoulli equation. Due to the axisymmetric nature of the bubble surface, it suffices to enforce the Bernoulli equation on points $p = (\xi(\alpha), 0, \eta(\alpha))$, $\alpha \in [0, \pi]$. Due to the vanishing normal velocity, $|\nabla\phi|^2 = |\frac{\partial\phi}{\partial s}|^2$ on S_1. One way to calculate $|\frac{\partial\phi}{\partial s}|$ is to take the derivative of (2.6.4) with respect to arc-length numerically using FFT. Here we resort to a more accurate method by calculating the derivatives analytically. When calculating tangential velocity $\frac{\partial\phi}{\partial s} = \frac{1}{s'(\alpha)}\frac{\partial\phi}{\partial\alpha}$, ϕ_2 and $-z$ are both smooth and can be differentiated directly as the following:

$$\frac{\partial\phi_2}{\partial s} = \frac{1}{s'(\alpha)}\frac{\partial\phi_2}{\partial\alpha} = \int_{S_2} \frac{1}{s'(\alpha)}\frac{\partial}{\partial\alpha}\frac{\mu_2(q)}{4\pi|p-q|}\,dA_q = \frac{-1}{4\pi}\int_{-\infty}^{\infty} \mu_2(y)G[e_3, f_3, g_1, h_1]\,d\beta, \tag{2.6.5}$$

with g_1 and h_1 still as before and

$$e_3 = \frac{1}{2s'(\alpha)}\frac{\partial g_1}{\partial\alpha} = (\eta(\alpha) - y)\frac{\eta'(\alpha)}{s'(\alpha)} + \xi(\alpha)\frac{\xi'(\alpha)}{s'(\alpha)} = (\eta(\alpha) - y)\sin\theta(\alpha) + \xi(\alpha)\cos\theta(\alpha),$$

$$f_3 = \frac{1}{2s'(\alpha)}\frac{\partial h_1}{\partial \alpha} = \frac{\xi'(\alpha)}{s'(\alpha)} = \cos\theta(\alpha).$$

Similarly, we have

$$\frac{\partial z}{\partial s} = \frac{1}{s'(\alpha)}\frac{\partial z}{\partial \alpha} = \frac{\eta'(\alpha)}{s'(\alpha)} = \sin\theta(\alpha).$$

$\frac{\partial \phi_1}{\partial s}$ is different due to the discontinuity in $\nabla\phi_1$ across S_1 , which will be proved in detail in the next section. We will prove that for $\alpha \in (0,\pi)$

$$\frac{1}{s'(\alpha)}\frac{\partial \phi_1}{\partial \alpha} = p.v.\int_{S_1}\frac{1}{s'(\alpha)}\frac{\partial}{\partial \alpha}\Big(\frac{\mu_1(q)}{4\pi|p-q|}\Big)\,dA_q = \underbrace{\frac{-1}{4\pi}p.v.\int_0^{\pi}\mu_1(\beta)\xi(\beta)s'(\beta)G[a_3,b_3,c_1,d_1]\,d\beta}_{\Pi_3}, \tag{2.6.6}$$

with c_1 and d_1 still as before and

$$a_3 = \frac{1}{2s'(\alpha)}\frac{\partial c_1}{\partial \alpha} = \xi(\alpha)\frac{\xi'(\alpha)}{s'(\alpha)} + (\eta(\alpha)-\eta(\beta))\frac{\eta'(\alpha)}{s'(\alpha)} = \xi(\alpha)\cos\theta(\alpha) + (\eta(\alpha)-\eta(\beta))\sin\theta(\alpha),$$

$$b_3 = \frac{1}{2s'(\alpha)}\frac{\partial d_1}{\partial \alpha} = \frac{\xi'(\alpha)}{s'(\alpha)}\xi(\beta) = \xi(\beta)\cos\theta(\alpha).$$

Notice that without the principal value in Π_3, by Taylor series expansion around $\beta = \alpha$ we get $b_3c_1 - a_3d_1 \sim \mathcal{O}(\alpha-\beta)$, which results in a $1/(\beta-\alpha)$ type singularity in the integral. This indicates the importance of the principal value in Π_3, whose derivation will be shown in detail in the next section.

As for mean curvature, the formula is $\kappa = \frac{1}{R_1} + \frac{1}{R_2}$, where

$$R_1 = \frac{\partial s}{\partial \theta} = \frac{\partial s}{\partial \alpha}\frac{\partial \alpha}{\partial \theta} = \frac{s'(\alpha)}{\theta'(\alpha)}, \quad R_2 = \frac{\xi(\alpha)}{\sin\theta}. \tag{2.6.7}$$

Notice that $R_2(0) = R_1(0)$ and $R_2(\pi) = R_1(\pi)$ in the limit. To compute the mean curvature, only first derivatives are involved, which is better than the radial parametrization in the sense of problem 2 from the beginning of this section. The Bernoulli equation can be represented now as

$$\left(\frac{\partial \phi_1}{\partial s} + \frac{\partial \phi_2}{\partial s} - \sin\theta(\alpha)\right)^2 + \frac{2}{F^2}\eta(\alpha) + \frac{2}{W}\left(\frac{s'(\alpha)}{\theta'(\alpha)} + \frac{\xi(\alpha)}{\sin\theta}\right) - C = 0, \quad \alpha \in [0,\pi]. \tag{2.6.8}$$

After formulating all the elements in the equations, we are ready to discuss how to discretize them and solve for the bubble shape. But before that, we need to analyze the singularities in the integrand to determine the numerical method for integration.

2.7 Analyzing the singularities

In (2.6.3), only Π_1 and Π_2 are singular when q approaches p due to a zero denominator in G. To understand the singularity better, let us first study the asymptotic expansion of $G[a,b,c,d]$ at such a singular point. The two elliptic integrals in (2.6.2) can be expanded around $-\infty$ as follows

$$\begin{aligned} K(z) &= \frac{\log(-z)}{2\sqrt{-z}}\left(1+\frac{1}{4z}+\frac{9}{64z^2}+\cdots\right)+\frac{1}{\sqrt{-z}}\left(\log 4+\frac{\log 4-1}{4z}+\frac{18\log 4-21}{128z^2}+\cdots\right),\\ E(z) &= \sqrt{-z}+\frac{1}{\sqrt{-z}}\left(\frac{1}{4}+\log 2+\frac{8\log 2-3}{64z}+\cdots\right)+\frac{\log(-z)}{4\sqrt{-z}}\left(1+\frac{1}{8z}+\frac{3}{64z^2}+\cdots\right). \end{aligned} \tag{2.7.1}$$

For $G[a_1,b_1,c_1,d_1]$ in Π_1, the leading terms in each expansions around $\alpha\in(0,\pi)$ are

$$\begin{aligned} c_1-d_1 &\sim (\xi'^2(\alpha)+\eta'^2(\alpha))(\beta-\alpha)^2 = s'^2(\alpha)(\beta-\alpha)^2,\\ -\frac{2d_1}{c_1-d_1} &\sim \frac{-4\xi^2(\alpha)}{s'^2(\alpha)(\beta-\alpha)^2},\\ b_1c_1-a_1d_1 &\sim \xi(\alpha)s'(\alpha)(s'(\alpha)\sin\theta-\xi(\alpha))(\beta-\alpha)^2. \end{aligned} \tag{2.7.2}$$

Combining with (2.7.1), we know that the leading term in $\frac{4b_1}{d_1\sqrt{c_1-d_1}}K(-\frac{2d_1}{c_1-d_1})$ is $\frac{2\sin\theta}{\xi(\alpha)}\log|\beta-\alpha|$, which is singular except when $\alpha=0$ or π due to $\xi(0)=\xi(\pi)=\theta(0)=\theta(\pi)=0$. The leading term in $-4\frac{(b_1c_1-a_1d_1)}{(c_1+d_1)d_1\sqrt{c_1-d_1}}E(-\frac{2d_1}{c_1-d_1})$ is $\frac{\xi(\alpha)-s'(\alpha)\sin\theta}{\xi^2(\alpha)s'(\alpha)}$. In other words, the integrand of Π_1 has a *log* type of singularity. When $\alpha=0$ or π, however, due to $\theta(0)=\theta(\pi)=\xi(0)=\xi(\pi)=\eta'(0)=\eta'(\pi)=0$, $b_1=d_1=0$. The integrand is smooth on $[0,\pi]$ because

$$\lim_{\alpha\to 0}\mu_1(\alpha)\xi(\alpha)s'(\alpha)G[a_1,b_1,c_1,d_1]=\frac{\pi\mu_1(0)s'(0)\eta''(0)}{\xi'^2(0)}<\infty,$$

which is the same case for $\alpha=\pi$.

Similarly, for $G[e_2,f_2,g_2,h_2]$ in Π_2, we have the following expansions around any fixed $z\in(-\infty,\infty)$

$$\begin{aligned} g_2-h_2 &= (y-z)^2,\\ -\frac{2h_2}{g_2-h_2} &= \frac{-4}{(y-z)^2},\\ f_2g_2-e_2h_2 &= -(y-z)^2. \end{aligned}$$

So the leading term in $\frac{4f_2}{h_2\sqrt{g_2-h_2}}K(-\frac{2h_2}{g_2-h_2})$ is $\log|y-z|$, and that in $-4\frac{(f_2g_2-e_2h_2)}{(g_2+h_2)h_2\sqrt{g_2-h_2}}E(-\frac{2h_2}{g_2-h_2})$ is $\frac{4}{(y-z)^2+4}$. All in all, the integrand of Π_2 also has a *log* type of singularity.

The last type of singularity happens when evaluating $\frac{\partial\phi}{\partial s}$ on S_1 which is needed to enforce the Bernoulli equation. To start, let us first understand how to swap the order of integration and differentiation in (2.6.6). When evaluating ϕ_1 on S_1, for any $p=(\xi(\alpha),0,\eta(\alpha))\in S_1$,

we abuse notation and write $\phi_1(\alpha) = \phi_1(p(\alpha))$. From (2.4.2), we have

$$\phi_1(\alpha) = \int_0^{\pi}\int_0^{2\pi} \frac{\mu_1(\beta)\xi(\beta)s'(\beta)}{4\pi\sqrt{c_1 - d_1\cos\varphi}}\, d\varphi d\beta = \int_0^{\pi} \frac{\mu_1(\beta)\xi(\beta)s'(\beta)K(-\frac{2d_1}{c_1-d_1})}{\pi\sqrt{c_1-d_1}}\, d\beta. \tag{2.7.3}$$

For $\alpha \in (0,\pi)$, as analyzed before, $\frac{K\left(-\frac{2d_1}{c_1-d_1}\right)}{\sqrt{c_1-d_1}}$ has leading term $-\frac{\log|\beta-\alpha|}{2\xi(\alpha)}$ when expanded around α. This leads to extra caution when interchanging the differentiation and integration when evaluating $\frac{\partial\phi_1}{\partial\alpha}$. To justify (2.6.6), it suffices to prove that the following holds

$$\frac{\partial}{\partial\alpha}\left(\int_{\alpha_1}^{\alpha_2} f(\beta)\log|\beta-\alpha|\, d\beta\right) = p.v.\int_{\alpha_1}^{\alpha_2}\frac{f(\beta)}{\beta-\alpha}\, d\beta, \tag{2.7.4}$$

for any $f(\beta)\in\mathcal{C}^1$ and $\alpha\in(\alpha_1,\alpha_2)\subset[0,\pi]$. Without loss of generality, we assume $\alpha_2-\alpha \geq \alpha-\alpha_1$. By definition,

$$\begin{aligned}
p.v.\int_{\alpha_1}^{\alpha_2}\frac{f(\beta)}{\beta-\alpha}\, d\beta &= \lim_{\epsilon\to0^+}\left(\int_{\kappa_1}^{\alpha-\epsilon} + \int_{\alpha+\epsilon}^{\kappa_2}\right)\frac{f(\beta)}{\beta-\alpha}\, d\beta \\
&= \lim_{\epsilon\to0^+}\left(\int_{\epsilon}^{\alpha_2-\alpha}\frac{f(\alpha+\gamma)}{\gamma}\, d\gamma - \int_{\epsilon}^{\alpha-\alpha_1}\frac{f(\alpha-\gamma)}{\gamma}\, d\gamma\right) \\
&= \lim_{\epsilon\to0^+}\int_{\epsilon}^{\alpha-\alpha_1}\frac{f(\alpha+\gamma)-f(\alpha-\gamma)}{\gamma}\, d\gamma + \int_{\alpha-\alpha_1}^{\alpha_2-\alpha}\frac{f(\alpha+\gamma)}{\gamma}\, d\gamma \\
&= \int_0^{\alpha-\alpha_1}\frac{f(\alpha+\gamma)-f(\alpha-\gamma)}{\gamma}\, d\gamma + \int_{\alpha-\alpha_1}^{\alpha_2-\alpha}\frac{f(\alpha+\gamma)}{\gamma}\, d\gamma.
\end{aligned}$$

The last equality holds because $\lim_{\epsilon\to0^+}\frac{f(\alpha+\epsilon)-f(\alpha-\epsilon)}{\epsilon} = 2f'(\alpha)$. On the other hand, we have

$$\begin{aligned}
&\frac{\partial}{\partial\alpha}\left(\int_{\alpha_1}^{\alpha_2} f(\beta)\log|\beta-\alpha|\, d\beta\right) \\
&\quad= \frac{\partial}{\partial\alpha}\left(\int_{2\alpha-\alpha_1}^{\alpha_2} f(\beta)\log|\beta-\alpha|\, d\beta + \int_{\alpha_1}^{2\alpha-\alpha_1} f(\beta)\log|\beta-\alpha|\, d\beta\right) \\
&\quad= \int_{2\alpha-\alpha_1}^{\alpha_2}\frac{f(\beta)}{\alpha-\beta}\, d\beta - 2f(2\alpha-\alpha_1)\log(\alpha-\alpha_1) + \frac{\partial}{\partial\alpha}\left(\int_{\alpha_1-\alpha}^{\alpha-\alpha_1} f(\alpha+\gamma)\log|\gamma|\, d\gamma\right) \\
&\quad= \int_{\alpha-\alpha_1}^{\alpha_2-\alpha}\frac{f(\alpha+\gamma)}{\gamma}\, d\gamma - 2f(2\alpha-\alpha_1)\log(\alpha-\alpha_1) \\
&\qquad+ \frac{\partial}{\partial\alpha}\left(\int_0^{\alpha-\alpha_1}(f(\alpha+\gamma)+f(\alpha-\gamma))\log|\gamma|\, d\gamma\right).
\end{aligned}$$

Since $f\in\mathcal{C}^1$ and $\log|\gamma|$ is integrable over any closed finite interval, by dominated convergence

we can move the differentiation inside the integral and apply integration by part to get

$$\begin{aligned}
&\frac{\partial}{\partial\alpha}\left(\int_{\alpha_1}^{\alpha_2} f(\beta)\log|\beta-\alpha|\,d\beta\right)\\
&\quad=\int_{\alpha-\kappa_1}^{\kappa_2-\alpha}\frac{f(\alpha+\gamma)}{\gamma}\,d\gamma-2f(2\alpha-\kappa_1)\log(\alpha-\kappa_1)\\
&\qquad+\int_0^{\alpha-\kappa_1}(f'(\alpha+\gamma)+f'(\alpha-\gamma))\log|\gamma|\,d\gamma+(f(2\alpha-\kappa_1)+f(\kappa_1))\log(\alpha-\kappa_1)\\
&\quad=\int_{\alpha-\kappa_1}^{\kappa_2-\alpha}\frac{f(\alpha+\gamma)}{\gamma}\,d\gamma-f(2\alpha-\kappa_1)\log(\alpha-\kappa_1)+f(\kappa_1)\log(\alpha-\kappa_1)\\
&\qquad+\lim_{\epsilon\to0}\int_\epsilon^{\alpha-\kappa_1}(f'(\alpha+\gamma)+f'(\alpha-\gamma))\log|\gamma|\,d\gamma\\
&\quad=\int_{\alpha-\kappa_1}^{\kappa_2-\alpha}\frac{f(\alpha+\gamma)}{\gamma}\,d\gamma-\lim_{\epsilon\to0^+}\int_\epsilon^{\alpha-\kappa_1}\frac{f(\alpha+\gamma)+f(\alpha-\gamma)}{\gamma}\,d\gamma\\
&\qquad-\lim_{\epsilon\to0}(f(\alpha+\epsilon)-f(\alpha-\epsilon))\log\epsilon\\
&\quad=\int_0^{\alpha-\kappa_1}\frac{f(\alpha+\gamma)-f(\alpha-\gamma)}{\gamma}\,d\gamma+\int_{\alpha-\kappa_1}^{\kappa_2-\alpha}\frac{f(\alpha+\gamma)}{\gamma}\,d\gamma.
\end{aligned}$$

The last equality is due to the fact that $\lim_{\epsilon\to0^+}\frac{f(\alpha+\epsilon)-f(\alpha-\epsilon)}{\epsilon}=2f'(\alpha)<\infty$ and the fact that $\lim_{\epsilon\to0^+}\big((f(\alpha+\epsilon)-f(\alpha-\epsilon)\big)\log\epsilon=\lim_{\epsilon\to0^+}2f'(\tilde\alpha)\epsilon\log\epsilon=0$ for some $\tilde\alpha\in[\alpha-\epsilon,\alpha+\epsilon]$, so the claim is proved and (2.6.6) is justified.

When $\alpha=0$ or π, due to $\xi(0)=\xi(\pi)=\theta(0)=\theta(\pi)=0$, the integrand in Π_3 from (2.6.6) does not have $\frac{1}{\beta}$-type singularity anymore, so we could ignore the Cauchy principal value integral. From the fact that $a_3(0)=d_1(0)=0$, by definition we have $G[a_3,b_3,c_1,d_1]=0$, resulting in $\frac{\partial\phi_1}{\partial s}(0)=0$. This can be proved rigorously by the theorem on exchanging limit and differentiation, i.e. if f_n converges to f pointwisely and f_n' converges to g uniformly, then f is differentiable and $f'=g$. Furthermore, it should not be surprising that velocity generated by charges on bubble surfaces is 0 at the stagnation points due to equal charge density on the same latitude. It is also easy to see geometrically that the velocity generated by changes on the tube and by the background flow is also 0 at the stagnation points.

Chapter 3

Numerical procedure and results

In this chapter, we discretize the HLS formulation and integrate the weak singularity with generalized Gaussian quadrature based on the singularity type discussed in Chapter 2. The $g = 0$ and $g \neq 0$ cases are discussed separately due to the symmetric nature of the problem when $g = 0$. The general numerical procedure is stated for the reader's convenience. Finally, we show the wall effect on small oblate bubbles and the existence of elongated bubbles when $g = 0$. No steady solution is found when $g \neq 0$. This case will be studied with a viscous boundary layer in Chapter 4, and for the inviscid time-dependent problem In Chapter 5.

3.1 Numerical discretization and integration

Now we are ready to explain the numerical procedure. First we make an initial guess of $\theta(\beta)$. Without loss of generality, we assume that β ranging voer $[0, 2\pi]$ covers the whole bubble surface. Instead of representing $\theta(\beta)$ directly, we find it easier to represent $\tilde{\theta}(\beta) = \theta(\beta) - \beta$ as it is a smooth periodic function, so we treat the Fourier modes of $\tilde{\theta}(\beta)$ as the variables we are solving for. To be precise, since $\tilde{\theta}(k\pi) = 0$ and $\tilde{\theta}(\beta)$ is odd around $k\pi$ for $k \in \mathbb{Z}$, its Fourier modes are purely imaginary and correspond to $\sin(k\beta)$ where k is the frequency. With $N + 1$ uniform grid points on $[0, \pi]$, we treat the coefficients before $\{\sin(k\beta)\}_{k=1}^{N-1}$ as the first $N - 1$ variables we are solving for. As for arc-length element $s'(\beta)$, due to the time-invariant nature of the problem, it is fixed as a constant σ to make sure that the grid points are uniformly distributed with respect to arc-length. The complete elliptic integrals in (2.6.2) are numerically integrated accurately in double precision using method of [13].

Knowing $\tilde{\theta}(\beta)$ and σ, we can get the shape of bubble surface using (3.1). With this, (2.6.3) can be evaluated at $\{\alpha_k\}_{k=0}^{N}$ where $\alpha_k = \frac{k\pi}{N}$ on S_1; whereas on S_2 evaluation points cannot be chosen uniformly due to the domain $(-\infty, \infty)$ being infinite. We use the transform $y = \cot\tau$ to map $\mathbb{R}$ to $(-\frac{\pi}{2}, \frac{\pi}{2})$. Geometrically, as shown in Figure 3.1, any $q = (1, 0, z) \in S_2$ is mapped to the radial angle τ between the positive z direction and the line connecting the

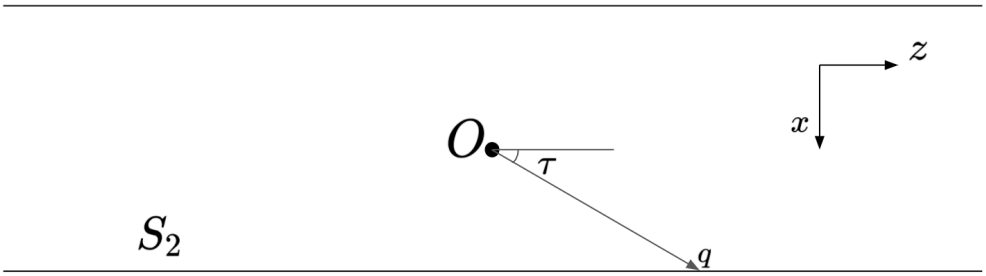

Figure 3.1: Transforming any point $q \in S_2$ to its angle representation τ.

origin O and q. Under this transformation, we obtain a new integral expression

$$\int_{-\infty}^{\infty} \mu_2(y) G[e, f, g, h](z, y)\, dy = \int_0^{\pi} \tilde{\mu}_2(\tau) G[e, f, g, h](\cot\omega, \cot\tau) \csc^2\tau\, d\tau, \tag{3.1.1}$$

where $\tilde{\mu}_2(\cdot) = \mu_2(\tan(\cdot))$ and $z = \cot\omega$. From now on, we think of μ_2 being parametrized by radial angle τ by default and abuse the notation to write it as $\mu_2(\tau)$. We use a Chebyshev-Gauss grid $\{\omega_k\}_{k=1}^M$ on $(0, \pi)$ as the new evaluation points to enforce the second equation in (2.6.3). One caveat is that we represent $\mu_2(\tau)$ using Chebyshev polynomials of degree greater than 0, not including the constant polynomial. This is because the constant polynomial is the one-dimensional kernel of (2.6.3) as shown in Section 2.5.

Treating the $N+1$ Fourier modes of $\mu_1(\beta)$ and the M Chebyshev modes (the coefficients before Chebyshev polynomials of degree 1, $2, \cdots, M$) of $\mu_2(\tau)$ as the $N+M+1$ variables we are solving for, the evaluation of (2.6.3) at $\{\alpha_k\}_{k=0}^N$ and $\{\omega_k\}_{k=1}^M$ gives $N+M+1$ defining equations. $\mu_1(\beta)$ and $\mu_2(\tau)$ are then uniquely constructed. To be more precise, since μ_1 is symmetric about $k\pi$ for any integer k, the $N+1$ Fourier modes only contain real parts, which correspond to the coefficients before $\{\cos(k\pi)\}_{k=0}^N$.

With all the grid points on S_1 and S_2 chosen as above, to numerically evaluate all the above integrals defined on $(0, \pi)$, we first integrate them on each panels, i.e. $\{(\alpha_j, \alpha_{j+1})\}_{j=0}^{N-1}$ for integrations on S_1, and $\{(\omega_j, \omega_{j+1})\}_{j=1}^{M-1}$ for integrations on S_2, and then add all these N sub-integrals and $M-1$ sub-integrals together respectively. For regular integrals, the integrand can be well approximated on each panels by Legendre polynomials, so we use classical Gaussian quadrature to integrate on panels. Singular integrals, however, must be treated differently.

Due to the singularities discussed in the last section, Π_1 and Π_2 should be treated differently from the others. For the other two integrals, since they have smooth integrands, on each subinterval (α_{k-1}, α_k) and (ω_{k-1}, ω_k), the integrand can be approximated well by polynomials and we can use classical Gaussian quadrature to integrate.

For Π_1 in (2.6.3), suppose we are evaluating it with $\alpha = \alpha_k$, when integrating on (α_{k-1}, α_k) and (α_k, α_{k+1}), due to the singularity at θ_k, we need to approximate the integrand by $\{1, \log|\alpha - \alpha_k|, \alpha, \alpha\log|\alpha - \alpha_k|, \alpha^2, \alpha^2\log|\alpha - \alpha_k|, \cdots\}$, which can be done using generalized Gaussian quadrature with log type of singularity [31]. For integration on non-adjacent subintervals, we still use classical Gaussian quadrature to approximate the integral. When $k = 0$ or N though, the integrand on adjacent subinterval is smooth as we analyzed before, so classical Gaussian quadrature is applied to all the subintervals.

Π_2 in (2.6.3) is dealt with similarly when the evaluation point ω_k is close to the middle of $(0, \pi)$. When ω_k is close to 0 or π, however, $\cot\omega$ might be very far from $\cot\tau$ even though ω and τ are close, so we subdivide the adjacent sub-intervals (ω_{k-1}, ω_k) into two parts $(\omega_{k-1}, \omega_{k-1} + \sin^2\omega_k)$ and $(\omega_{k-1} + \sin^2\omega_k, \omega_k)$. We use classical Gaussian quadrature for the first part as usual due to the smoothness of integrand. For the second part, we subtract the singularity $\mu_2(\omega_k)\log|\cot\omega_k - \cot\tau)|\csc^2\tau$ in the integrand and then add it back. The new integral can be approximated by classical Gaussian quadrature, and then we add back

$$\int_{\omega_{k-1}+\sin^2\omega_k}^{\omega_{k-1}} \mu_2(\omega_k)\log|\cot\omega_k - \cot\tau|\csc^2\tau\, d\tau = -\mu_2(\omega_k)l(\log|l| - 1),$$

with $l = \cot(\omega_{k-1} + \sin^2\omega_k) - \cot(\omega_{k-1})$. This singularity subtraction trick can also be applied to (ω_k, ω_{k+1}) similarly.

Here we present in Figure 3.2 the μ_1 and μ_2 solutions of (2.6.3) solved in the above numerical scheme. With $N = M = 120$, the Fourier modes of μ_1 decay down to 10^{-12}, but the Chebyshev modes only decay to 10^{-6}. Increasing N will make the Fourier modes decay even more, but increasing M will not make the Chebyshev modes decay more. From Figure 3.2 we see that at $\tau = 0$ and $\tau = \pi$, $\mu_2(\tau)$ seems to have a log type of singularity. A function with singularities at the endpoints cannot be approximated well by Chebyshev expansions, thus making the Chebyshev modes not decay to round-off error with M big enough. Notice that for different bubble shapes, we do not have a systematic way to recognize endpoint singularity of μ_2 yet. Since the endpoint singularity of μ_2 is very far from the bubble physically in the lab frame, it will have a small influence on the bubble shape. So we stick to the above numerical scheme at this point.

After solving for μ_1 and μ_2, we define the error to be the evaluation of the left hand side of the Bernoulli equation at $\{\alpha_k\}_{k=0}^N$ subtracted by a constant C, which is another input variable. One caveat is evaluating the Cauchy principal value in Π_3 when $k \neq 0, N$. Again we use the same 'subtract the singularity' trick on intervals adjacent to α_k, i.e. $(\alpha_{k-1}, \alpha_{k+1})$

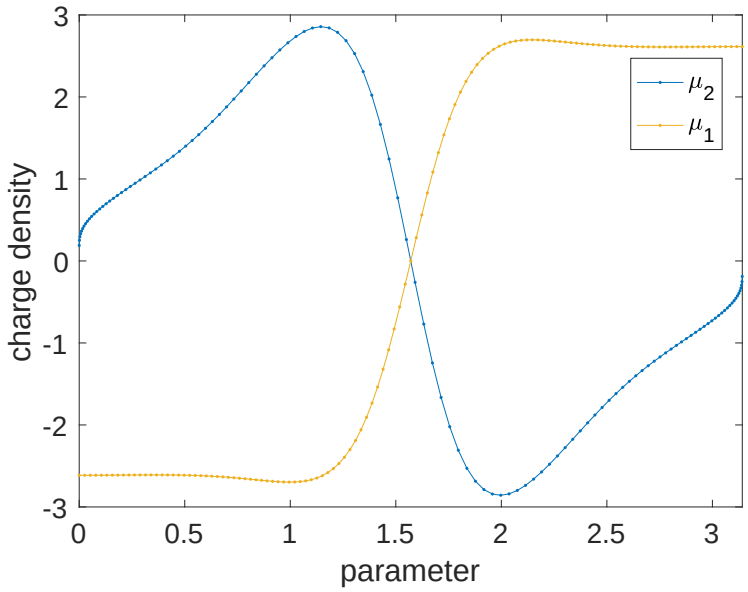

Figure 3.2: $\mu_1(\alpha)$ with $\alpha \in [0, \pi]$ on a round bubble of radius 0.9 and $\mu_2(\tau)$ with $\tau \in [0, \pi]$ on the infinite tube solved with $N = M = 120$ when Neumann conditions are satisfied on S_1 and S_2.

as below:

$$
\begin{aligned}
p.v. \int_{\alpha_{k-1}}^{\alpha_{k+1}} \sigma\mu_1(\beta)\xi(\beta)G[a_3, b_3, c_1, d_1]\, d\beta &= p.v. \int_{\alpha_{k-1}}^{\alpha_{k+1}} \frac{\sigma\mu_1(\beta)\xi(\beta)h(\alpha_k, \beta)}{\beta - \alpha_k}\, d\beta \\
&= \sigma\Big(\int_{\alpha_{k-1}}^{\alpha_{k+1}} \frac{\mu_1(\beta)\xi(\beta)h(\alpha_k, \beta) - \mu_1(\alpha_k)\xi(\alpha_k)h(\alpha_k, \alpha_k)}{\beta - \alpha_k}\, d\beta + \mu_1(\alpha_k)\xi(\alpha_k)h(\alpha_k, \alpha_k) \\
p.v. \int_{\alpha_{k-1}}^{\alpha_{k+1}} \frac{1}{\beta - \alpha_k}\, d\beta \Big) &= \sigma \int_{\alpha_{k-1}}^{\alpha_{k+1}} \frac{H(\alpha_k, \beta) - H(\alpha_k, \alpha_k)}{\beta - \alpha_k}\, d\beta,
\end{aligned}
\tag{3.1.2}
$$

where $h(\alpha_k, \beta) = (\beta - \alpha_k)G[a_3, b_3, c_1, d_1](\alpha_k)$ and $H(\alpha_k, \beta) = \mu_1(\beta)\xi(\beta)h(\alpha_k, \beta)$. Notice the integrand $\frac{H(\alpha_k,\beta)-H(\alpha_k,\alpha_k)}{\beta-\alpha_k}$ does not have a $\frac{1}{\beta-\alpha_k}$-type singularity anymore, but it still has a log singularity around α_k, so we again use the generalized Gaussian quadrature to evaluate the integral. Since the interval $(\alpha_{k-1}, \alpha_{k+1})$ is symmetric about a_k, $\frac{H(\alpha_k,\alpha_k)}{\beta-\alpha_k}$ contribute nothing to the Gaussian quadrature integration due to the symmetry of quadrature grids around α_k. It means we only need to evaluate $\frac{H(\alpha_k,\beta)}{\beta-\alpha_k}$ when using generalized Gaussian quadrature.

3.2 Numerical procedure

After the detailed discussion on discretizing the problem and integrating accurately, we are ready to introduce the whole procedure on solving for a numerical solution of a steady rising

bubble.

With σ fixed, our goal is to find the unknown function $\tilde{\theta}(\beta)$ such that the corresponding velocity potential generated by the layer potential theory satisfies the Bernoulli equation. Given an initial guess of $\tilde{\theta}(\beta)$ and Bernoulli constant C, the bubble surface is reconstructed using (3.1). μ_1 and μ_2 are then solved by (2.6.3). Lastly, the value of evaluating the left-hand-side of (2.6.8) is the error we want to minimize. When the error is 0, we get one solution.

Since the problem is very non-linear, we use the Levenberg Marquardt algorithm [40] [51]. This algorithm combines gradient descent and Newton's method in a trust-region framework. It has the advantage that the algorithm can still converge to the solution even with a poor initial guess, and the final iterations converge quadratically for zero-residue problems. The most time-consuming step is computing the approximate Jacobian matrix of the whole problem by finite difference.

Since we represent and solve the solutions 'with and without gravity' cases differently, we discuss the detailed numerical procedure separately as follows.

Without gravity

First, we study the bubble shape when there is no gravity, i.e. Froude number $F = \infty$. In this case, the Bernoulli equation is simplified to be

$$\Big(\frac{\partial \phi_1}{\partial s} + \frac{\partial \phi_2}{\partial s} - \sin\theta(\alpha)\Big)^2 + \frac{2}{W}\Big(\frac{s'(\alpha)}{\theta'(\alpha)} + \frac{\xi(\alpha)}{\sin\theta}\Big) - C = 0, \quad \alpha \in [0, \pi].$$

Suppose $\phi(x, y, z) = \phi_1(x, y, z) + \phi_2(x, y, z) - z$ is a solution to (2.2.2). It is easy to show that $-\phi_1(x, y, -z) - \phi_2(x, y, -z) - z$ will also be a solution to the system if $(x, y, z) \in \mathcal{D}$ means $(x, y, -z) \in \mathcal{D}$, i.e. if S_1 is symmetric about $\alpha = \frac{\pi}{2}$. Solving for bubble shape that is symmetric about $\alpha = \frac{\pi}{2}$ we assume both N and M are even. In this case, $\tilde{\theta}(\beta)$ is odd about $(k + \frac{1}{2})\pi$ and $k\pi$ for all $k \in \mathbb{Z}$. We expect $\xi(\beta)$ to be even about $(k + \frac{1}{2})\pi$ and $k\pi$ for all $k \in \mathbb{Z}$. Setting $\eta(\frac{\pi}{2}) = 0$, $\eta(\beta)$ is odd about $(k + \frac{1}{2})\pi$ and even about $k\pi$ for all $k \in \mathbb{Z}$. Except for the obvious fact that $\mu_1(\beta)$ is even about $k\pi$ for any $k \in \mathbb{Z}$, from (2.6.3) we see that $\mu_1(\beta)$ and $\mu_2(\tau)$ must be odd about $\beta = (k + \frac{1}{2})\pi$ and $\tau = \pi/2$ respectively.

With all the symmetries above, the unknown variables will be the $\frac{N}{2} - 1$ even Fourier sine modes of $\tilde{\theta}(\beta)$, i.e. coefficients before $\{\sin(2k\beta)\}_{k=1}^{\frac{N}{2}-1}$, and also the Bernoulli constant C. So there are in total $\frac{N}{2}$ unknown real numbers to find. Given an initial guess of these $\frac{N}{2}$ real numbers, we treat the odd Fourier cosine modes of μ_1 and μ_2 as intermediate variables, which can be solved by evaluating (2.6.3) only at grid points with positive z due to symmetry, i.e. $\{a_k\}_{k=0}^{N/2-1}$ and $\{\omega_k\}_{k=1}^{M/2}$. All the other constants, i.e the arc-length element σ and Weber number W, are fixed. Later we will see that the problem size is cut into half relative to that of the general case with gravity.

With gravity

For the general case when gravity is non-zero, we lose the symmetry about $\beta = \frac{\pi}{2}$ of the problem due to the $\frac{2}{F^2}z$ term in the Bernoulli equation. Now with $\tilde{\theta}(\beta)$ being odd only about $k\pi$ for all $k \in \mathbb{Z}$, the unknown variables will be the $N-1$ Fourier sine modes of $\tilde{\theta}(\beta)$, i.e. the coefficients before $\{\sin(k\beta)\}_{k=1}^{N-1}$, and also the Bernoulli constant C. One caveat is that not every $\tilde{\theta}(\beta)$ of the above form gives us a legitimate profile curve. This is because $\xi(\pi) = 0$ is not guaranteed in the non-symmetric case. With σ fixed as in the $g = 0$ case, $\xi(\pi) = 0$ is equivalent to imposing $\int_0^\pi \cos(\theta(\beta))\, d\beta = 0$. Notice that not every $\theta(\beta)$ satisfies this. To make this happen, we abuse notation and split the periodized tangent angle into two parts, one part consisting of all sine series terms with frequency higher then 1, denoted by $\tilde{\theta}(\beta)$, and another another part $c_0 \sin\beta$, i.e. the first Fourier modes. We then impose the following condition:

$$\int_0^\pi \cos(\theta(\beta))\, d\beta = \int_0^\pi \cos(\tilde{\theta}(\beta) - \beta + c_0 \sin\beta)\, d\beta = 0. \tag{3.2.1}$$

Given any $\tilde{\theta}(\beta)$ that is periodic and odd around $k\pi$, we solve for c_0 by first integrating (3.2.1) using the Trapezoidal rule and then using Newton's iterations to solve it. After the projection, we treat $\theta(\beta) = \tilde{\theta}(\beta) - \beta + c_0 \sin\beta$ as the tangential angle and all the calculations start from here.

The oddness of $\tilde{\theta}(\beta)$ about $k\pi$ still holds here, and we treat the $N-2$ imaginary Fourier modes of $\tilde{\theta}(\beta)$ with frequency between 2 and $N-1$ (i.e. the coefficients before $\{\sin(k\beta)\}_{k=2}^{N-1}$) as free variables. Intermediately, we need to calculate the first mode c_0 as discussed above to enforce (3.2.1). Combined with the Bernoulli constant C, and the Weber number W, there are N variables in total, with $N+1$ residues from evaluating (2.6.8) at $\{\alpha_k\}_{k=0}^{N}$. The arc-length element σ and Froude number F are treated as fixed constants. Although the problem seems overdetermined, increasing the grid number N and M until spectral accuracy is achieved should still capture the solution using Levenberg-Marquardt algorithm if one exists.

3.3 Numerical solution branches

Several constants control the solutions implicitly. The constant arc-length element σ, which is equivalent to the length of the bubble surface profile curve; the Froude Number F; and the Weber number W; To see under what relation between these constants there exists a solution, we first fix F and start with small σ and gradually increase it using numerical continuation. Since the Fourier modes of $\tilde{\theta}$ are the variables we are solving for in the Levenberg-Marchquet algorithm, we say we get a legitimate numerical solution if the Fourier modes decay and the Bernoulli equation evaluation errors at N grid points are in order of 10^{-9} on average.

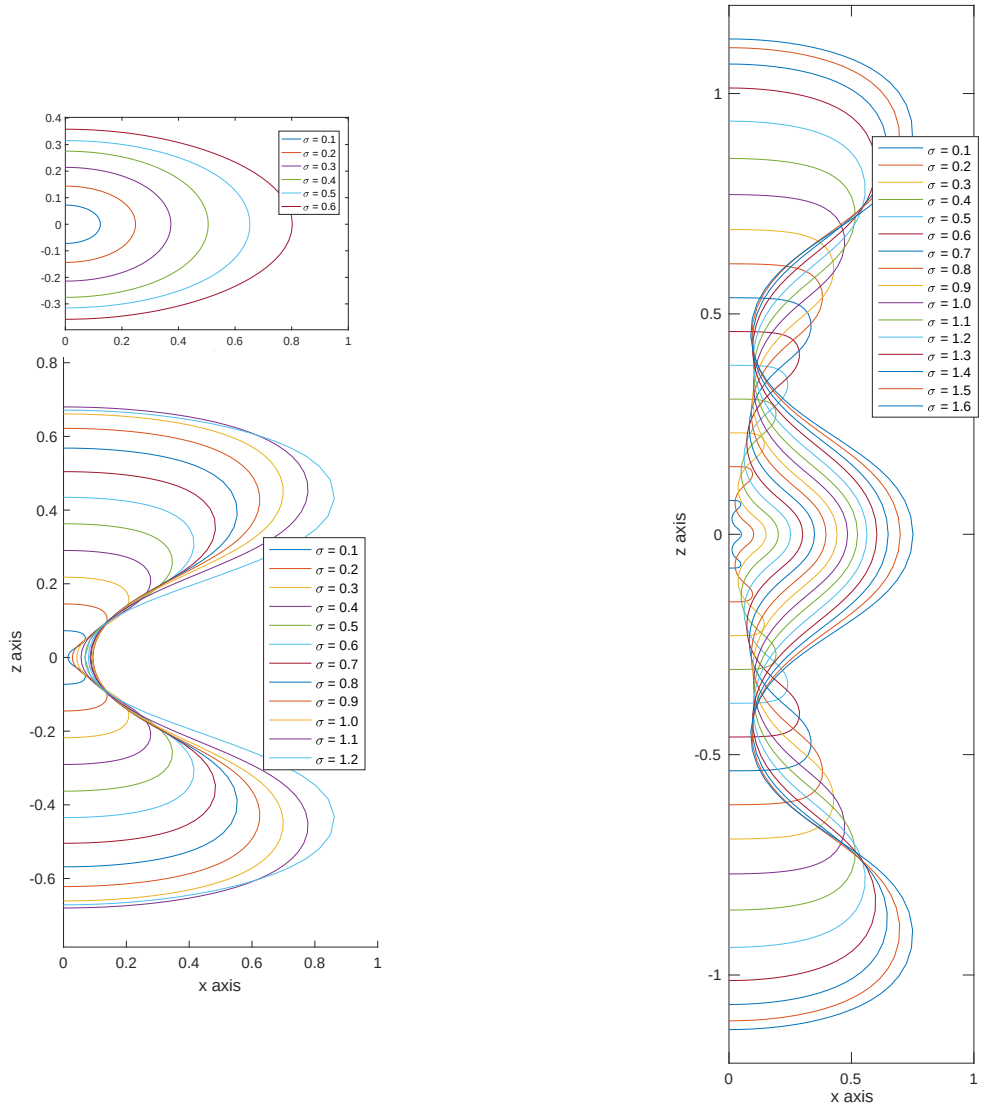

Figure 3.3: The right-hand side cross-sectional profile curve of a steadily rising bubble with one (top left), two (bottom left), and three (right) humps. The infinitely long tube wall is always placed at $x = 1$ and the far-field background flow is normalized to $U = -1$.

Without gravity

The case $g = 0$ corresponds to an infinite Froude number $F = \infty$, so we are left with two constants, the arc-length element σ, which controls the profile curve length of the bubble, and the Weber number W. We wish to determine under what relation of these two constants there exists a solution.

Each curve in Figure 3.3 represents the right-hand side cross-sectional shape of a bubble

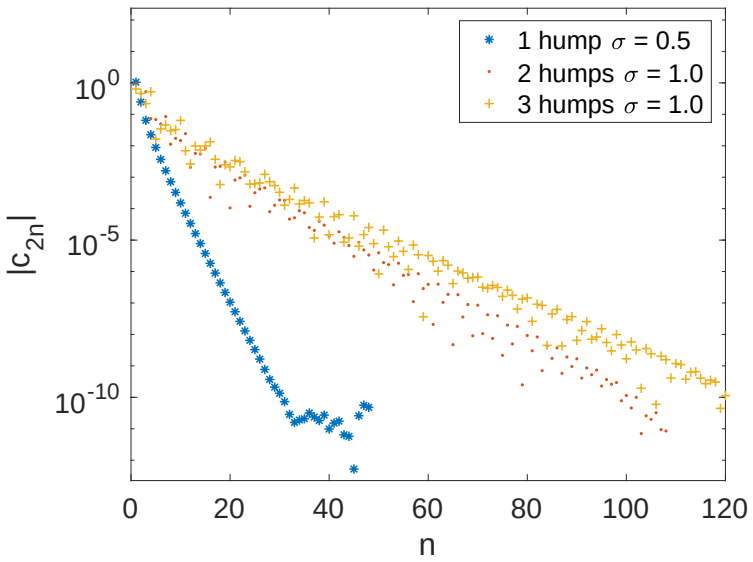

Figure 3.4: The magnitude of even Fourier modes $|c_{2n}|$ of $\tilde{\theta}(\alpha)$ with $2n$ the even frequency versus n in the no gravity case. Each relation corresponds to one representative from each solution branch, i.e. $\sigma = 0.5$ from the one hump case, and $\sigma = 1.0$ from the cases with two and three humps.

rising steadily at unit speed inside the potential flow filled in an infinitely long tube. The top left panel in Figure 3.3 shows the solution branches of a small oblate bubble with arc length element σ increasing from 0.1 to 0.6. We start with a sphere with $\sigma = 0.1$ as the initial guess, and get one solution with $\sigma = 0.1$. By increasing σ gradually, new curves are found by numerical continuation. Similarly in the bottom left panel and the right panel, each curve corresponds to a steady shape with different σ ranging from 0.1 to 1.2 and 0.1 to 1.6 respectively. Numerically, to make Fourier modes of $\tilde{\theta}$ decrease to the round-off error, we need more and more grid points on S_1. This can be illustrated in Figure 3.4 from the exponential decay of the Fourier modes magnitude of $\tilde{\theta}(\alpha)$ with one hump ($\sigma = 0.5$), two humps ($\sigma = 1.0$) and three humps ($\sigma = 1.0$). We let $N = 96$ in the 'one-hump case', $N = 216$ in the 'two-humps case' and $N = 240$ in the 'three-humps case'. As the number of humps increases, the Fourier modes magnitude decays more slowly. 120 MPI threads have been used to run the problem in the 'three-humps case', so to obtain the full decay of the Fourier modes, larger N and more MPI threads need to be used. Notice that in all three cases, σ cannot be increased indefinitely due to the wall at $x = 1$. As σ becomes larger, the effect of the wall pushing the bubble away from it becomes bigger, making it harder to find a convergent solution. If we insist on fixing σ to be larger than the threshold in the current branch, the searching will be pushed to another solution branch with a higher number of humps. Very likely, the Levenberg-Marquardt algorithm will land on a curve with one more hump than the current one. Interestingly, on each solution branch, the Weber number W

decreases continuously as σ increases.

For a fixed number of humps and a fixed σ, we can only get one smooth bubble shape numerically. To be precise, when N is not big enough and Fourier modes of $\tilde{\theta}$ only decay to 10^{-6}, numerically we can get several bubble shapes characterized by different Bernoulli constant C. As we increase N however, all these numerical solutions 'converge' to a smooth solution with a small C. But theoretically, there still might exist other solution branches for a fixed number of humps.

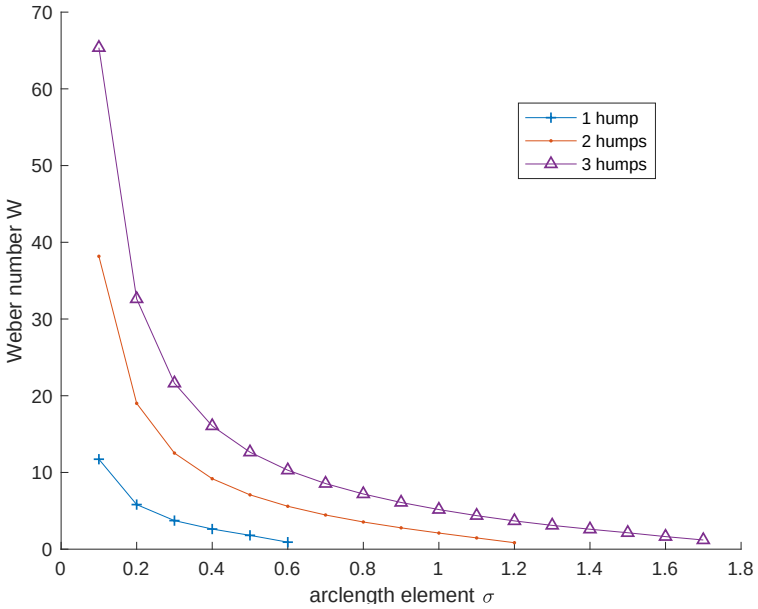

Figure 3.5: Three solution branches of different bubble shapes(1, 2, and 3 humps) relating σ and W obtained from numerical continuation.

Figure 3.5 demonstrates the above three solution branches relating W and σ. Since with a fixed number of humps, σ cannot be increased indefinitely, all solution branches are not infinitely extendable to the right and there must be an endpoint to each of them. We can see that these solutions look similar to unduloid, which is a type of constant-mean-curvature surface [10]. We can think of our solution shapes as a compact modification of them. Since an unduloid can be extended with any number of humps, we believe that for a fixed number of humps there exists at least one solution branch. If this is true, there must be infinitely many solution branches. Bubbles with more humps need to be represented by more Fourier modes to get the accuracy, and so far we do not have enough time to search for other solution branches with a higher number of humps. If we randomly choose a (σ, W) pair very close to a solution branch, the Levenberg-Marquardt algorithm will not converge to a solution. This makes us believe that the union of all these solution branches does not cover the whole (σ, W) plane and that for a fixed T, there are countably infinitely many bubbles that can rise steadily with unit speed. The Swift-Hohenberg equation with cubic and quintic

nonlinearities also has an infinite hierarchy of solution branches with a different number of humps [5].

With gravity

Using the results from the no gravity case and increasing g slowly, we find no convergent solution no matter how small the gravity is, with or without the tube wall S_2. This means that under the current inviscid model, bringing in gravity breaks the symmetry of the bubble and the kinetic energy and the surface tension stress cannot be balanced on the entire bubble surface. We will demonstrate the dynamics of an initially symmetric bubble under this setup in Chapter 5 to see how gravity affects its shape and movement.

Wall effect

The results in the previous two subsections concern a bubble in an infinitely long tube, and here we show the wall effects on the existence of a steadily rising bubble. We will compare the shape of the steadily rising bubble with and without an infinitely long tube S_2. When there is no tube, the bubble rises in open water, for example a big water tank or the ocean. When there is gravity, no solution is found without wall. When there is no gravity, we treat the solution from the wall case as the initial guess and search for solution in the case of no wall. Since our goal is to compare the solutions for these two cases, we still choose the imaginary tube radius H as the reference length even without a tube. Surprisingly for open

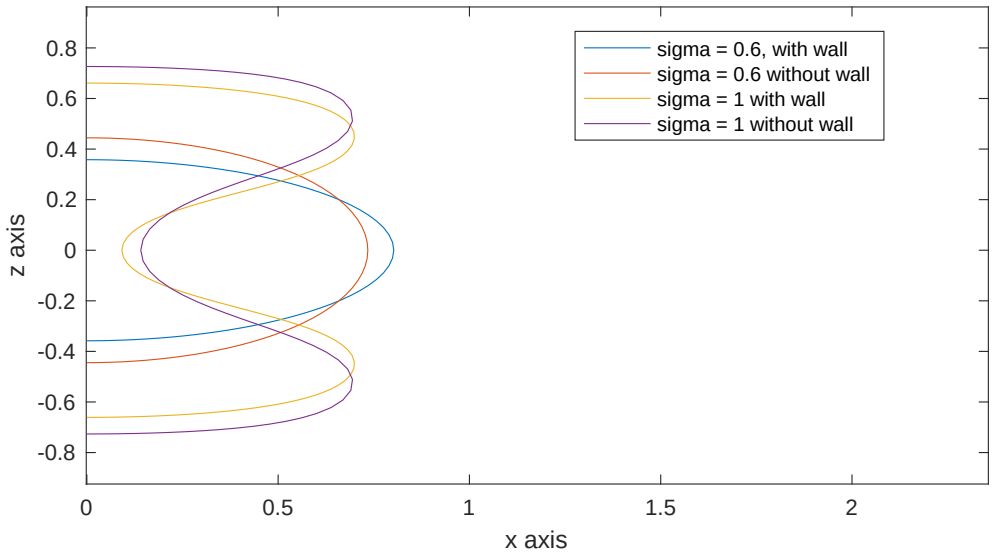

Figure 3.6: Comparison of steadily rising bubbles shapes with or without wall at $x = 1$.

water we also get rising bubbles with more than one hump using numerical continuation.

The fluid still accelerates around the outer oscillations and is pulled in by surface tension there, and is slowed down and pushed back out by surface tension near the inner oscillations of the bubble shape. In Figure 3.6, we show two steady-rising-bubble shapes without a wall with different arc-length element σ, obtained by numerical continuation. The other two curves are the corresponding initializations which are also the steady-rising bubble shapes in the case of a wall. We see that the tube bubble is more oblate than the open water bubble. For the other two constant variables, the Bernoulli constant C and the Weber number W, C is smaller with the wall than without, but W is larger. In this thesis, we concentrate on the bubble movement inside the infinitely long vertical tube, so from now on all the bubbles shown are in the presence of a wall unless stated otherwise.

3.4 Time complexity and parallel computing

The most time-consuming part of the problem lies in computing the Jacobian matrix, which requires $\mathcal{O}\big(n(M+N+1)^4\big)$ flops in the serial version for the general case when $g \neq 0$. Here $N+1$ and M are the number of Fourier and Chebyshev modes, and n is the maximum number of quadrature grids on a panel. If we run the serial program on a single machine with 10^9 FLOPS, with $M+N=70$ and $n=40$, it will take roughly one second to calculate the Jacobian matrix ignoring the big constant in complexity contributed from calculating elliptic integrals K and E. But to get spectral accuracy, 35 nodes in the right half of the profile curve is not enough.

We use OpenMP and MPI to parallelize the serial version. Since OpenMP does not scale as well as MPI when there are many threads, we use MPI for calculating the Jacobian matrix and each thread takes care of one column naturally by using finite difference approximation without affecting other computations on other threads. The time that takes the program to finish varies with the problem size and the initial guess that we give it. If the initial guess is close to the local minimum, only one or two Jacobian evaluations are required and within several minutes a convergent solution will be found with $N = 120$ and $M = 72$. However with the same number of grid points, if the initial guess is too far away from the solution, the program can take up to five hours before failing to find the solution.

Chapter 4

The viscous model

4.1 Introduction

Using the inviscid potential flow model of Chapter 2 and 3, we have not found any numerical solutions with non-zero gravity. This implies that according to our initial formulation, the surface tension force, gravitational force, and dynamic pressure cannot be balanced throughout the bubble surface. One element missing from our idealized model is the effect of viscosity — no fluids (aside from superfluid helium) are inviscid in practice. At high Reynolds number, viscous effects may be insignificant throughout large regions of the flow field and these regions may be treated as if the fluid were inviscid. However, the effect of viscosity must in general be taken into account in thin layers adjacent to boundaries in the flow. The essence of boundary layer theory in fluid mechanics, applicable only at high Reynolds number, is that viscous effects are considered to be restricted to thin layers called boundary layers and that certain simplifications can be made in the boundary layer because of its thinness [7] [42]. In addition to distorting the bubble, gravity exerts a buoyancy force on it, and a steady bubble is possible only if the flow exerts on it an opposite drag force. This force is supplied partially by the viscous stress. So even though our primary interest is in the effect of gravity, we still need to include viscosity stress in our equation in order to find steadily rising bubbles with $g > 0$.

4.2 Mathematical formulation

With the notion of 'viscous potential flow', following the convention from [35], we only need to change the Bernoulli equation (2.1.4) to be

$$\frac{1}{2}\rho|\nabla\tilde{\phi}|^2 + \rho g\tilde{z} + \tilde{\kappa}T + 2\rho\nu\frac{\partial\tilde{u}}{\partial\mathbf{n}} = \text{constant},$$

where $\frac{\partial\tilde{u}}{\partial\mathbf{n}} = \frac{\partial^2\tilde{\phi}}{\partial\mathbf{n}^2}$ is the normal derivative of the normal velocity $\tilde{u}$ on the bubble surface, and ν the kinematic viscosity. We neglect shear stresses in the air so that a constant pressure

normal stress is still imposed on the fluid at the boundary [27]. The new term capturing the normal component of the normal viscous stress contributes to the equilibrium bubble shape. Using the same non-dimensionalization transfrom as in Chapter 2, we get the dimensionless version

$$|\nabla\phi|^2 + \frac{2}{F^2}z + \frac{2}{W}\kappa + 4\nu\frac{\partial^2\phi}{\partial\mathbf{n}^2} = C \quad \text{on } S_1. \tag{4.2.1}$$

With this small modification, the rest of the single layer potential formulation remains unchanged when solving for the charge densities on S_1 and S_2. Now let us compute $\frac{\partial^2\phi}{\partial\mathbf{n}^2}$ in the HLS framework. Due to ϕ being harmonic on $\mathcal{D}$, at any fixed point $p = (\xi(\alpha), 0, \eta(\alpha)) \in \zeta$, in the local cartesian coordinate system oriented along the vectors $\mathbf{n} = (-\sin\theta(\alpha), 0, \cos\theta(\alpha))$, $\mathbf{t} = (\cos\theta(\alpha), 0, \sin\theta(\alpha))$ and $\mathbf{e} = (0, 1, 0)$ we have

$$\frac{\partial^2\phi}{\partial\mathbf{n}^2} + \frac{\partial^2\phi}{\partial\mathbf{t}^2} + \frac{\partial^2\phi}{\partial\mathbf{e}^2} = 0.$$

So to find $\frac{\partial^2\phi}{\partial\mathbf{n}^2}$, it suffices to compute $-\frac{\partial^2\phi}{\partial\mathbf{t}^2} - \frac{\partial^2\phi}{\partial\mathbf{e}^2}$. We first relates the $\frac{\partial^2\phi}{\partial\mathbf{t}^2}$ with the second derivative of velocity potential restricted on profile curve $\zeta(\alpha)$. We have

$$\frac{1}{\sigma}\frac{\partial\phi(\zeta(\alpha))}{\partial\alpha} = \nabla\phi(\zeta(\alpha))\cdot\frac{\zeta'(\alpha)}{\sigma} = \nabla\phi(\zeta(\alpha))\cdot\mathbf{t}$$

and

$$\frac{1}{\sigma^2}\frac{\partial^2\phi(\zeta(\alpha))}{\partial\alpha^2} = \frac{1}{\sigma}\frac{\partial}{\partial\alpha}\big(\nabla\phi(\zeta(\alpha))\cdot\mathbf{t}\big) = \mathbf{t}'\mathbf{H}_\phi\mathbf{t} + \nabla\phi(\zeta(\alpha))\cdot\frac{\theta'(\alpha)\mathbf{n}}{\sigma} = \frac{\partial^2\phi}{\partial\mathbf{t}^2}, \tag{4.2.2}$$

where $\mathbf{H}_\phi$ is the Hessian of ϕ and the fact $\frac{\partial\phi}{\partial\mathbf{n}} = 0$ is used in the last equality. Similarly we relates the $\frac{\partial^2\phi}{\partial\mathbf{t}^2}$ with the second derivative of velocity potential restricted on the circle of latitude $\gamma(\varphi) = \big(\xi(\alpha)\cos\varphi, \xi(\alpha)\sin\varphi, \eta(\alpha)\big)$. We have

$$\frac{1}{\xi(\alpha)}\frac{\partial\phi(\gamma(\varphi))}{\partial\varphi}\Big|_{\varphi=0} = \nabla\phi(\gamma(0))\cdot\frac{\gamma'(0)}{\xi(\alpha)} = \nabla\phi(\gamma(\varphi))\cdot\mathbf{e}$$

and

$$\begin{aligned}\frac{1}{\xi^2(\alpha)}\frac{\partial^2\phi(\gamma(\varphi))}{\partial\varphi^2}\Big|_{\varphi=0} &= \frac{1}{\xi(\alpha)}\frac{\partial}{\partial\varphi}\big(\nabla\phi(\gamma(\varphi))\cdot(-\sin\varphi,\cos\varphi,0)\big)\Big|_{\varphi=0}\\ =\mathbf{e}'\mathbf{H}_\phi\mathbf{e} + \frac{\nabla\phi(\gamma(0))\cdot(-1,0,0)}{\xi(\alpha)} &= \frac{\partial^2\phi}{\partial\mathbf{e}^2} - \frac{\partial\phi}{\partial\mathbf{t}}\frac{\cos\theta(\alpha)}{\xi(\alpha)} = 0,\end{aligned} \tag{4.2.3}$$

where the last equality is due to $\phi(\gamma(\varphi))$ being a constant function by axisymmetry. Combining (4.2.2) (4.2.3) we have the final expression

$$\frac{\partial^2\phi}{\partial\mathbf{n}^2}(p) = -\frac{1}{\sigma^2}\frac{\partial^2\phi(\zeta(\alpha))}{\partial\alpha^2} + \frac{\cos\theta(\alpha)}{\sigma\xi(\alpha)}\frac{\partial\phi(\zeta(\alpha))}{\partial\alpha}. \tag{4.2.4}$$

Numerically, derivatives with respect to α are easy to compute using the FFT. Notice that when $\alpha = 0$ or π, after applying L'Hospital's rule to the second part, both terms cancel and the normal viscous stress vanishes at the two stagnation points.

4.3 Numerical solution

We use the steady shape for the $g = 0$ case from Chapter 3 as an initial guess, and treat viscosity as an unknown that is solved for along with the bubble shape using the Levenberg-Marquardt method. There are four constants that control the physics: the Froude number F, the Weber number W, the kinematic viscosity ν, and the arc-length element σ. We fix F and σ, and solve for the bubble shape with W and ν being variables. Figure 4.1 shows the change of the steadily rising bubble as F goes down from infinity.

5.2.

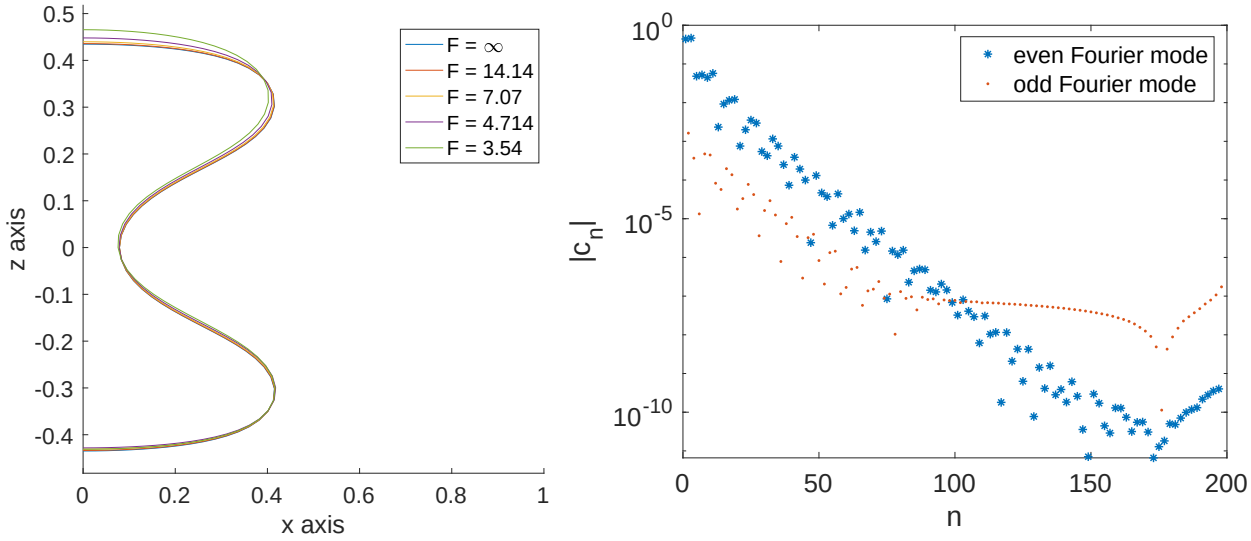

Figure 4.1: Right-hand cross-sectional profile of a steadily rising bubble for several values of the Froude number F (left) and the decay of Fourier modes $|c_n|$ $(1 \leq n \leq 198)$ of $\tilde{\theta}(\alpha)$ when $F = 14.14$ with $N = 200$ and $M = 120$ (right).

We start with a symmetric bubble with $\sigma = 0.6$, which is a steady solution of the zero gravity case. Treating W and ν as unknowns, decreasing F when F is large will change the solution very little. When F is small, however, the solution is very sensitive to changes in F. Both W and ν become bigger as F increases. The Bernoulli equation error goes down to 10^{-9} on average and the Fourier modes of these bubble shapes decrease to 10^{-6} with $N = 72$ and $M = 60$. However, if M and N are increased, the odd Fourier modes of $\tilde{\theta}(\alpha)$ only decrease to 10^{-7}, and the even modes decrease to 10^{-10}. From the right panel of Figure 5.2, the sequence $\{|c_{2k-1}|\}_{k=1}^{99}$ reaches 10^{-7} when $n = 2k - 1$ is around 79 and will not decrease more for bigger n. The sequence of even modes $\{|c_{2k}|\}_{k=1}^{99}$ achieves 10^{-10} at around $n = 2k = 170$. Compared with the decay of Fourier modes in Figure 3.4 in the zero gravity case where odd modes are directly set to 0 by symmetry, we think the reason of the odd modes not decaying as well as the even modes lies in the numerical treatment of

the infinite tube. On one hand, the singularity of μ_2 after the cotangent transform shown in Figure 3.2 might bring in numerical errors. We suspect that the asymptotic behavior of $\mu_2(\tau)$ as τ approaches 0 and π has some fractional power that is not well-represented by Chebyshev polynomials on $[0, \pi]$. On the other hand, in our methods the infinite tube is always treated as being symmetric about the xy plane, i.e. the large z case is treated in the principal value sense numerically. Each point $p = (1, 0, z) \in S_2$ is treated differently in terms of integration on S_2. In reality, however, due to the infiniteness of S_2, all these p are in some sense no different from each other. We believe that this discrepancy between our numerical representation and reality due to the infinite tube contributes to the problem.

Chapter 5

Time-dependent problem

5.1 Mathematical set up

In this chapter we consider the time dependent problem in which the initial bubble shape $S_1(0)$ and the initial velocity potential $\phi(\zeta(\beta), 0)$ with $\zeta \in S_1(0)$ are given, and the bubble shape $S_1(t)$ evolves with time. Before non-dimensionalization, the steady Bernoulli equation (2.1.4) is changed to the following unsteady one

$$\rho\frac{\partial\tilde{\phi}}{\partial\tilde{t}} + \frac{\rho}{2}|\nabla\tilde{\phi}|^2 + \rho g\tilde{z} + T\tilde{\kappa} = \tilde{C}(t) \quad \text{ on } \tilde{S}_1(t).$$

After non-dimensionalization with transformations $\tilde{t} = \frac{H}{U}t$ (U is the nonzero initial bubble rising velocity), $\phi(x, y, z) = \frac{\tilde{\phi}(\tilde{x},\tilde{y},\tilde{z})}{UH}$, $\tilde{x} = Hx$, $\tilde{y} = Hy$, $\tilde{z} = Hz$, $\tilde{R}_1 = HR_1$, $\tilde{R}_2 = HR_2$ and $T = \tilde{T}/H$, we have the non-dimensionalized unsteady Bernoulli equation

$$\frac{\partial\phi}{\partial t} + \frac{1}{2}|\nabla\phi|^2 + \frac{z}{F^2} + \frac{\kappa}{W} = C(t) \quad \text{ on } S_1(t). \tag{5.1.1}$$

Similar to the steady case, the velocity potential is decomposed as

$$\phi(t) = \phi_1(t) + \phi_2(t) - z, \tag{5.1.2}$$

where $-z$ means that we are still choosing the unit upward rising frame as the model frame. Suppressing the dependence on spatial coordinates (x, y, z) and time coordinate t in the notation, the complete dynamic system we are solving for is

$$\begin{aligned}
&\Delta\phi = 0 \quad \text{in } \mathcal{D},\\
&\phi(p, 0) = \chi_0(p) \quad \text{on the given initial bubble surface } S_1(0),\\
&\frac{\partial\phi}{\partial\mathbf{n}} = 0 \quad \text{on the cylindrical wall } S_2 = \{x^2 + y^2 = 1\},\\
&\frac{\partial\phi}{\partial z} = -1 \quad \text{on } z = \pm\infty,\\
&\frac{\partial\phi}{\partial t} + \frac{1}{2}|\nabla\phi|^2 + \frac{z}{F^2} + \frac{\kappa}{W} = C(t) \quad \text{on } S_1(t),
\end{aligned} \tag{5.1.3}$$

where $\chi_0(p)$ is the given initial velocity potential value at p.

5.2 Representing the solution using single and double layer potentials

One big difference between the unsteady problem and the steady-state problem is the boundary condition on S_1. For the steady problem, it is an exterior Neumann condition, whereas in the unsteady problem it is an exterior Dirichlet condition. Based on this, total velocity potential is still decomposed into three parts: ϕ_1 is generated by a dipole density μ_1 on S_1; ϕ_2 is generated by a charge density μ_2 on S_2; and $-z$ describes the background downward unit speed flow with

$$\begin{aligned}\phi_1(p) &= \frac{1}{4\pi}\int_{S_1}\frac{(p-q)\cdot\mathbf{n}_q}{|p-q|^3}\mu_1(q)\,dA_q,\\ \phi_2(p) &= \frac{1}{4\pi}\int_{S_2}\frac{\mu_2(q)}{|p-q|}\,dA_q,\end{aligned} \tag{5.2.1}$$

where as before, $\mathbf{n}(q)$ is the normal derivative at $q \in S_1$ pointing into fluid domain $\mathcal{D}$.

Using the exterior Dirichlet boundary condition on S_1, (2.3.3b), and interior Neumann boundary condition on S_2, (2.3.2a), we obtain

$$\begin{aligned}\phi(p) &= \frac{\mu_1(p)}{2} + \frac{1}{4\pi}\int_{S_1}\frac{(p-q)\cdot\mathbf{n}_q}{|p-q|^3}\mu_1(q)\,dA_q + \frac{1}{4\pi}\int_{S_2}\frac{\mu_2(q)}{|p-q|}\,dA_q - p_3\\ &= \chi_0(p), \quad p \in S_1, \qquad (5.2.2a)\\ \frac{\partial\phi}{\partial\mathbf{n}_p}(p) &= \frac{\mu_2(p)}{2} + \frac{1}{4\pi}\int_{S_1}\frac{\partial}{\partial\mathbf{n}_p}\Big(\frac{(p-q)\cdot\mathbf{n}_q}{|p-q|^3}\Big)\mu_1(q)\,dA_q + \frac{1}{4\pi}\int_{S_2}\frac{(q-p)\cdot\mathbf{n}_p}{|p-q|^3}\mu_2(q)\,dA_q,\\ &= 0, \quad p \in S_2, \qquad (5.2.2b)\end{aligned}$$

where p_3 is the z coordinate of p. Notice that the first integrand in (5.2.2b) can be simplified as

$$\frac{\partial}{\partial\mathbf{n}_p}\Big(\frac{(p-q)\cdot\mathbf{n}_q}{|p-q|^3}\Big) = -3\frac{\big((p-q)\cdot\mathbf{n}_q\big)\big((p-q)\cdot\mathbf{n}_p\big)}{|p-q|^5} + \frac{\mathbf{n}_p\mathbf{n}_q}{|p-q|^3}$$

due to p never coinciding with q: no singularity is involved.

Now let us work out the detailed expression of (5.2.2) using the HLS framework as in the previous chapter. To make the notation cleaner, we use $F[a,b,c,d,e]$ to denote the following

integral

$$\begin{aligned} F[a,b,c,d,e] :&= \int_0^{2\pi} \frac{a + b\cos\varphi + c\cos^2\varphi}{(d - e\cos\varphi)^{5/2}}\, d\varphi \\ &= \frac{4}{3e^2(d-e)^{3/2}(d+e)^2}\Big((-2cd^3 + bd^2e + 4ade^2 + 6cde^2 + 3be^3)E\Big(-\frac{2e}{d-e}\Big) \\ &\quad + (d+e)(-e(bd+ae) + c(2d^2 - 3e^2))K\Big(-\frac{2e}{d-e}\Big)\Big). \end{aligned} \tag{5.2.3}$$

Notice that when $e = 0$, the above integral can be evaluated analytically to obtain $\frac{\pi(2a+c)}{d^{5/2}}$.

For (5.2.2a), without loss of generality, $p = (\xi(\alpha), 0, \eta(\alpha))$. For the integration over S_1, $q = (\xi(\beta)\cos\varphi, \xi(\beta)\sin\varphi, \eta(\beta))$, and $\mathbf{n}_q = (-\sin\theta(\beta)\cos\varphi, -\sin\theta(\beta)\sin\varphi, \cos\theta(\beta))$. For the integral over S_2, $q = (\cos\varphi, \sin\varphi, y)$. After parametrization, (5.2.2a) can be expressed as

$$\begin{aligned} &2\pi\mu_1(\alpha) + \int_0^{\pi} \mu_1(\beta)\xi(\beta)s_\beta G[a_3, b_3, c_1, d_1]\, d\beta + \int_{-\infty}^{\infty} \mu_2(y)\frac{4K\big(\frac{-2h_1}{g_1-h_1}\big)}{\sqrt{g_1 - h_1}}\, dy \\ &\quad = 4\pi(\eta(\alpha) + \chi_0(\alpha)), \end{aligned} \tag{5.2.4}$$

where

$$a_3 = \xi(\beta)\sin\theta(\beta) + (\eta(\alpha) - \eta(\beta))\cos\theta(\beta), \quad b_3 = \xi(\alpha)\sin\theta(\beta),$$

and c_1, d_1, g_1 and h_1 having the same formula as in (2.6.3).

For (5.2.2b), without loss of generality, $p = (1, 0, z)$ and $\mathbf{n}_p = (1, 0, 0)$. For integration over S_1, $q = (\xi(\beta)\cos\varphi, \xi(\beta)\sin\varphi, \eta(\beta))$ and $\mathbf{n}_q = (-\sin\theta(\beta)\cos\varphi, -\sin\theta(\beta)\sin\varphi, \cos\theta(\beta))$. For the integral over S_2, $q = (\cos\varphi, \sin\varphi, y)$. After parametrization, (5.2.2b) can be expressed as

$$2\pi\mu_2(z) + \int_0^{\pi} \mu_1(\beta)\xi(\beta)s_\beta F[a_4, b_4, c_4, c_2, d_2]\, d\beta + \int_{-\infty}^{\infty} \mu_2(y)G[e_2, f_2, g_2, h_2]\, dy = 0, \tag{5.2.5}$$

with

$$\begin{aligned} a_4 &= -3\big(\xi(\beta)\sin\theta(\beta) + (z - \eta(\beta))\cos\theta(\beta)\big), \\ b_4 &= \sin\theta(\beta)\big(2 + 2\xi^2(\beta) - (z - \eta(\beta))^2\big) + 3\cos\theta(\beta)(z - \eta(\beta))\xi(\beta), \\ c_4 &= -\xi(\beta)\sin\theta(\beta), \end{aligned}$$

and c_2, d_2, e_2, f_2, g_2, h_2 are the same as in (2.6.3).

(5.2.4) and (5.2.5) together solves $\mu_1(\alpha)$ and $\mu_2(z)$, which gives us the velocity potential everywhere by plugging into (5.2.1). Two other elements needed later are the normal velocity $\frac{\partial\phi}{\partial\mathbf{n}}$ and the tangential velocity $\frac{\partial\phi}{\partial s}$ on S_1, and we compute them here for later usage. For any fixed $p = (\xi(\alpha), 0, \eta(\alpha)) \in S_1$, since ϕ_1 is a double layer potential, by (2.3.4) and (2.3.1d), its normal velocity defined in the Cauchy principal value sense is continuous across the surface. Solving for μ_1 and μ_2 through (5.2.2) is a key step in the dynamics computations, thus the

solvability of it should be well studied before proceeding. By the divergence theorem, it is easy to prove that

$$\int_{S_1} \frac{(p-q)\cdot \mathbf{n}_q}{|p-q|^3}\, dA_q = 0, \quad p \in \mathcal{D},$$
$$2\pi + \int_{S_1} \frac{(p-q)\cdot \mathbf{n}_q}{|p-q|^3}\, dA_q = 0, \quad p \in S_1,$$

so $[\mu_1, \mu_2] = \mathbb{R}(1,0)$ is the one dimensional kernel of the system. Thus we omit the zeroth modes in the Fourier expansion of μ_1.

5.3 Hyper-singularity removal and singularity analysis

3D vortex sheets with axial symmetry have been well studied theoretically [6], but we need to compute the singularities using our parametrization in all the integrals to know how to remove them and what numerical schemes to use to integrate them. First, notice that the formula for ϕ_2 is the same as in the steady case, so all the calculations involving it stay the same as before. Evaluations of $\int_{S_2} \frac{\mu_2(q)}{|p-q|}\, dA_q$ and $\int_{S_2} \frac{(q-p)\cdot \mathbf{n}_p}{|p-q|^3}\mu_2(q)\, dA_q$ on S_2 both involve $\log|p-q|$ type of singularity when q approaches the evaluation point p. However, ϕ_1 is different. For any fixed $p = (\xi(\alpha), 0, \eta(\alpha)) \in S_1$, let $q = (\xi(\beta)\cos\varphi, \xi(\beta)\sin\varphi, \eta(\beta))$, we have

$$\phi_1(\alpha) = \frac{1}{4\pi}\int_0^\pi \mu_1(\beta)\xi(\beta)s_\beta G[a_3, b_3, c_1, d_1]\, d\beta, \tag{5.3.1}$$

where $a_3 = \xi(\beta)\sin\theta(\beta) - (\eta(\beta)-\eta(\alpha))\cos\theta(\beta)$ and $b_3 = \xi(\alpha)\sin\theta(\beta)$. By (2.6.2) (2.7.1) and a Taylor expansion around α, we have $b_3c_1 - a_3d_1 = \mathcal{O}(\beta-\alpha)^2$ and the integrand has a $\log|\beta-\alpha|$ type of singularity. Also when $\alpha = 0$ or π, the integrand is smooth as in the steady case. We can use the same method to integrate it numerically as in the steady case.

For normal derivatives of ϕ_1 on S_2, $\int_{S_1} \frac{\partial}{\partial \mathbf{n}_p}\big(\frac{(p-q)\cdot\mathbf{n}_q}{|p-q|^3}\big)\mu_1(q)\, dA_q$ in (5.2.2b) has a smooth integrand due to the evaluation point p and integration point q never coinciding. When they do coincide however, the integrand is hyper-singular. In more detail, let $p = (\xi(\alpha), 0, \eta(\alpha))$ so that

$$\int_{S_1} \frac{\partial}{\partial \mathbf{n}_p}\Big(\frac{(p-q)\cdot \mathbf{n}_q}{|p-q|^3}\Big)\mu_1(q)\, dA_q = \int_0^\pi \mu_1(\beta)\xi(\beta)s_\beta F[a_5, b_5, c_5, c_1, d_1]\, d\beta, \tag{5.3.2}$$

where the formula of c_1, d_1 are as before and

$$\begin{aligned}
a_5 &= 3\xi(\alpha)\xi(\beta)\sin\theta(\alpha)\sin\theta(\beta) + 3(\eta(\beta)-\eta(\alpha))\xi(\beta)\cos\theta(\alpha)\sin\theta(\beta) - \\
&\quad 3\xi(\alpha)(\eta(\beta)-\eta(\alpha))\sin\theta(\alpha)\cos\theta(\beta) + (\xi^2(\alpha)+\xi^2(\beta)-2(\eta(\beta)-\eta(\alpha))^2)\cos\theta(\alpha)\cos\theta(\beta), \\
b_5 &= (-2\xi^2(\alpha) - 2\xi^2(\beta) + (\eta(\alpha)-\eta(\beta))^2)\sin\theta(\alpha)\sin\theta(\beta) + 3\xi(\alpha)(\eta(\alpha)-\eta(\beta))\cos\theta(\alpha) \\
&\quad \sin\theta(\beta) + 3\xi(\beta)(\eta(\beta)-\eta(\alpha))\sin\theta(\alpha)\cos\theta(\beta) - 2\xi(\alpha)\xi(\beta)\cos\theta(\alpha)\cos\theta(\beta), \\
c_5 &= \xi(\alpha)\xi(\beta)\sin\theta(\alpha)\sin\theta(\beta).
\end{aligned}$$

When β approaches α, we have

$$\begin{aligned}-2c_5c_1^3 + b_5c_1^2d_1 + 4a_5c_1d_1^2 + 6c_5c_1d_1^2 + 3b_5d_1^3 &\sim -\xi^6(\alpha)\sigma^2(\beta-\alpha)^2,\\ -d_1(b_5c_1 + a_5d_1) + c_5(2c_1^2 - 3d_1^2) &\sim 12\xi^2(\alpha)\sigma^2(\beta-\alpha)^2.\end{aligned}$$

If $\alpha = 0$ or π, we have

$$F[a_5, b_5, c_5, c_1, d_1] = F[a_5, 0, 0, d, 0] = \frac{2\pi a_4}{c_1^{5/2}} \sim \mathcal{O}(\beta-\alpha)^{-3}.$$

Combined with the only extra term $\xi(\beta) \sim O(\alpha-\beta)$ in the integrand, we get a $1/(\beta-\alpha)^2$ type singularity in the integrand: a hyper-singularity. When $\alpha \in (0,\pi)$, using (2.7.1) (2.7.2), we have a $F[a_5, b_5, c_5, c_1, d_1]$ also containing leading singularity of type $1/(\beta-\alpha)^2$, a hyper-singularity. So unlike before where at $\alpha = 0$ or π the integrand is treated differently, here at any $\alpha \in [0,\pi]$ the integrand formally contains a hyper-singularity. This is why we have to interpret this integral in the principal value sense as below.

Physically, $H[\mu_1](p)$ is the limit of $p_\epsilon = p + \epsilon\mathbf{n}_p$ approaching p from outside the bubble. We introduce a new auxiliary function $\hat{\mu}$ defined both on and off of the surface S_1 and write

$$\begin{aligned}H[\mu_1](p) &= \lim_{\epsilon\to 0^+}\int_S \frac{\partial^2 N(p_\epsilon, q)}{\partial\mathbf{n}_p\partial\mathbf{n}_q}\mu_1(q)\,dA_q\\ &= \lim_{\epsilon\to 0^+}\int_S \frac{\partial^2 N(p_\epsilon, q)}{\partial\mathbf{n}_p\partial\mathbf{n}_q}(\mu_1(q)-\hat{\mu}_1(q))\,dA_q + \lim_{\epsilon\to 0^+}\int_S \frac{\partial^2 N(p_\epsilon, q)}{\partial\mathbf{n}_p\partial\mathbf{n}_q}\hat{\mu}_1(q)\,dA_q \qquad (5.3.3)\\ &= \int_S \frac{\partial^2 N(p, q)}{\partial\mathbf{n}_p\partial\mathbf{n}_q}(\mu_1(q)-\hat{\mu}_1(q))\,dA_q + \lim_{\epsilon\to 0^+}\int_S \frac{\partial^2 N(p_\epsilon, q)}{\partial\mathbf{n}_p\partial\mathbf{n}_q}\hat{\mu}_1(q)\,dA_q,\end{aligned}$$

where we require $\hat{\mu}_1(q)$ to be an axisymmetric harmonic function that is a first order approximation of μ_1 at p, i.e. $|\mu_1(q) - \hat{\mu}_1(q)| \sim \mathcal{O}(q-p)^2$ as q approaches p on S, making the first integrand smooth over S. The limit disappears after swapping with the integral. For the second integral, we apply Green's identity to get

$$\begin{aligned}&\lim_{\epsilon\to 0^+}\int_S \frac{\partial^2 N(p_\epsilon, q)}{\partial\mathbf{n}_p\partial\mathbf{n}_q}\hat{\mu}_1(q)\,dA_q = \lim_{\epsilon\to 0^+}\frac{\partial}{\partial\mathbf{n}_p}\int_S \frac{\partial N(p_\epsilon, q)}{\partial\mathbf{n}_q}\hat{\mu}_1(q)\,dA_q\\ &= \lim_{\epsilon\to 0^+}\frac{\partial}{\partial\mathbf{n}_p}\Big(\int_S N(p_\epsilon, q)\frac{\partial\hat{\mu}_1(q)}{\partial\mathbf{n}_q}\,dA_q - \int_\Omega N(p_\epsilon, q)\Delta\hat{\mu}_1(q)\,dV_q\Big)\\ &= \lim_{\epsilon\to 0^+}\frac{\partial}{\partial\mathbf{n}_p}\int_S N(p_\epsilon, q)\frac{\partial\hat{\mu}_1(q)}{\partial\mathbf{n}_q}\,dA_q\\ &= -\frac{1}{2}\frac{\partial\hat{\mu}_1(p)}{\partial\mathbf{n}_p} + D'\Big[\frac{\partial\hat{\mu}_1(q)}{\partial\mathbf{n}_q}\Big](p),\end{aligned} \qquad (5.3.4)$$

where the last equality uses jump condition (2.3.2b). Combining (5.3.3) and (5.3.4), we get the final formula which we will use when computing normal velocity on S

$$H[\mu_1](p) = \int_S \frac{\partial^2 N(p, q)}{\partial\mathbf{n}_p\partial\mathbf{n}_q}(\mu_1(q)-\hat{\mu}_1(q))\,dA_q - \frac{1}{2}\frac{\partial\hat{\mu}_1(p)}{\partial\mathbf{n}_p} + D'\Big[\frac{\partial\hat{\mu}_1(q)}{\partial\mathbf{n}_q}\Big](p). \qquad (5.3.5)$$

For the tangential velocity on S, due to the double layer potential jump (2.3.3b), applying the tangential derivatives to both sides we have

$$\frac{\partial D^-[\mu](p)}{\partial s} = \frac{1}{2}\frac{\partial \mu(p)}{\partial s} + \frac{\partial D[\mu](p)}{\partial s}. \tag{5.3.6}$$

Similar to the steady case, $\frac{\partial D[\mu](p)}{\partial s}$ has a $1/|\beta - \alpha|$ type singularity in the integrand in HLS framework and is defined in principal value sense by (2.7.4). It can be dealt with similarly to the steady case.

5.4 Evolution under HLS framework

Let us start by describing the motion of the bubble surface using the generic evolution equation [50, 37, 39, 38]. From now on, primes with respect to β, for example, are changed to partial derivatives and denoted using subscript β, and the subscript t means taking derivatives with respect to time t. Due to the problem being axisymmetric around the y axis, for simplicity from now on we restrict ourselves to the xz plane unless stated otherwise. Intersecting S_1 with the xz plane we get the bubble's profile curve $\zeta(\alpha, t) = S_1(t) \cap \{y = 0\}$. For any point $\zeta(\beta, t)$, we use $\mathbf{n}$ and $\mathbf{t}$ to denote the outward normal and unit tangent vectors at the point, respectively. The position of the interface at any moment of time can be determined using the fact that, in the absence of mass transfer through the interface, the interface is convected by the fluid, i.e. the interface normal velocity is equal to the normal component of the fluid velocity. The motion of the profile curve can be described as

$$\zeta_t = (\xi, 0, \eta)_t = u\mathbf{n} + v\mathbf{t}, \tag{5.4.1}$$

where $u = \frac{\partial \phi}{\partial \mathbf{n}}$ is determined by physics, and v instead will be chosen later to enforce a favorable parameterization on the free surface. Since the top and bottom of the bubble are both flat, the following conditions should be guaranteed: $\xi(0, t) = \xi(\pi, t) = 0$, still enforced by (3.2.1) as in the steady case; $\mathbf{n}(0, t) = (0, -1)$, $\mathbf{n}(\pi, t) = (0, -1)$, $\mathbf{t}(0, t) = (1, 0)$ and $\mathbf{t}(\pi, t) = (-1, 0)$. They together induce

$$v(0, t) = \xi_t(0, t) = 0, \quad v(\pi, t) = \xi_t(\pi, t) = 0. \tag{5.4.2}$$

Enforcing the arc-length element s_β being constant when time is fixed as before, at any point $q = (\xi(\beta, t), \eta(\beta, t)) \in \zeta$, the outward normal vector and unit tangential vectors are

$$\mathbf{n} = \frac{(-\eta_\beta, \xi_\beta)}{|(-\eta_\beta, \xi_\beta)|} = (-\sin\theta(\beta), \cos\theta(\beta)), \quad \mathbf{t} = \frac{(\xi_\beta, \eta_\beta)}{|(\xi_\beta, \eta_\beta)|} = (\cos\theta(\beta), \sin\theta(\beta)).$$

Taking time derivatives on both sides of $\theta(\beta, t) = \arctan(\frac{\eta_\beta}{\xi_\beta})$ gives

$$\theta_t = \frac{\xi_\beta \eta_{\beta,t} - \xi_{\beta,t}\eta_\beta}{s_\beta^2} = \frac{(-\eta_\beta, \xi_\beta)}{s_\beta} \cdot \frac{(\xi_{\beta,t}, \eta_{\beta,t})}{s_\beta} = \frac{\mathbf{n} \cdot (u\mathbf{n} + v\mathbf{t})_\beta}{s_\beta} = \frac{u_\beta + v\theta_\beta}{s_\beta}.$$

Since $\tilde{\theta}(\beta,t) = \theta(\beta,t) + \beta$ we also have

$$\tilde{\theta}_t = \theta_t = \frac{u_\beta + v\theta_\beta}{s_\beta} = \frac{u_\beta + v(\tilde{\theta}_\beta - 1)}{s_\beta}. \tag{5.4.3}$$

The evolution of the arc-length element s_β satisfies

$$s_{\beta,t} = \frac{\xi_\beta \xi_{\beta,t} + \eta_\beta \eta_{\beta,t}}{s_\beta} = \frac{(\xi_\beta, \eta_\beta)}{s_\beta} \cdot (\xi_{\beta,t}, \eta_{\beta,t}) = \mathbf{t} \cdot (u\mathbf{n} + v\mathbf{t})_\beta = v_\beta - u\theta_\beta. \tag{5.4.4}$$

The length of the bubble surface profile curve at time t is $\int_0^\pi s_\beta(t)\, d\beta$. Differentiating with respect to time, with boundary condition (5.4.2) we find

$$L_t = \int_0^\pi v_\beta - u\theta_\beta \, d\beta = -\int_0^\pi u\theta_\beta \, d\beta. \tag{5.4.5}$$

To make the arc-length element independent of spatial variable, i.e. $s_\beta(t) = \frac{L(t)}{\pi}$, we also need

$$s_{\beta,t}(t) = \frac{L_t}{\pi} = -\frac{1}{\pi}\int_0^\pi u\theta_\beta \, d\beta \tag{5.4.6}$$

for all t. Combining (5.4.4) and (5.4.5) we get

$$v_\beta = u\theta_\beta - \frac{1}{\pi}\int_0^\pi u\theta_\beta \, d\beta.$$

So after u is determined physically, we solve the above equation for v such that the normalized arc-length parameterization is maintained at all times. Naturally the integration constant is taken such that boundary condition (5.4.2) is satisfied. So we let

$$v(\alpha) = \int_0^\alpha u\theta_\beta \, d\beta - \frac{\alpha}{\pi}\int_0^\pi u\theta_\beta \, d\beta. \tag{5.4.7}$$

The last step is to find the evolution equation for $\chi(\alpha,t) = \phi(\zeta(\alpha,t),t)$, i.e. the total velocity potential restricted to the profile curve of the bubble. Taking time derivatives on both sides, we have

$$\chi_t = \nabla\phi \cdot \zeta_t + \phi_t.$$

Combined with (2.6.7), (5.4.1), the Bernoulli equation can be changed to a equation describing the evolution of χ as

$$\chi_t = u\frac{\partial\phi}{\partial\mathbf{n}} + v\frac{\partial\phi}{\partial s} - \frac{|\nabla\phi|^2}{2} - \frac{\eta(\alpha)}{F^2} - \frac{1}{W}\Big(\frac{\theta_\alpha}{s_\alpha} + \frac{\sin\theta}{\xi(\alpha)}\Big) + C(t), \tag{5.4.8}$$

where $C(t)$ can be taken to be 0 or chosen to project out the spatial mean of the right-hand side, for example. Ways to accurately compute the normal and tangential velocities will be shown in the next section.

5.5 Numerical computation

Normal velocity on S_1

The normal velocity is given by $u = \frac{\partial \phi}{\partial \mathbf{n}} = \frac{\partial \phi_1}{\partial \mathbf{n}} + \frac{\partial \phi_2}{\partial \mathbf{n}} - \cos\theta(\alpha)$ with only $\frac{\partial \phi_1}{\partial \mathbf{n}}$ containing singular integrals. Based on (5.3.5), to evaluate $\frac{\partial \phi_1}{\partial \mathbf{n}}$ for any fixed $p = (\xi(\alpha), 0, \eta(\alpha)) \in S_1$, first we need to find $\hat{\mu}_1(q)$ that satisfies the following four conditions

1. $\hat{\mu}_1(q)$ is harmonic in $\mathbb{R}^3$.
2. $\hat{\mu}_1(p) = \mu_1(\alpha)$.
3. $\nabla\hat{\mu}_1(p) \cdot (\cos\theta(\alpha), 0, \sin\theta(\alpha)) = \mu_1'(\alpha)/\sigma$.
4. $\hat{\mu}_1(q)$ is axisymmetric about z axis.

Spherical harmonics can be applied to find a suitable $\hat{\mu}_1$. In spherical coordinates, we denote $r = \sqrt{x^2+y^2+z^2}$ and let

$$\hat{\mu}_1(x,y,z) = c_0 P_0\Big(\frac{z}{r}\Big) + c_1 r P_1\Big(\frac{z}{r}\Big) + c_2 r^2 P_2\Big(\frac{z}{r}\Big) = c_0 + c_1 z + c_2\Big(z^2 - \frac{x^2+y^2}{2}\Big),$$

where P_k denotes the Legendre polynomial of degree k. This expression guarantees conditions 1 and 4 automatically. We use conditions 2 and 3 to get the following matrix equation

$$A\begin{pmatrix} c_0 \\ c_1 \\ c_2 \end{pmatrix} := \begin{pmatrix} 1 & \eta(\alpha) & \eta^2(\alpha) - \frac{\xi^2(\alpha)}{2} \\ 0 & \sin\theta(\alpha) & 2\eta(\alpha)\sin\theta(\alpha) - \xi(\alpha)\cos\theta(\alpha) \end{pmatrix}\begin{pmatrix} c_0 \\ c_1 \\ c_2 \end{pmatrix} = \begin{pmatrix} \mu_1(\alpha) \\ \frac{\mu_1'(\alpha)}{\sigma} \end{pmatrix}.$$

For $\alpha \in (0,\pi)$, the second row of A cannot be identically 0 due to $\xi(\alpha) > 0$, so A is always of rank 2. To get a continuously varying solution depending on $\alpha \in (0,\pi)$, we choose the smallest set of coefficient (c_0, c_1, c_2) in the l^2 norm, i.e. we aim to minimize $c_0^2 + c_1^2 + c_2^2$. The reason that we choose three basis functions and make it into a quadratic optimization problem instead of directly solving for two coefficients under two basis functions is that we want to find a smooth representation of the coefficients. If we only choose the first two basis functions, for example, $\hat{\mu}$ will not exists at points $\alpha \notin \{0,\pi\}$ satisfying $\theta(\alpha) \in \{0, \pi, -\pi\}$, i.e. points with horizontal tangent planes as illustrated in Figure 5.1. This might happen when the bubble surface evolves. Using three basis functions as above, the horizontal case can be handled well, as will be shown below.

The solution of the above matrix equation can be computed easily using Lagrange multiplier as

$$\begin{aligned} c_0 &= \frac{c(d^2+e^2) - f(ad+be)}{(1+b^2)d^2 - 2abde + (1+a^2)e^2}, \\ c_1 &= \frac{ace^2 + df + b^2df - be(cd+af)}{(1+b^2)d^2 - 2abde + (1+a^2)e^2}, \\ c_2 &= \frac{bd(cd-af) + e(-acd + f + a^2f)}{(1+b^2)d^2 - 2abde + (1+a^2)e^2}, \end{aligned} \tag{5.5.1}$$

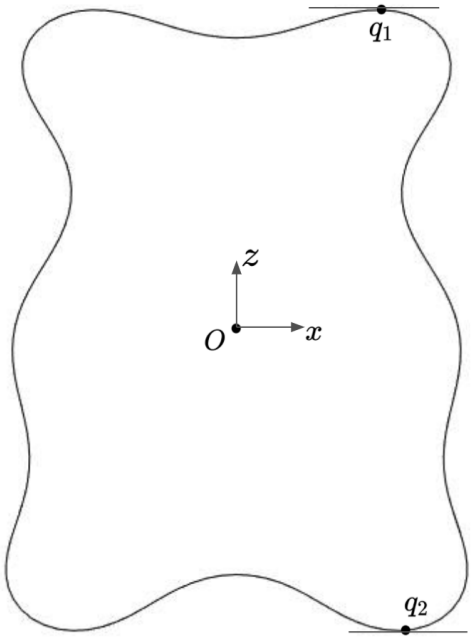

Figure 5.1: Two horizontal tangent points q_1 and q_2 characterized by vanishing tangential angle.

with $a = \eta(\alpha)$, $b = \eta^2(\alpha) - \frac{\xi^2(\alpha)}{2}$, $c = \mu_1(\alpha)$, $d = \sin\theta(\alpha)$, $e = 2\eta(\alpha)\sin\theta(\alpha) - \xi(\alpha)\cos\theta(\alpha)$, and $f = \frac{\mu_1'(\alpha)}{\sigma}$. Here no matter what numbers a, b, d, and e are the denominator is always strictly positive. When $d = 0$, $e \neq 0$ due to the rank of A being 2, the denominator is $(1+a^2)e^2 > 0$. When $e = 0$ and $d \neq 0$, the denominator is $(1+b^2)d^2 > 0$. When $e \neq 0$ and $b \neq 0$, by the Cauchy-Schwarz inequality we have $(1+b^2)d^2 - 2abde + (1+a^2)e^2 > (1+b^2)d^2 - 2|de|\sqrt{1+b^2}\sqrt{1+a^2} + (1+a^2)e^2 = \left(|d|\sqrt{1+b^2} - |e|\sqrt{1+a^2}\right)^2 \geq 0$.

When $\alpha = 0$ or π, however, the second row of A is identically 0 and $\mu_1'(0) = \mu_1'(\pi) = 0$ due to the symmetry about 0 and π. Since $\mu_1(\beta) - \mu_1(0) \sim \mathcal{O}(\beta)^2$ and $\mu_1(\beta) - \mu_1(\pi) \sim \mathcal{O}(\beta - \pi)^2$, we can simply choose $c_0 = \mu_1(\alpha)$ and $c_1 = c_2 = 0$ at $\alpha = 0$ or $\alpha = \pi$.

Now let us parametrize the terms in (5.3.5) to get

$$\int_{S_1} \frac{\partial^2 N(p,q)}{\partial \mathbf{n}_p \partial \mathbf{n}_q} (\mu_1(q) - \hat{\mu}_1(q))\, dA_q$$
$$= \frac{1}{4\pi} \int_0^\pi \Big(\mu_1(\beta) - c_0 - c_1\eta(\beta) - c_2(\eta^2(\beta) - \frac{\xi^2(\beta)}{2})\Big)\xi(\beta) s_\beta F[a_5, b_5, c_5, c_1, d_1]\, d\beta,$$

where the formulae for a_5, b_5 and c_5 are from (5.3.2). We also have

$$\frac{\partial \hat{\mu}_1(p)}{\partial \mathbf{n}_p} = c_2\xi(\alpha)\sin\theta(\alpha) + (c_1 + 2c_2\eta(\alpha))\cos\theta(\alpha)$$

and

$$D'\Big[\frac{\partial\hat{\mu}_1(q)}{\partial\mathbf{n}_q}\Big] = \frac{1}{4\pi}\int_0^\pi \big(c_2\xi(\beta)\sin\theta(\beta) + (c_1+2c_2\eta(\beta))\cos\theta(\beta)\big)\xi(\beta)s'(\beta)G[a_1,b_1,c_1,d_1]\,d\beta,$$

where a_1, b_1, c_1 and d_1 exactly the same as in (2.6.3). $\frac{\partial\phi_2}{\partial\mathbf{n}_p}$ can be calculated as

$$\frac{\partial\phi_2}{\partial\mathbf{n}_p} = \frac{1}{4\pi}\int_{-\infty}^{\infty}\mu_2(y)G[e_1,f_1,g_1,h_1]\,dy,$$

with e_1, f_1, g_1 and h_1 exactly the same as in (2.6.3). The normal velocity from the background flow is

$$-\frac{z}{\partial\mathbf{n}_p} = -\cos\theta(\alpha).$$

Tangential velocity on S_1

Again there are two choices to compute the tangential velocities at the points $\{\xi(\alpha_k)\}_{k=0}^N$. One choice is to take the derivative of the potential on S_1 numerically, using the FFT. This is very convenient since the potential data is given from the previous time step. This could be harder in the steady problem since we would need to first compute the velocity potential on S_1 before applying the FFT. Another method is to first find the analytic expression of tangential velocity and evaluate it at the uniform grid points. The derivation is shown as follows, and it also involves $1/(\beta-\alpha)$ type singularity to be interpreted in the principal value sense as in the steady problem. Unlike in the steady problem, the derivation here is much more complicated, and the cumbersome evaluations could potentially bring in larger round-off errors. Although the second method is listed below for completeness, we choose to use the first (FFT-based) method in the code.

Using (5.3.6) and the HLS parametrization, the tangential velocity at $p=(\xi(\alpha),0,\eta(\alpha))$ is

$$\begin{aligned} v =& \frac{\mu_1'(\alpha)}{2\sigma} + \frac{1}{4\pi}\Big(\int_0^\pi \mu_1(\beta)\xi(\beta)s_\beta F[a_6,b_6,c_6,c_1,d_1]\,d\beta - \int_{-\infty}^{\infty}\mu_2(y)G[e_3,f_3,g_1,h_1]\,d\beta\Big) \\ & - \sin\theta(\alpha), \end{aligned} \tag{5.5.2}$$

where the formula of a_3, b_3, c_1, d_1 are as in (5.2.4), e_3, f_3, g_1 h_1 as in (2.6.5) and

$$\begin{aligned}
a_6 &= (a_3' c_1 - \frac{3}{2} a_3 c_1')/\sigma \\
&= -3\big(\sin\theta(\alpha)(\eta(\alpha)-\eta(\beta)) + \cos\theta(\alpha)\xi(\alpha)\big)\big(\cos\theta(\beta)(\eta(\alpha)-\eta(\beta)) + \sin\theta(\beta)\xi(\beta)\big) \\
&\quad + \cos\theta(\beta)\sin\theta(\alpha)\big((\eta(\alpha)-\eta(\beta))^2 + \xi(\alpha)^2 + \xi(\beta)^2\big), \\
b_6 &= \big(\frac{3}{2}(a_1 d_1' + b_1 c_1') - (a_1' d_1 + b_1' c_1)\big)/\sigma \\
&= -2\cos\theta(\beta)\sin\theta(\alpha)\xi(\alpha)\xi(\beta) - \cos\theta(\alpha)\sin\theta(\beta)\big((\eta(\alpha)-\eta(\beta))^2 + \xi(\alpha)^2 + \xi(\beta)^2\big) \\
&\quad + 3\sin\theta(\beta)\xi(\alpha)(\sin\theta(\alpha)(\eta(\alpha)-\eta(\beta)) + \cos\theta(\alpha)\xi(\alpha)) \\
&\quad + 3\cos\theta(\alpha)\xi(\beta)(\cos\theta(\beta)(\eta(\alpha)-\eta(\beta)) + \sin(\theta(\beta))\xi(\beta)), \\
c_6 &= (b_1' d_1 - \frac{3}{2} b_1 d_1')/\sigma = -\cos\theta(\alpha)\sin\theta(\beta)\xi(\alpha)\xi(\beta),
\end{aligned} \tag{5.5.3}$$

where $'$ means taking derivatives with respect to α. By Taylor expansion, we have the following

$$\begin{aligned}
-2c_6c_1^3 + b_6c_1^2d_1 + 4a_6c_1d_1^2 + 6c_6c_1d_1^2 + 3b_6d_1^3 &\sim 24\xi^5(\alpha)\sin\theta(\alpha)s_\alpha^3(\beta-\alpha)^3, \\
-d_1(b_6c_1 + a_6d_1) + c_6(2c_1^2 - 3d_1^2) &\sim -6\xi^4(\alpha)\sin\theta(2\alpha)s_\alpha^2(\beta-\alpha)^2.
\end{aligned}$$

Again by (2.7.1), with the above computations, similar to the steady case, we have $1/(\beta-\alpha)$ type singularity in

$$\frac{4(-2c_6c_1^3 + b_6c_1^2d_1 + 4a_6c_1d_1^2 + 6c_6c_1d_1^2 + 3b_6d_1^3)}{3d_1^2(c_1-d_1)^{3/2}(c_1+d_1)^2} E\Big(-\frac{2d_1}{c_1-d_1}\Big),$$

and $\log|\beta-\alpha|$ type of singularity in

$$\frac{-d_1(b_6c_1 + a_6d_1) + c_6(2c_1^2 - 3d_1^2)}{3d_1^2(c_1-d_1)^{3/2}(c_1+d_1)} K\Big(-\frac{2d_1}{c_1-d_1}\Big).$$

We can use the singularity subtraction method in (3.1.2) to deal with it.

Numerical procedure

The variables we evolve are the $N-1$ Fourier sine modes of $\tilde{\theta}(\beta,t)$, the arc-length element $s_\beta(t)$, and the $N+1$ evaluations of the velocity potential on the bubble surface, $\{\chi(\alpha_k,t) = \phi(\zeta(\alpha_k,t)),t)\}_{k=0}^N$. At time t_n, the profile curve $\zeta(\alpha,t_n)$ can be reconstructed from the Fourier modes of $\tilde{\theta}(\beta,t_n)$ and $s_\beta(t_n)$. With given $\{\chi(\alpha_k,t_n)\}_{k=0}^N$, we can evaluate (5.2.4) and (5.2.5) after the cotangent transform as in the steady case (3.1) at $\{\alpha_k\}_{k=0}^N$ and $\{\omega\}_{k=1}^M$ respectively. We first solve for μ_1 and μ_2 to determine the normal velocity on S_1. As discussed in Section 4.3, we treat the N cosine Fourier modes of frequency greater than 0 and the $M+1$ Chebyshev modes as the $N+M+1$ variables in total. This gives an $N+M+1$ linear system, which can

be uniquely solved to get the Fourier modes of μ_1 and μ_2. After constructing $\hat{\mu}_1$ from (5.5.1), the normal and the tangential derivatives on profile curve can be computed using formulae from the last two subsections, contributing to the evaluation of the right-hand side of χ_t by (5.4.8). Applying the Fourier transform to (5.4.3) on both sides, we get the evolution equation of the Fourier sine modes of $\tilde{\theta}(t)$. The arc-length element $s_\beta(t)$ can be evolved by (5.4.6) directly.

We use a Runge-Kutta method of order 8 [22] to evolve $\tilde{\theta}$, s_β and χ. In the internal Runge-Kutta stages, $\xi(\pi) = 0$ is enforced by (3.2.1) before computing the profile curve. But the first Fourier modes of $\tilde{\theta}$, i.e. the coefficient before $\sin\beta$, is not updated. However, after a full time step, the curve is projected to the $\xi(\pi) = 0$ case by adding c_0 to the first Fourier modes of $\tilde{\theta}$ where c_0 from (3.2.1) is numerically solved using Newton's method.

5.6 Numerical results

We first study the time evolution of an initial round bubble with the radius 0.9 sitting still with its front stagnation point at the origin. We treat this example as a sanity check of our

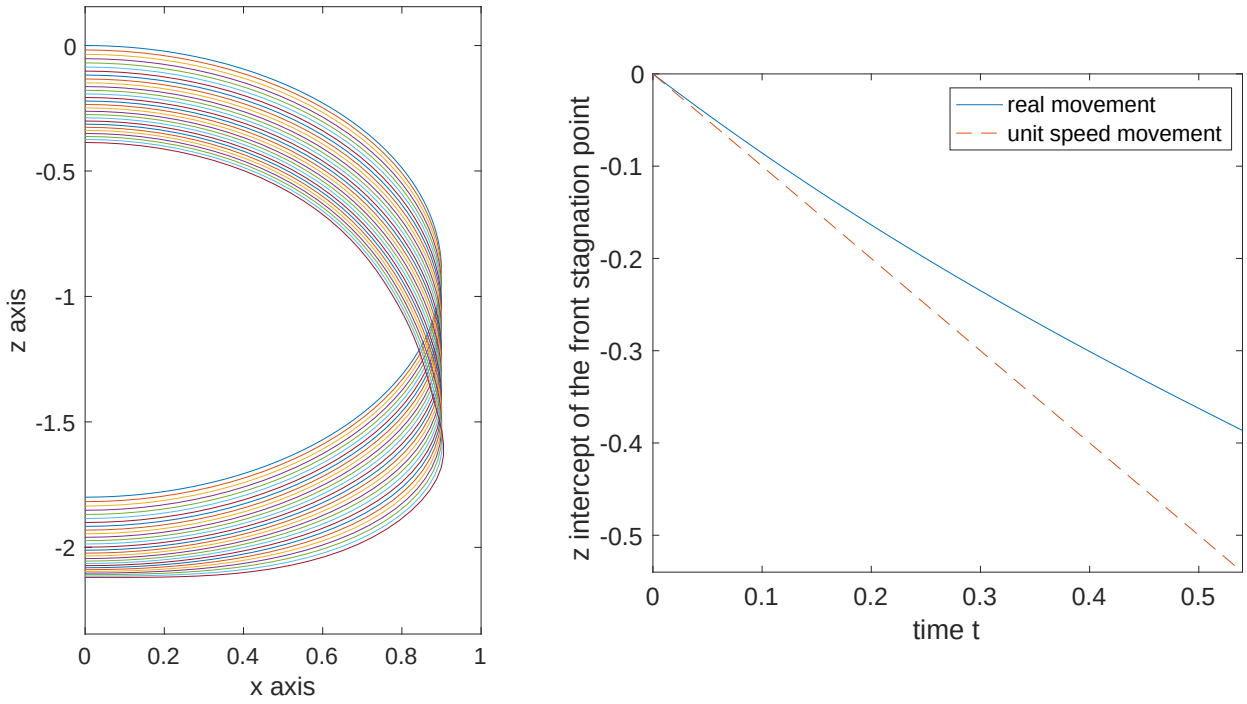

Figure 5.2: Dynamics of the profile curve of a round bubble of radius 0.9 with $F = 1.0$ and $W = 12.3115$ (left) and the displacement of the front stagnation point (right).

inviscid model and the numerical method. The Froude number and Weber number are fixed

to be $F = 1.0$ and $W = 12.3115$. The initial velocity potential on S_1 is set to be $-\cos\theta(\alpha)$. The movement of the profile curve is described in Figure 5.2.

For the left panel, it shows 28 profile curves with $0.02s$ time lapse in between. Since we are thinking of the origin being fixed, and the background flow is flowing down at unit speed, the bubble not only deforms due to the pressure difference at the surface but also moves down at a non-constant speed in the model frame, i.e. frame of reference in which $\phi_z = -1$ at $z = \pm\infty$. In the lab frame, the water is stagnant at $z = \pm\infty$, and the bubble moves up at a non-constant speed. In the right panel, we can see the intercept-time curve of the front stagnation point is slightly concave up, this implies the front stagnation point decelerates as it moves down in the model frame. In the lab frame, the bubble deforms faster at the lower and its front stagnation point accelerates upwards from 0 velocity.

Now we choose solution shapes from the no gravity case to evolve. We fixed $F = 1$, $W = 1.7983$, and the initial potential on the bubble surface is chosen to be the surface potential in the no gravity case. The bubble we choose is a small oblate one with $\sigma(0) = 0.5$. The left panel in 5.3 shows the changes of bubble shapes at every 0.02 second from time 0 to

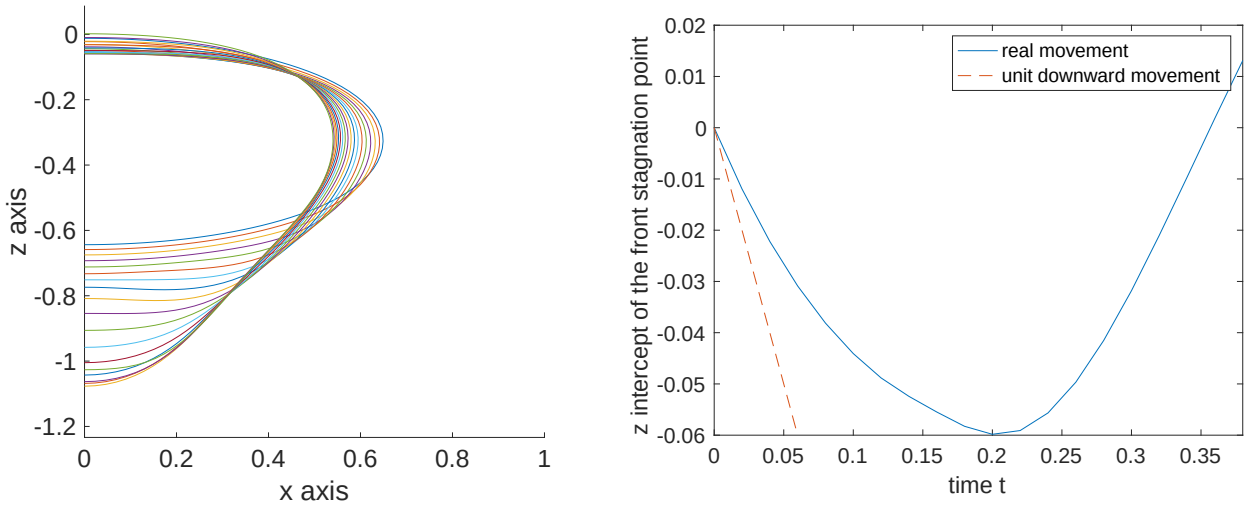

Figure 5.3: Dynamics of the profile curve of steadily rising bubbles with two humps from the no gravity case under the condition $F = 1.0$ and $\sigma = 0.5$ (left) and the displacement of the front stagnation point (right).

time 0.38. we see that the bubbles deform much more in the lower half than the upper half. From the right panel, we see that when gravity is turned on, in the bubble frame it initially drops but decelerates and eventually rises up. In the lab frame, it immediately accelerates upwards, always rising.

Chapter 6

Accurate evaluation of orthogonal polynomials near endpoints of the integration interval

In Chapters 3-5, we proposed a spectral method in which μ_2 is represented by Chebyshev polynomials after the infinite domain is transformed to a finite interval using the cotangent transformation. Most orthogonal polynomials suffer from loss of precision when evaluated near the endpoints of the defining interval, which will bring in numerical errors that might accumulate throughout later computations. In this chapter, we develop alternative recurrence relations for evaluating univariate orthogonal polynomials near an endpoint of the integration interval to improve accuracy when implemented in floating-point arithmetic. These improved recurrence relations also lead to more accurate methods for computing quadrature abscissas and weights.

6.1 Preliminaries

In this section, we review various well-known properties of univariate orthogonal polynomials and quadrature in order to establish notation and summarize the results we need to derive and use the new recurrence relations. For simplicity, we assume the measure with respect to which the polynomials are orthogonal is absolutely continuous with respect to Lebesgue measure. Shifting and/or reflecting the weight function if necessary, we may assume the region where additional accuracy is desired is near the left endpoint of the support of the measure, which is located at $x = 0$. We consider the inner product

$$\langle f, g\rangle = \int_0^{B^2} \overline{f(x)} g(x) w(x)\, dx, \tag{6.1.1}$$

where $w : [0, B^2) \to [0, \infty)$ is integrable and has finite moments of all orders. Here $B > 0$ and $B = \infty$ is allowed. Using B^2 to denote the upper limit of the support of w is convenient in

later sections of this chapter, where its square root appears frequently. The monic orthogonal polynomials $p_k(x)$ can be constructed by the Stieltjes procedure, which leads to the 3-term recurrence

$$\begin{aligned} p_0(x) &= 1, \\ p_1(x) &= x - a_0, \\ p_{k+1}(x) &= (x - a_k)p_k(x) - b_k p_{k-1}(x), \qquad (k \geq 1), \end{aligned} \tag{6.1.2}$$

where

$$a_k = \frac{\langle x p_k, p_k \rangle}{c_k}, \qquad c_k = \langle p_k, p_k \rangle, \qquad b_k = \frac{c_k}{c_{k-1}}. \tag{6.1.3}$$

So far b_k is defined only for $k \geq 1$, but it is also convenient to define $b_0 = c_0$ so that $c_k = \prod_{j=0}^{k} b_j$ for $k \geq 0$. The monic polynomials are often poorly scaled, which can lead to overflow and underflow problems. It is usually preferable to work directly with the normalized polynomials $\varphi_k(x) = p_k(x)/\sqrt{c_k}$, which satisfy $\|\varphi_k\| = 1$ and the 3-term recurrence

$$\begin{aligned} \varphi_0(x) &= 1/\sqrt{c_0}, \\ \sqrt{b_1}\varphi_1(x) &= (x - a_0)\varphi_0(x), \\ \sqrt{b_{k+1}}\varphi_{k+1}(x) &= (x - a_k)\varphi_k(x) - \sqrt{b_k}\varphi_{k-1}(x), \qquad (k \geq 1). \end{aligned} \tag{6.1.4}$$

This recurrence is mathematically equivalent to applying the Gram-Shmidt procedure to orthogonalize the functions $\{1, x, x^2, x^3, \dots\}$. It is often convenient to rescale the weight function $w(x)$ if necessary so that $\varphi_0(x) = b_0 = c_0 = 1$.

Let us fix $n \geq 1$ and define $x_1, \dots, x_n$ to be the zeros of $\varphi_n(x)$. By the separation theorem [14], these zeros are real, distinct, and lie strictly inside $(0, B^2)$. Let $\mathbb{R}_n[x]$ denote the space of polynomials of degree $\leq n$ equipped with the inner product (6.1.1), and let Φ_n map the coefficients $\hat{f} = [\hat{f}_0; \dots; \hat{f}_{n-1}] \in \mathbb{R}^n$ of a polynomial $f(x) = \sum_{k=0}^{n-1} \hat{f}_k \varphi_k(x) \in \mathbb{R}_{n-1}[x]$ to the values of f at the x_j. We also define $X_n = \mathrm{diag}[x_1, \dots, x_n]$ and the nth Jacobi matrix J_n encoding the recurrence (6.1.4). Explicitly, Φ_n and J_n have the form

$$\Phi_n = \begin{pmatrix} \varphi_0(x_1) & \cdots & \varphi_{n-1}(x_1) \\ \varphi_0(x_2) & \cdots & \varphi_{n-1}(x_2) \\ \vdots & & \vdots \\ \varphi_0(x_n) & \cdots & \varphi_{n-1}(x_n) \end{pmatrix}, \quad J_n = \begin{pmatrix} a_0 & \sqrt{b_1} & & & \\ \sqrt{b_1} & a_1 & \sqrt{b_2} & & \\ & \sqrt{b_2} & \ddots & \ddots & \\ & & \ddots & a_{n-2} & \sqrt{b_{n-1}} \\ & & & \sqrt{b_{n-1}} & a_{n-1} \end{pmatrix}. \tag{6.1.5}$$

The recurrence (6.1.4) together with the fact that $\varphi_n(x_j) = 0$ shows that the rows of Φ_n are left eigenvectors of J_n with the abscissas as eigenvalues, i.e.

$$\Phi_n J_n = X_n \Phi_n. \tag{6.1.6}$$

Since J_n is symmetric, the rows of Φ_n are mutually orthogonal. If we were to rescale each row of Φ_n to have unit length, it would be an orthogonal matrix. Without rescaling the

rows, we instead have

$$\Phi_n^T \Omega \Phi_n = I_n, \qquad \Omega = \mathrm{diag}[\omega_1, \ldots, \omega_n], \qquad \omega_j^{-1} = \sum_{k=0}^{n-1} \varphi_k(x_j)^2, \tag{6.1.7}$$

where I_n is the $n \times n$ identity matrix. This equation is equivalent to

$$\sum_{j=1}^{n} \varphi_k(x_j)\varphi_l(x_j)\omega_j = \delta_{kl} = \int_0^{B^2} \varphi_k(x)\varphi_l(x)w(x)\,dx, \qquad (0 \le k, l \le n-1), \tag{6.1.8}$$

which is also true if $k = n$ or $l = n$ (but not both) since the $\varphi_n(x_j) = 0$ for each j in the sum on the left-hand side. This shows that the ω_j are in fact the Gaussian quadrature weights such that

$$\int_0^{B^2} f(x)w(x)\,dx = \sum_{j=1}^{n} f(x_j)\omega_j, \qquad (f \in \mathbb{R}_{2n-1}[x]). \tag{6.1.9}$$

The formula (6.1.7) for ω_j^{-1} is due to Christoffel [14], who derived it in a different way. Golub and Welsch [20] had the idea to solve the eigenvalue problem (6.1.6) numerically to find the abscissas $\{x_j\}$ and weights $\{\omega_j\}$. The eigensolver returns Q_n and $X_n = \mathrm{diag}[x_1, \ldots, x_n]$ such that

$$J_n Q_n = Q_n X_n. \tag{6.1.10}$$

After rescaling some of the rows of Q_n^T by -1 if necessary so that its first column (indexed 0 in our notation) has positive entries, we know from (6.1.7) that $Q_n^T = \Omega^{1/2}\Phi_n$. Moreover, the first column of Φ_n is $\varphi_0(x_j) = 1/\sqrt{c_0}$. Thus, we obtain the Golub-Welsch formula $\omega_j = (Q_n^T)_{j0}^2 c_0$ for $1 \le j \le n$. We will improve on the accuracy of this method in floating-point arithmetic with the new recurrence formulas.

6.2 An associated family of orthogonal polynomials

The key idea that we propose is to change variables (via $x = t^2$) so that evaluation near the endpoint of the original integration interval becomes evaluation of an associated family of orthogonal polynomials near the center of its integration interval. While an extensive literature exists exploring theoretical aspects of this transformation, especially in the context of continued fractions [25], we are not aware of previous work in which its computational benefits in floating-point arithmetic have been studied or noted.

Under the change of variables $x = t^2$, $dx = 2t\,dt$, the inner product becomes

$$\langle \tilde{f}, \tilde{g} \rangle = \int_{-B}^{B} \overline{\tilde{f}(t)}\tilde{g}(t)\tilde{w}(t)\,dt, \qquad \tilde{f}(t) = f(t^2), \quad \tilde{g}(t) = g(t^2), \quad \tilde{w}(t) = |t|w(t^2). \tag{6.2.1}$$

Note that we dropped the factor of 2 in dx and extended the interval to $[-B, B]$ using even symmetry of the integrand. Since the weight function $\tilde{w}(t)$ and interval $[-B, B]$ are

symmetric, the monic orthogonal polynomials $\tilde{p}_n(t)$ with respect to this measure split into even and odd polynomials [14], and the coefficients $\tilde{a}_n$ in the recurrence relation are zero:

$$\tilde{p}_0(t) = 1, \qquad \tilde{p}_1(t) = t, \qquad \tilde{p}_{n+1}(t) = t\tilde{p}_n(t) - \tilde{b}_n\tilde{p}_{n-1}(t), \quad (n \geq 1). \tag{6.2.2}$$

Similarly, since $\tilde{c}_0 = c_0$, we have $\tilde{\varphi}_0(t) = 1/\sqrt{c_0}$, $\tilde{b}_1^{1/2}\tilde{\varphi}_1(t) = t\tilde{\varphi}_0(t)$ and

$$\tilde{b}_{n+1}^{1/2}\tilde{\varphi}_{n+1}(t) = t\tilde{\varphi}_n(t) - \tilde{b}_n^{1/2}\tilde{\varphi}_{n-1}(t), \qquad (n \geq 1). \tag{6.2.3}$$

The even polynomials $\tilde{p}_{2n}(t)$ are monic and orthogonal to all polynomials of lower degree. Since $p_n(t^2)$ also has this property, it must be that

$$\tilde{p}_{2n}(t) = p_n(t^2), \qquad (n \geq 0). \tag{6.2.4}$$

It follows that $\tilde{c}_{2n} = c_n$ and

$$\tilde{\varphi}_{2n}(t) = \varphi_n(t^2), \qquad (n \geq 0). \tag{6.2.5}$$

For later use, note from (6.2.2) and (6.2.4) that

$$t\tilde{p}_{2n+1}(t) = p_{n+1}(t^2) + \tilde{b}_{2n+1}p_n(t^2), \qquad (n \geq 0). \tag{6.2.6}$$

Orthogonal polynomials are generally more oscillatory near the endpoints of the support of the weight function than in the interior.

It is well known that evaluation near the endpoints using (6.1.4) suffers from instability, which is not the case where evaluation happens far from the endpoints. Since our method can change the old evaluation near endpoints to a new evaluation close to 0, which is far from the two endpoints of $[-B, B]$, our idea is that new method using (6.2.3) could gain more accuracy and stability. Additionally, we can form the new Jacobi matrix $\tilde{J}_{2N}$ and diagonalize it to find the new eigenvalues $\{t_j\}_{j=1}^{2N}$, whose squares are the original quadrature abscissas by Theorem 2 below. The new $\{t_j\}_{j=1}^{2N}$, which are the zeros of $\tilde{p}_{2N}(t)$, are more evenly distributed near $t = 0$ than those of $p_N(x)$ near $x = 0$. Thus, we expect more accurate quadrature abscissas using our new method. For quadrature weights, using similar versions of the Christoffel formula [17], i.e.

$$\omega_j = \frac{1}{\sum_{i=0}^{n-1} \tilde{\varphi}_{2i}^2(t_j)}, \tag{6.2.7}$$

we can gain more accuracy by having more accurate evaluation of $\tilde{\varphi}_{2i}$ at more accurate abscissas t_j using our new method. To make all of this happen, it suffices to find $\tilde{b}_n$ using a_n and b_n. We now propose two methods of doing this.

Method using linear term relations

In the first approach, we use the linear terms of $p_n(x)$ and $\tilde{p}_n(t)$. If we give names to the constant and linear terms in $p_n(x)$ and $\tilde{p}_n(t)$, e.g.

$$\begin{aligned} p_n(x) &= x^n + \cdots + d_{n,1}x + d_{n,0}, \qquad (n \geq 0), \\ \tilde{p}_n(t) &= t^n + \cdots + \tilde{d}_{n,1}t + \tilde{d}_{n,0}, \qquad (n \geq 0), \end{aligned} \tag{6.2.8}$$

then (6.2.6) implies that

$$\tilde{b}_{2n+1} = -\frac{d_{n+1,0}}{d_{n,0}}, \qquad (n \geq 0). \tag{6.2.9}$$

Also notice from $p_n(x) = \prod_{i=1}^{n}(x - x_i)$ with $0 < x_1 < \cdots < x_n < B^2$, by direct calculation we have $d_{n,n} = 1$ with

$$d_{n,k} = (-1)^{n-k} \sum_{1 \leq i_1 < \cdots < i_{n-k} \leq n} x_{i_1} \cdots x_{i_{n-k}}, \qquad (0 \leq k \leq n-1). \tag{6.2.10}$$

From this $d_{n,0} = (-1)^n x_1 \cdots x_n \neq 0$, which allows the division in (6.2.9). We also find from (6.2.2) and (6.2.4) that

$$tp_n(t^2) = \tilde{p}_{2n+1}(t) + \tilde{b}_{2n}\tilde{p}_{2n-1}(t), \qquad (n \geq 1). \tag{6.2.11}$$

Matching linear terms, we obtain

$$d_{n,0} = \tilde{d}_{2n+1,1} + \tilde{b}_{2n}\tilde{d}_{2n-1,1}.$$

From (6.2.6), we see that $\tilde{d}_{2n+1,1} = d_{n+1,1} + \tilde{b}_{2n+1}d_{n,1}$ and $\tilde{d}_{2n-1,1} = d_{n,1} + \tilde{b}_{2n-1}d_{n-1,1}$, which gives

$$\tilde{b}_{2n} = \frac{d_{n,0} - \tilde{d}_{2n+1,1}}{\tilde{d}_{2n-1,1}} = \frac{d_{n,0} - d_{n+1,1} - \tilde{b}_{2n+1}d_{n,1}}{d_{n,1} + \tilde{b}_{2n-1}d_{n-1,1}}, \qquad (n \geq 1). \tag{6.2.12}$$

Notice that for odd degree polynomials $\tilde{p}_{2n-1}(t)$, we must have $\tilde{p}_{2n-1}(t) = (t + t_{n-1}) \cdots (t + t_1)t(t - t_1) \cdots (t - t_{n-1}) = t\prod_{i=1}^{n-1}(t^2 - t_i^2)$ with $0 < t_1 < \cdots < t_{n-1} < B$. Expanding the expression we get $\tilde{d}_{2n-1,2n-1} = 1$ and

$$\tilde{d}_{2n-1,2k-1} = (-1)^{n-k} \sum_{1 \leq i_1 < \cdots < i_{n-k} \leq n-1} t_{i_1}^2 \cdots t_{i_{n-k}}^2, \qquad (1 \leq k \leq n-1). \tag{6.2.13}$$

So we have $\tilde{d}_{2n-1,1} = (-1)^{n-1}\prod_{i=1}^{n-1} t_i^2 \neq 0$, thus justifying the division in (6.2.12). Using (6.2.9) and (6.2.12), we can compute $\tilde{b}_1$, $\tilde{b}_3$, $\tilde{b}_2$, $\tilde{b}_5$, $\tilde{b}_4$, $\tilde{b}_7$, $\tilde{b}_6$, etc. to obtain $\{\tilde{b}_k\}_{k=1}^{2N-1}$ for any $N \geq 1$, provided $\{d_{n,0}\}_{n=0}^{N}$ and $\{d_{n,1}\}_{n=0}^{N}$ can be computed. Using the following three-term recurrence relation of monic orthogonal polynomials $p_n(x)$,

$$\begin{aligned} p_0(x) &= 1, \\ p_1(x) &= x - a_0, \\ p_{n+1}(x) &= (x - a_n)p_n(x) - b_n p_{n-1}(x), \end{aligned} \tag{6.2.14}$$

the d's satisfy the recurrence relations

$$\begin{aligned} d_{0,0} &= 1, \qquad d_{1,0} = -a_0, \qquad d_{0,1} = 0, \qquad d_{1,1} = 1, \\ d_{n+1,0} &= -a_n d_{n,0} - b_n d_{n-1,0}, \qquad d_{n+1,1} = d_{n,0} - a_n d_{n,1} - b_n d_{n-1,1}, \quad (n \geq 1), \end{aligned} \tag{6.2.15}$$

so given $\{a_n\}_{n=0}^{N-1}$ and $\{b_n\}_{n=1}^{N-1}$, by first computing $\{d_{n,0}\}_{n=0}^{N}$ and $\{d_{n,1}\}_{n=1}^{N}$ we can easily compute $\{\tilde{b}_n\}_{n=1}^{2N-1}$, as desired.

Notice that $\{\tilde{b}_n\}_{n=1}^{2N-1}$ derived through the above procedure can be directly shown to be positive, without even knowing the hidden relation $\tilde{b}_n = \frac{\tilde{c}_n}{\tilde{c}_{n-1}}$. To prove it, from (6.2.9) and (6.2.12) it suffices to show that $d_{n+1,0}d_{n,0} < 0$ and $|\tilde{d}_{2n+1,1}| > |d_{n,0}| = |\tilde{d}_{2n,0}|$. The first inequality is obvious from (6.2.10). For the second one, using expression (6.2.13) and the interlacing theorem [18], we have $|\tilde{d}_{2n+1,1}| = \prod_{i=1}^{n} t_i^2 > \prod_{i=1}^{n} y_i^2 = |\tilde{d}_{2n,0}|$ where $\{\pm t_i\}_{i=1}^{n} \cup \{0\}$ and $\{\pm y_i\}_{i=1}^{n}$ are the zeros of $\tilde{p}_{2n+1}$ and $\tilde{p}_{2n}$ respectively.

Method using Jacobi matrix relations

The second method we propose to compute $\{\tilde{b}_n\}_{n=1}^{2N-1}$ is based on the following theorem. From now on, we use the following matrix notation

$$\tilde{J} = \begin{pmatrix} 0 & \sqrt{\tilde{b}_1} & & & \\ \sqrt{\tilde{b}_1} & 0 & \sqrt{\tilde{b}_2} & & \\ & \sqrt{\tilde{b}_2} & \ddots & \ddots & \\ & & \ddots & 0 & \sqrt{\tilde{b}_{2N-1}} \\ & & & \sqrt{\tilde{b}_{2N-1}} & 0 \end{pmatrix}, \quad J = \begin{pmatrix} a_0 & \sqrt{b_1} & & & \\ \sqrt{b_1} & a_1 & \sqrt{b_2} & & \\ & \sqrt{b_2} & \ddots & \ddots & \\ & & \ddots & a_{N-2} & \sqrt{b_{N-1}} \\ & & & \sqrt{b_{N-1}} & a_{N-1} \end{pmatrix}.$$

Theorem 1. *The eigenvalues t_n of $\tilde{J}$ are related to the eigenvalues of J via $t_{2n-1} = \sqrt{x_n}$, $t_{2n} = -\sqrt{x_n}$, $1 \leq n \leq N$.*

Proof. Notice first that the eigenvalues $\{t_n\}_{n=1}^{2N}$ of $\tilde{J}$ and the eigenvalues $\{x_n\}_{n=1}^{N}$ of J are the zeros of $\tilde{p}_{2N}(t)$ and $p_N(x)$ respectively, by (6.1.6). Since $\tilde{p}_{2N}(t) = p_N(t^2)$, the square of the zeros of $\tilde{p}_{2N}(t)$ are exactly the zeros of $p_N(x)$. So we can rearrange $\{t_n\}_{n=1}^{2N}$ and $\{x_n\}_{n=1}^{N}$ such that $t_{2n-1} = \sqrt{x_n}$, $t_{2n} = -\sqrt{x_n}$ for $1 \leq n \leq N$, as claimed. □

Theorem 2. *The even rows and columns of $\tilde{J}^2$ give J. The odd rows and columns of $\tilde{J}^2$ yield a matrix with the same eigenvalues as the even rows and columns.*

Proof. By Theorem 1 and Equation (6.1.6), we can write $\tilde{\Phi}\tilde{J} = \tilde{X}\tilde{\Phi}$ explicitly with

$$\tilde{\Phi} = \begin{pmatrix} \tilde{\varphi}_0(\sqrt{x_1}) & \tilde{\varphi}_1(\sqrt{x_1}) & \cdots & \tilde{\varphi}_{2N-1}(\sqrt{x_1}) \\ \tilde{\varphi}_0(-\sqrt{x_1}) & \tilde{\varphi}_1(-\sqrt{x_1}) & \cdots & \tilde{\varphi}_{2N-1}(-\sqrt{x_1}) \\ \vdots & \vdots & & \vdots \\ \tilde{\varphi}_0(-\sqrt{x_N}) & \tilde{\varphi}_1(-\sqrt{x_N}) & \cdots & \tilde{\varphi}_{2N-1}(-\sqrt{x_N}) \end{pmatrix}, \quad \tilde{X} = \begin{pmatrix} \sqrt{x_1} & & & & \\ & -\sqrt{x_1} & & & \\ & & \ddots & & \\ & & & \sqrt{x_n} & \\ & & & & -\sqrt{x_n} \end{pmatrix}.$$

So far it is clear that

$$\tilde{J}^2 = \begin{pmatrix} 0 & \sqrt{\tilde{b}_1} & & & \\ \sqrt{\tilde{b}_1} & 0 & \sqrt{\tilde{b}_2} & & \\ & \sqrt{\tilde{b}_2} & \ddots & \ddots & \\ & & \ddots & 0 & \sqrt{\tilde{b}_{2N-1}} \\ & & & \sqrt{\tilde{b}_{2N-1}} & 0 \end{pmatrix}^2 = \begin{pmatrix} * & 0 & * & & & & \\ 0 & * & 0 & * & & & \\ * & 0 & * & 0 & * & & \\ & \ddots & \ddots & \ddots & \ddots & \ddots & \\ & & * & 0 & * & 0 & * \\ & & & * & 0 & * & 0 \\ & & & & * & 0 & * \end{pmatrix}.$$

Applying $\tilde{J}$ twice to $\tilde{\Phi}$ from the right gives us $\tilde{\Phi}\tilde{J}^2 = \tilde{X}^2\tilde{\Phi}$ by (6.1.6). Since the only possible nonzeros in $\tilde{J}^2$ are in the even submatrix and odd submatrix, we can pick the even rows and columns of $\tilde{J}^2$, $\tilde{\Phi}$ and X to form a new $N \times N$ matrix multiplication $\tilde{\Phi}_e(\tilde{J}^2)_e = (\tilde{X}^2)_e\tilde{\Phi}_e$. Because of $(\tilde{X}^2)_e = X$ and $\tilde{\varphi}_{2n}(\sqrt{x_i}) = \varphi_n(x_i)$, we must have $\tilde{\Phi}_e = \Phi$. Comparing with $J = \Phi^{-1}X\Phi$, we proved $(\tilde{J}^2)_e = J$, i.e. the even rows and columns of $\tilde{J}^2$ give J.
Similarly we can only consider the odd rows and columns of $\tilde{J}^2$, $\tilde{\Phi}$ and X to get equation $\tilde{\Phi}_o(\tilde{J}^2)_o = \tilde{X}_o^2\tilde{\Phi}_o = X\tilde{\Phi}_o$. So the even rows and columns submatrix of $\tilde{J}^2$, the odd rows and columns submatrix of $\tilde{J}^2$, and J all have the same eigenvalues. □

Multiplying out the relation stated in Theorem 2 and comparing entries, we get

$$\begin{aligned} \tilde{b}_{2n+1} &= a_n - \tilde{b}_{2n}, \qquad (n \geq 0,\ \tilde{b}_0 = 0), \\ \tilde{b}_{2n} &= \frac{b_n}{\tilde{b}_{2n-1}}, \qquad (n \geq 1). \end{aligned} \tag{6.2.16}$$

which allows us to find all the $\tilde{b}_n$ iteratively when a_n and b_n are known.

6.3 Connections with continued fractions

A continued fraction [25] is an ordered pair $\langle\langle\{p_n\},\{q_n\}\rangle,\{f_n\}\rangle$ where $\{p_n\} = p_1, p_2, \ldots$ and $\{q_n\} = q_0, q_1, q_2, \ldots$ are complex numbers with all $p_n \neq 0$ and $\{f_n\}$ is a sequence in the extended complex plane defined as follows:

$$f_n = s_0 \circ s_1 \circ \cdots \circ s_n(0), \qquad n = 0, 1, 2, \ldots$$

where $s_0(w) = q_0 + w$ and $s_n(w) = \frac{p_n}{q_n + w}$, $n = 1, 2, 3, \ldots$. For convenience we denote it by $q_0 + \frac{p_1}{q_1+}\frac{p_2}{q_2+}\frac{p_3}{q_3+}\cdots$. Orthogonal polynomials with respect to the weight function $w(x)$ are related to the continued fraction expression of the m-function of $w(x)$ [14, 19, 25]. Directly applying this relation to the original weight function defined on $[0, B^2]$ as before, we have the following theorem.

Theorem 3. *For any $z \in \mathbb{C} - [0, B^2]$ we have*

$$\int_0^{B^2} \frac{w(x)}{z-x}\,dx = \frac{1}{z-a_0-}\frac{b_1}{z-a_1-}\frac{b_2}{z-a_2-}\cdots = \lim_{n\to\infty}\frac{R_n(z)}{S_n(z)}, \tag{6.3.1}$$

where the convergents $\frac{R_n(z)}{S_n(z)}$ satisfy $R_{n+1} = (z-a_n)R_n - b_nR_{n-1}$ with $R_0 = 0$ and $R_1 = 1$, and $S_{n+1} = (z-a_n)S_n - b_nS_{n-1}$ with $S_0 = 1$ and $S_1 = z - a_0$. Truncation of the continued fraction up to the n-th term is related to Stieltjes's result for Gaussian quadrature as follows

$$\sum_{j=1}^{n}\frac{\omega_j}{z-x_j} = \frac{1}{z-a_0-}\frac{b_1}{z-a_1-}\cdots\frac{b_{n-1}}{z-a_{n-1}} = \frac{R_n(z)}{S_n(z)}.$$

Notice that here the denominator $S_n(z)$ is exactly our monic orthogonal polynomial $p_n(z)$. Using (6.3.1), we can give another proof of (6.2.16) as follows.

Denoting $\int_0^{B^2}\frac{w(x)}{z-x}\,dx$ by $F(z)$ and making substitution $x = t^2$ we get

$$\begin{aligned} F(z^2) &= \int_0^{B^2}\frac{w(x)}{z^2-x}\,dx = \int_{-B}^{B}\frac{\tilde{w}(t)}{z^2-t^2}\,dt = \frac{1}{2z}\Big(\int_{-B}^{B}\frac{\tilde{w}(t)}{z-t}\,dt + \int_{-B}^{B}\frac{\tilde{w}(t)}{z+t}\,dt\Big) \\ &= \frac{1}{2z}\Big(\int_{-B}^{B}\frac{\tilde{w}(t)}{z-t}\,dt + \int_{-B}^{B}\frac{\tilde{w}(t)}{z-t}\,dt\Big) = \frac{1}{z}\int_{-B}^{B}\frac{\tilde{w}(t)}{z-t}\,dt = \frac{\tilde{F}(z)}{z}. \end{aligned} \tag{6.3.2}$$

Letting $s_k(w) = \frac{\tilde{b}_k}{z-w}$ and considering only the even part of $\tilde{F}(z)$ (defined in [25]), we let

$$t_k(w) = s_{2k-1}\circ s_{2k}(w) = c_{2k-1} + \frac{c_{2k-1}c_{2k}}{1-c_{2k}-w},$$

where $c_1 = \frac{\tilde{b}_1}{z}$ and $c_k = \frac{\tilde{b}_k}{z^2}$ for $k > 1$. In this way

$$\begin{aligned} s_1\circ s_2\cdots s_{2n}(0) &= t_1\circ t_2\cdots t_n(0) \\ &= c_1 + \frac{c_1c_2}{1-c_2-c_3-}\frac{c_3c_4}{1-c_4-c_5-}\cdots\frac{c_{2n-1}c_{2n}}{1-c_{2n}} \\ &= \frac{1}{z}\Big(\tilde{b}_1 + \frac{\tilde{b}_1\tilde{b}_2}{z^2-\tilde{b}_2-\tilde{b}_3-}\frac{\tilde{b}_3\tilde{b}_4}{z^2-\tilde{b}_4-\tilde{b}_5-}\cdots\frac{\tilde{b}_{2n-1}\tilde{b}_{2n}}{z^2-\tilde{b}_{2n}}\Big). \end{aligned}$$

By Theorem 3, we have the right hand side of (6.3.2) as

$$\begin{aligned}
\frac{\tilde{F}(z)}{z} &= \frac{1}{z}\Big(\frac{1}{z-}\frac{\tilde{b}_1}{z-}\frac{\tilde{b}_2}{z-}\cdots\Big) \\
&= \frac{1}{z}\lim_{n\to\infty}\frac{1}{z - s_1\circ s_2\ldots\circ s_{2n}(0)} = \frac{1}{z}\lim_{n\to\infty}\frac{1}{z - t_1\circ t_2\ldots\circ t_n(0)} \\
&= \frac{1}{z}\frac{1}{z-\frac{1}{z}\big(\tilde{b}_1+\frac{\tilde{b}_1\tilde{b}_2}{z^2-\tilde{b}_2-\tilde{b}_3-}\frac{\tilde{b}_3\tilde{b}_4}{z^2-\tilde{b}_4-\tilde{b}_5-}\cdots\frac{\tilde{b}_{2n-1}\tilde{b}_{2n}}{z^2-\tilde{b}_{2n}-\tilde{b}_{2n+1}-}\cdots\big)} \\
&= \frac{1}{z^2-\tilde{b}_1-\frac{\tilde{b}_1\tilde{b}_2}{z^2-\tilde{b}_2-\tilde{b}_3-}\frac{\tilde{b}_3\tilde{b}_4}{z^2-\tilde{b}_4-\tilde{b}_5-}\cdots\frac{\tilde{b}_{2n-1}\tilde{b}_{2n}}{z^2-\tilde{b}_{2n}-\tilde{b}_{2n+1}-}\cdots} \\
&= \frac{1}{z^2-\tilde{b}_1-}\frac{\tilde{b}_1\tilde{b}_2}{z^2-\tilde{b}_2-\tilde{b}_3-}\frac{\tilde{b}_3\tilde{b}_4}{z^2-\tilde{b}_4-\tilde{b}_5-}\cdots.
\end{aligned}$$

The left hand side of (6.3.2) is

$$F(z^2) = \frac{1}{z^2-a_0-}\frac{b_1}{z^2-a_1-}\frac{b_2}{z^2-a_2-}\cdots.$$

Comparing these two J-fractions (defined in [25]), by uniqueness we must have $\tilde{b}_{2n-1}\tilde{b}_{2n} = b_n$ and $\tilde{b}_{2n}+\tilde{b}_{2n+1} = a_n$, which are (6.2.16).

6.4 Numerical results

To evaluate $\tilde{\varphi}_n$ more accurately through (6.2.3), $\tilde{b}_n$ need to be computed accurately so that the its evaluation error will not accumulate thoroughout the recurrence relation. The good news is that for most 'standard' polynomials such as Jacobi polynomials and Laguerre polynomials, the associated $\tilde{b}_n$ can be computed analytically. For other polynomials whose associated polynomials do not have analytic $\tilde{b}_n$, we can use either method in Section 3 to compute them numerically. To decide which approach is more accurate, we implement both methods to find $\tilde{b}_n$ and compare the error of $\tilde{b}_n$ with the quadruple precision version in floating-point arithmetic. We find that the second method is generally more accurate than the first. This is not surprising considering equations (6.2.9), (6.2.12) and (6.2.15) implemented in the first method carry more computations than that in equation (6.2.16) involved in the second method. More operations of arithmetic might bring in more cancellation of digits, and the round-off error might accumulate in the process. Besides, intermediate values $d_{n,0}$ and $d_{n,1}$ in (6.2.15) for the first method suffer from both underflow and overflow when n is large, which makes it harder to implement. So from now on, we concentrate on using (6.2.16) to find $\tilde{b}_n$ of Jacobi polynomials and generalized Laguerre polynomials to test our new method.

Jacobi polynomial

The classical Jacobi polynomials $P_n^{(\alpha,\beta)}(y)$ are orthonormal polynomials defined on $[-1,1]$ with weights function $w(y) = (1-y)^\alpha(1+y)^\beta$. To put this into our standard form (6.1.1), we can use the change of variables $x = \frac{1+y}{2}$ and $x = \frac{1-y}{2}$ to map $y = -1$ and $y = 1$ to $x = 0$ respectively.

In more detail, the monic Jacobi polynomials $p_n^{(\alpha,\beta)}(y)$ defined on $[-1,1]$ with weight $w(y) = (1-y)^\alpha(1+y)^\beta$ can be related to the shifted monic Jacobi polynomials $\hat{p}_n^{(\alpha,\beta)}(x)$ defined on $[0,1]$ with weight $\hat{w}(x) = (1-x)^\alpha x^\beta$ using the change of variable $x = \frac{y+1}{2}$ in the following way:

$$\begin{aligned} c_n\delta_{mn} &= \int_{-1}^{1} p_n^{(\alpha,\beta)}(y)p_m^{(\alpha,\beta)}(y)w(y)\,dy = 2^{\alpha+\beta+1}\int_0^1 p_n^{(\alpha,\beta)}(2x-1)p_m^{(\alpha,\beta)}(2x-1)\hat{w}(x)\,dx \\ &= 2^{\alpha+\beta+m+n+1}\int_0^1 \hat{p}_n^{(\alpha,\beta)}(x)\hat{p}_m^{(\alpha,\beta)}(x)\hat{w}(x)\,dx = 2^{\alpha+\beta+m+n+1}\hat{c}_n\delta_{mn}, \end{aligned}$$

where we use the relation $p_n^{(\alpha,\beta)}(y) = 2^n\hat{p}_n^{(\alpha,\beta)}(\frac{y+1}{2})$. So we have $\hat{c}_n = \frac{c_n}{2^{\alpha+\beta+2n+1}}$. Similarly one may show that

$$\begin{aligned} \hat{a}_n &= \frac{\langle x\hat{p}_n^{(\alpha,\beta)}, \hat{p}_n^{(\alpha,\beta)}\rangle}{\hat{c}_n} = \frac{1}{2} + \frac{a_n}{2}, \\ \hat{b}_n &= \frac{\langle x\hat{p}_n^{(\alpha,\beta)}, \hat{p}_{n-1}^{(\alpha,\beta)}\rangle}{\hat{c}_{n-1}} = \frac{\langle yp_n^{(\alpha,\beta)}(y), p_{n-1}^{(\alpha,\beta)}(y)\rangle}{2^{\alpha+\beta+1+2n}\hat{c}_{n-1}} = \frac{b_n}{4}, \\ \varphi_n^{(\alpha,\beta)}(y) &= \frac{p_n^{(\alpha,\beta)}(y)}{\sqrt{c_n}} = \frac{2^n\hat{p}_n^{(\alpha,\beta)}(\frac{y+1}{2})}{2^{\frac{\alpha+\beta+2n+1}{2}}\sqrt{\hat{c}_n}} = \frac{\hat{\varphi}_n^{(\alpha,\beta)}(x)}{2^{\frac{\alpha+\beta+1}{2}}}, \end{aligned}$$

where $\varphi_n^{(\alpha,\beta)}(y)$ and $\hat{\varphi}_n^{(\alpha,\beta)}(x)$ are the corresponding orthonormal Jacobi polynomials needed in the recurrence (6.1.4). Using our method from Section 3, we can create new sets of orthonormal polynomials $\tilde{\varphi}_n^{(\alpha,\beta)}(t)$ from $\hat{\varphi}_n^{(\alpha,\beta)}(x)$. Although they are not Jacobi polynomials of any kind, this notation seems natural in the framework of Section 3. To evaluate $\varphi_n^{(\alpha,\beta)}(y)$, we can alternatively evaluate $\tilde{\varphi}_{2n}^{(\alpha,\beta)}(\sqrt{\frac{y+1}{2}})$. From [18], we know

$$\begin{aligned} &a_0 = \frac{\beta-\alpha}{\alpha+\beta+2}, \quad a_n = \frac{\beta^2-\alpha^2}{(2n+\alpha+\beta)(2n+\alpha+\beta+2)}, \quad (n>0), \\ &b_1 = \frac{4(1+\alpha)(1+\beta)}{(2+\alpha+\beta)^2(3+\alpha+\beta)}, \quad b_n = \frac{4n(n+\alpha)(n+\beta)(n+\alpha+\beta)}{(2n+\alpha+\beta)^2(2n+\alpha+\beta+1)(2n+\alpha+\beta-1)}, \quad (n>1), \end{aligned}$$

which we can use easily to calculate the $\hat{a}_n$ and $\hat{b}_n$ first. Applying algorithm (6.2.16) we then can get $\tilde{b}_n$.

We can treat the right endpoint $y = 1$ similarly. letting $x = \frac{1-y}{2}$ we have

$$\begin{aligned} c_n\delta_{mn} &= \int_{-1}^{1} p_n^{(\alpha,\beta)}(y)p_m^{(\alpha,\beta)}(y)w(y)\,dy = 2^{\alpha+\beta+1}\int_0^1 p_n^{(\alpha,\beta)}(1-2x)p_m^{(\alpha,\beta)}(1-2x)\hat{w}(x)\,dx \\ &= (-1)^{m+n}2^{\alpha+\beta+m+n+1}\int_0^1 \hat{p}_n^{(\beta,\alpha)}(x)\hat{p}_m^{(\beta,\alpha)}(x)\hat{w}(x)\,dx = (-1)^{m+n}2^{\alpha+\beta+m+n+1}\hat{c}_n\delta_{mn}, \end{aligned}$$

with $\hat{w}(x) = (1-x)^\beta x^\alpha$, $p_n^{(\alpha,\beta)}(y) = (-2)^n\hat{p}_n^{(\beta,\alpha)}(\frac{1-y}{2})$ and $\hat{c}_n = \frac{c_n}{2^{\alpha+\beta+2n+1}}$. Similarly we can show that

$$\begin{aligned} \hat{a}_n &= \frac{\langle x\hat{p}_n^{(\alpha,\beta)}, \hat{p}_n^{(\alpha,\beta)}\rangle}{\hat{c}_n} = \frac{1}{2} - \frac{a_n}{2}, \\ \hat{b}_n &= \frac{\langle x\hat{p}_n^{(\alpha,\beta)}, \hat{p}_{n-1}^{(\alpha,\beta)}\rangle}{\hat{c}_{n-1}} = \frac{\langle yp_n^{(\alpha,\beta)}(y), p_{n-1}^{(\alpha,\beta)}(y)\rangle}{2^{\alpha+\beta+1+2n}\hat{c}_{n-1}} = \frac{b_n}{4}, \\ \varphi_n^{(\beta,\alpha)}(y) &= \frac{p_n^{(\beta,\alpha)}(y)}{\sqrt{c_n}} = \frac{(-2)^n\hat{p}_n^{(\alpha,\beta)}(\frac{1-y}{2})}{2^{\frac{\alpha+\beta+2n+1}{2}}\sqrt{\hat{c}_n}} = \frac{(-1)^n\hat{\varphi}_n^{(\alpha,\beta)}(x)}{2^{\frac{\alpha+\beta+1}{2}}}. \end{aligned}$$

After applying the transform $x = t^2$ to $\hat{\varphi}_n^{(\alpha,\beta)}(x)$, we get the new set of orthonormal polynomials $\tilde{\varphi}_{2n}^{(\alpha,\beta)}(t)$ on $[0,1]$. Since both ends can be treated similarly, from now on we only deal with evaluation around $y = -1$.

Alternatively, we can derive analytic formulas for the $\tilde{b}_n$ by observing that the associated orthogonal polynomials of Jacobi polynomials are the generalized Gegenbauer polynomials [3]. Their relation can be well seen as $\tilde{w}(t) = |t|\hat{w}(t^2) = |t|^{2\beta+1}(1-t^2)^\alpha$, which is the weight function of the generalized Gegenbauer polynomials. We therefore know that

$$\tilde{b}_{n+1} = \frac{(n+1+\delta_n)(n+1+2\alpha+\delta_n)}{4(n+1+\alpha+\beta)(n+2+\alpha+\beta)} \tag{6.4.1}$$

with $\delta_n = (2\beta+1)\frac{1+(-1)^n}{2}$.

Notice that for evaluation near $y = -1$, the behavior of $P_n^{(\alpha,\beta)}(y)$ is mostly affected by β. Our first test case is when $\alpha = 0.5$ and $\beta = -0.5$, where $P_n^{(0.5,-0.5)}(y)$ is bounded between $[-1,1]$ and behaves like a Chebyshev polynomial near -1. Another test case we choose is $\alpha = 1$, $\beta = 2$, with the magnitude of $P_n^{(1,2)}(-1)$ increasing to infinity as n gets bigger with a well-known estimate [45]

$$\max_{y\in[-1,1]}(1-y)^{\alpha+\frac{1}{2}}(1+y)^{\beta+\frac{1}{2}}\left(P_n^{(\alpha,\beta)}(y)\right)^2 = O(\max\{1,(\alpha^2+\beta^2)^{\frac{1}{2}}\}).$$

The last test case is when $(\alpha,\beta) = (1.7, 2.1)$, which is typical of the most general setting with $\alpha > -1$ and $\beta > -1$. To analyze the relative evaluation error, we introduce the normalized functions

$$q_n^{(\alpha,\beta)}(x) = \frac{P_n^{(\alpha,\beta)}(2x-1)}{P_n^{(\alpha,\beta)}(-1)}, \qquad \tilde{q}_n^{(\alpha,\beta)}(t) = \frac{\tilde{\varphi}_n^{(\alpha,\beta)}(t)}{\tilde{\varphi}_n^{(\alpha,\beta)}(0)}.$$

Since evaluation error $e_n(x) = |q_n(x) - q_n^{\text{quadruple}}(x)|$ is sensitive to the evaluation points x and polynomial degree n, to get a smoother error curve we calculate the average error over a 21-points Chebyshev-Lobbato grid. Specifically, for each $n > 1$, we use the average error $\text{err}_n = \sqrt{\frac{1}{20}\sum_{i=1}^{20} e_n^2(t_i^2)}$ and $\widetilde{\text{err}}_n = \sqrt{\frac{1}{20}\sum_{i=1}^{20} \tilde{e}_{2n}^2(t_i)}$, where $\{t_i\}_{i=0}^{20}$ is the 21-point Chebyshev-Lobatto grid from $t_0 = 0$ to the smallest positive quadrature abscissa t_{20} on $[-1, 1]$ to represent how well an evaluation method near the original endpoint is.

Errors in evaluating $q_n^{(0.5,-0.5)}(x)$, $q_n^{(1,2)}(x)$ and $q_n^{(1.7,2.1)}(x)$ near $x = 0$ with respect to degree n using four different methods are plotted in Figure 6.1. Using (6.1.4) directly, which is the most classic way to evaluate orthogonal polynomials, we get large errors as n increases in all cases as shown in the plots. Implementing all our new methods discussed in Section 3 in double precision, we create the 'improved error', which hits the round-off error threshold in the $(\alpha, \beta) = (0.5, -0.5)$ case, but not in the other two cases. This discrepancy is due to the accuracy of $\tilde{b}_n$. In the $(0.5, -0.5)$ case, the recurrence relation (6.2.16) gives us accurate constant $\tilde{b}_n$ within round-off error due to the a_n and b_n being constant. In the $(\alpha, \beta) = (1, 2)$ case, however, computing $\tilde{b}_n$ from a_n, b_n using (6.2.16) in double precision leads to errors in $\tilde{b}_n$ that affect the accuracy of evaluating $\tilde{q}_n^{(\alpha,\beta)}(t)$. When α and β are non-integers as in the third case, the accumulation error in computing $\tilde{b}_n$ is even worse, making the 'improved method' not much improved. To guarantee the accuracy of $\tilde{b}_n$, besides using the 'analytic formula method' where $\tilde{b}_n$ is computed directly through (6.4.1), we can use 'hybrid quadruple/double' method, i.e. computing $\tilde{b}_n$ through (6.2.16) in quadruple precision with all other computations in double precision. Although computing $\tilde{b}_n$ iteratively in higher precision is more time consuming, this procedure only needs to be executed once and all the following polynomial evaluations can achieve similar accuracy as in the analytical formula method.

From Figure 6.1 we can see generally the hybrid quadruple-double method and the analytic formula method hit the round-off error accuracy as n increases. For generic integer parameters, as in the case when $(\alpha, \beta) = (1, 2)$, both versions give similar error curves. However in the non-integer case, like $\alpha = 1.7$ and $\beta = 2.1$, the hybrid quadruple-double error is slightly bigger than the analytic formula error. In general, however, we are satisfied with the resulting error in both methods. In the last plot of Figure 6.1, we compare the errors of $\tilde{b}_n$ calculated using (6.2.16) in the improved method and those using the analytic formula (6.4.1) in the $(\alpha, \beta) = (1.7, 2.1)$ case. As we can see, the error obtained by the recurrence is much bigger than that by the analytic formula, which validates our reasoning above.

Taking advantage of accurate evaluating near the endpoints using the new methods, we can apply one iteration of the Newton-Raphson method to calculate the abscissas near endpoints more accurately. The intermediate step of evaluating derivatives is done using the recurrence of $\varphi_n'(x)$ by differentiating both sides of (6.1.4). The error in calculating the quadrature abscissas and weights using the classical Golub-Welsch algorithm and our new method are compared in Figure 6.2. Two plots in the first row are for the error of calculating the first 40 quadrature abscissas (zeros of $P_{400}^{(1.7,2.1)}(x)$) closest to -1. As a result, our error is much smaller than that from the Golub-Welsch algorithm. Normalizing the quadrature

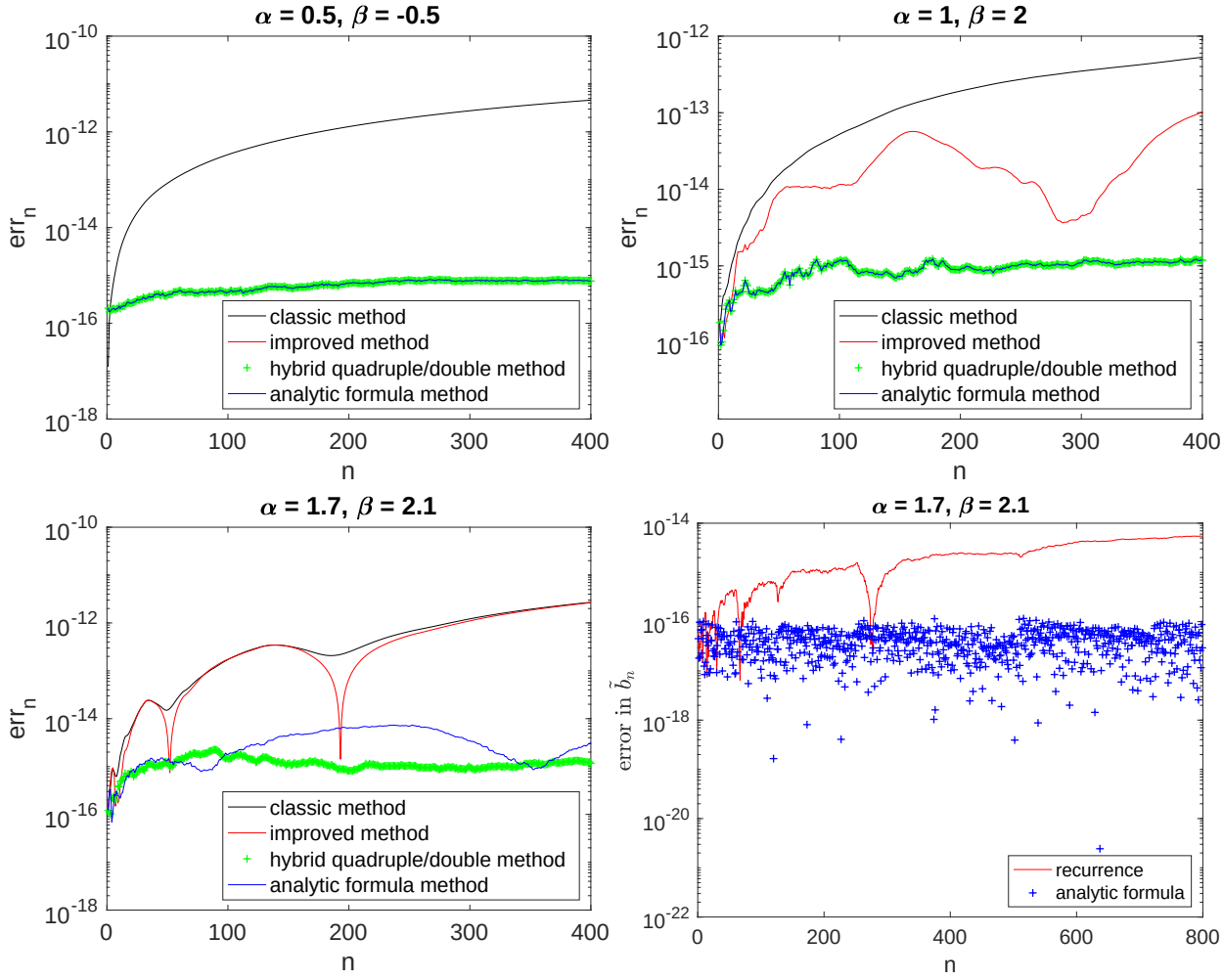

Figure 6.1: Evaluation error of $P_n^{(-0.5,0.5)}$, $P_n^{(1,2)}$ and $P_n^{(1.7,2.1)}$ using the classic, improved, hybrid quadruple/double, and analytic formula methods; and accuracy of $\tilde{b}_n$ used in the improved and analytic formula methods.

weights by multiplying $w^{-\frac{1}{2}}(x)$ to characterize the relative error, the error of the quadrature weights calculated using (6.2.7) at the new abscissas versus those by Golub-Welsch are plotted in the last row of Figure 6.2.

Generalized Laguerre polynomials

Generalized Laguerre polynomials $L_n^{\alpha}(x)$ are orthonormal polynomials defined on $[0, \infty)$ with weight function $w(x) = x^{\alpha}e^{-x}$ $(\alpha > -1)$. Its corresponding associated orthonormal polynomials derived as in Section 3 are denoted as $\tilde{L}_n^{\alpha}(t)$ defined on $(-\infty, \infty)$. So in our

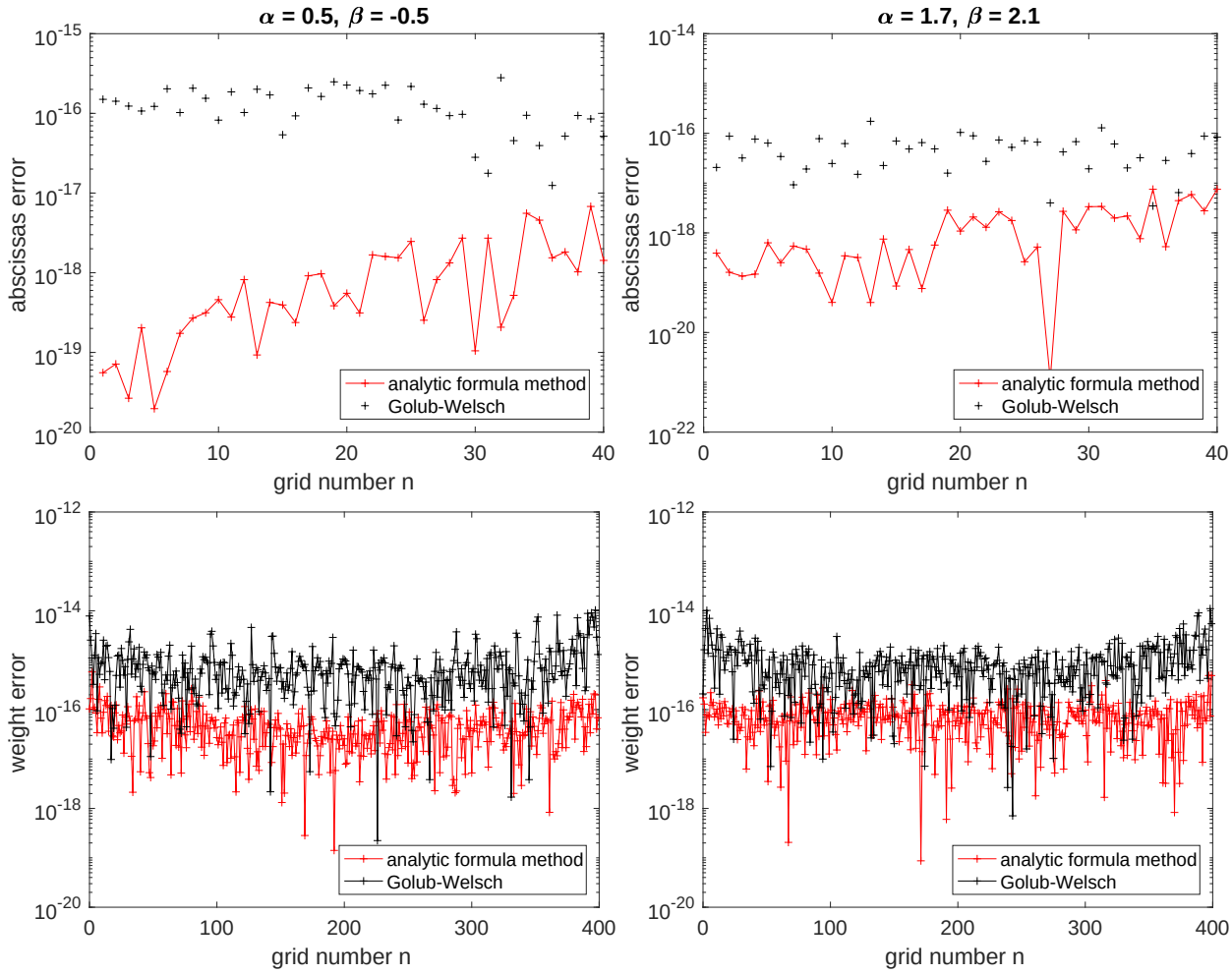

Figure 6.2: Error in calculating quadrature grids and weights of Jacobi type with $\alpha = 0.5$, $\beta = -0.5$ (first column) and $\alpha = 1.7$, $\beta = 2.1$ (second column).

new method, the idea is to evaluate $\tilde{L}^{\alpha}_{2n}(\sqrt{x})$ instead of $L^{\alpha}_{n}(x)$ whenever x is close to 0. Notice that the new associated weight function $\tilde{w}(t) = |t|w(t^2) = |t|^{2\alpha+1}e^{-t^2}$ defines the so-called generalized Hermite polynomial. Similar to Jacobi polynomials, we can either get the analytic formula of $\tilde{b}_{2n} = n$ [18], or calculate $\tilde{b}_n$ numerically using (6.2.16), which might lead to cancellation of error in some cases. Notice that $L^{\alpha}_{n}(x)$ goes to infinity as x increases, so to avoid overflow, we rescale the the output evaluation to be $L^{\alpha}_{n}(x)w^{\frac{1}{2}}(x)$. Due to the fast decaying property of $w(x)$, we also scale the quadrature weights by dividing it by $w(x)$ to avoid underflow. In this way, both polynomial evaluation and quadrature weight output are of order 1 and they together still satisfy the quadrature formula. Similar to Jacobi polynomials, we plot the average evaluation error of the generalized Laguerre polynomial over a 21-point Chebyshev-Lobatto grid distributed from 0 to the smallest positive quadrature

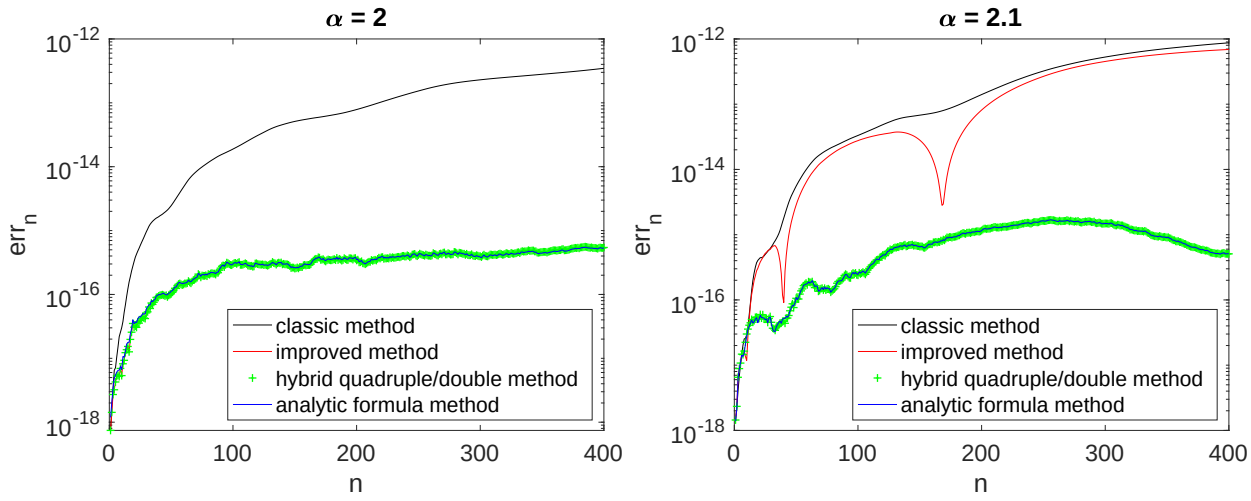

Figure 6.3: Evaluation error of $L_n^2(x)$ and $L_n^{2.1}(x)$ using the classic, improved, hybrid and analytic formula methods.

abscissa on $(-\infty, \infty)$, where evaluation error at each point is obtained by comparing with the quadruple precision version. The relation between 'classic error', 'improved error', 'analytic formula error' and 'hybrid quadruple/double error' and n are plotted in Figure 6.3 for $\alpha = 2$ and $\alpha = 2.1$. As in the Jacobi case, there is a discrepancy between the accuracy of the 'improved method' in both cases due to computing $\tilde{b}_n$ using (6.2.16) in double precision. When $\alpha = 2$, it is more or less the same as the best two methods, achieving round-off error accuracy. Whereas in the $\alpha = 2.1$ case, its error is similar to the classic method. This is again due to the nice property when $\alpha = 2$ that all the a_n, b_n and $\tilde{b}_n$ turn out to be integers and no large error is accumulated in the recurrence relation. In general, for all $\alpha \in \mathbb{N}$, the 'improved method' works well. For generic $\alpha \in \mathbb{R}$, however, we need the other two methods to achieve round-off error accuracy.

Figure 6.4 shows the error in finding quadrature abscissas and weights in the $\alpha = 2.1$ case, which serves as a generic case with $-1 < \alpha \in \mathbb{R}$. Unlike Jacobi polynomials, we cannot apply our new method near the right endpoint since it is ∞.

General orthogonal polynomials

When evaluating general orthogonal polynomials near endpoints, if we can derive analytic formulas of the associated $\tilde{b}_n$ directly, the 'analytic formula method' is the best choice, which has the same time complexity $\mathcal{O}(n)$ as the classic method when evaluating an n-th degree orthogonal polynomial at a certain point, yet achieves the round-off error accuracy. If we cannot find the analytic formula of $\tilde{b}_n$, but the analytic formula of b_n is known, we should choose the hybrid quadruple/double method. Although the overall computation increases compared to the classic method due to the quadruple precision calculation of a_n, b_n and $\tilde{b}_n$,

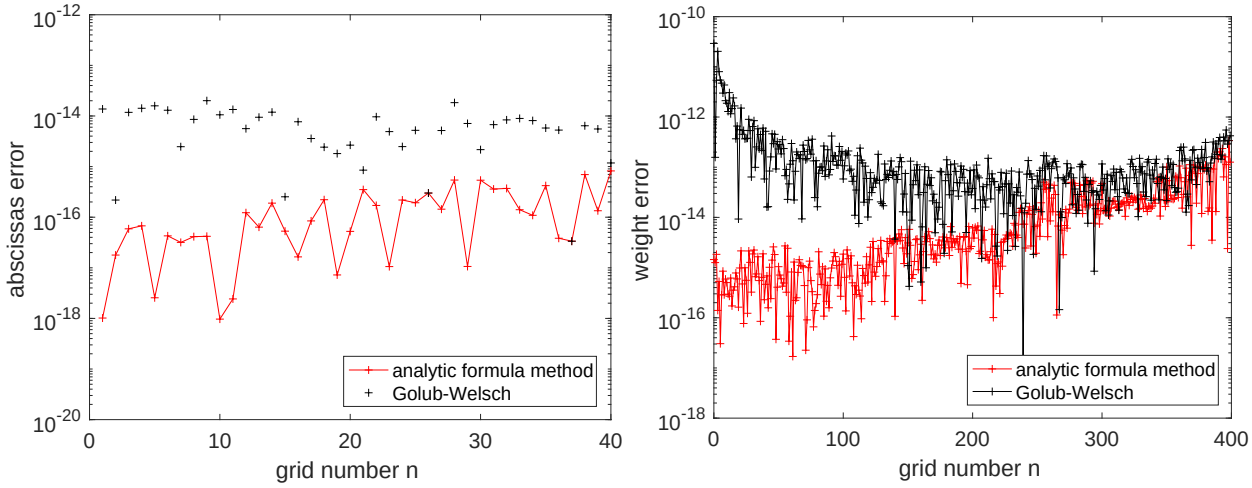

Figure 6.4: Error of quadrature abscissas and weights for the generalized Laguerre case $\alpha = 2.1$ using classic and analytic formula methods.

these only have to be computed once and subsequent evaluations near the endpoints can be done in double precision with improved accuracy.

What if no analytic formula can be found for either b_n or $\tilde{b}_n$? Our method still works well. Let us take Maxwell polynomials (half-line Hermite polynomials) as an example. We will use 'Maxwell polynomial' to denote the non-classical family of real-valued orthonormal polynomials $\varphi_n(x)$ with weight $w(x) = x^2 e^{-x^2}$ over the positive real line. The recurrence coefficients a_n and b_n satisfy

$$b_n + b_{n-1} + a_{n-1}^2 = \frac{2n+2}{2}, \quad a_n a_{n-1} b_n = \left(\frac{n+1}{2} - b_n\right)^2 - \frac{1}{4}, \tag{6.4.2}$$

and can be numerically computed using the method proposed in [2].

For the associated polynomials which are orthonormal polynomials with respect to the weight function $\tilde{w}(t) = |t|^5 e^{-t^4}$, a special case of Freud weights $w_\rho(t) = |t|^\rho e^{-|t|^m}$ where $\rho > -1$ and $m > 0$, $\tilde{b}_n$ in our case satisfy $4\tilde{b}_n^2(\tilde{b}_{n+1}^2 + \tilde{b}_n^2 + \tilde{b}_{n-1}^2) = n + 2(1 - (-1)^n)$, with $\tilde{b}_0 = 0$ and $\tilde{b}_1 = \sqrt{\frac{\Gamma(2)}{\Gamma(1.5)}}$. Making the substitution $x_n = 2\tilde{b}_n^2$, we get the *discrete Painlevé equation* d-P_1

$$x_n(x_{n+1} + x_n + x_{n-1}) = n + 2\big(1 - (-1)^n\big), \tag{6.4.3}$$

which is a non-linear recurrence relation that has a unique non-negative solution. We implement the 'boundary-value approach' proposed in [30] to get numerically accurate $\tilde{b}_n$.

Now using the a_n, b_n and $\tilde{b}_n$ calculated as above, we get the following error plot of Maxwell polynomial evaluation in Figure 6.5. Notice here we change names of 'analytic formula method' to 'direct calculation method' as we do not have analytic expression of $\tilde{b}_n$. In direct calculation method, we use (6.4.3) to obtain $\tilde{b}_n$ directly. Whereas in the 'hybrid

quadruple/double method', we solve for a_n and b_n through (6.4.2) and compute $\tilde{b}_n$ through (6.2.16) in quadruple precision with all the subsequent calculations in double precision.

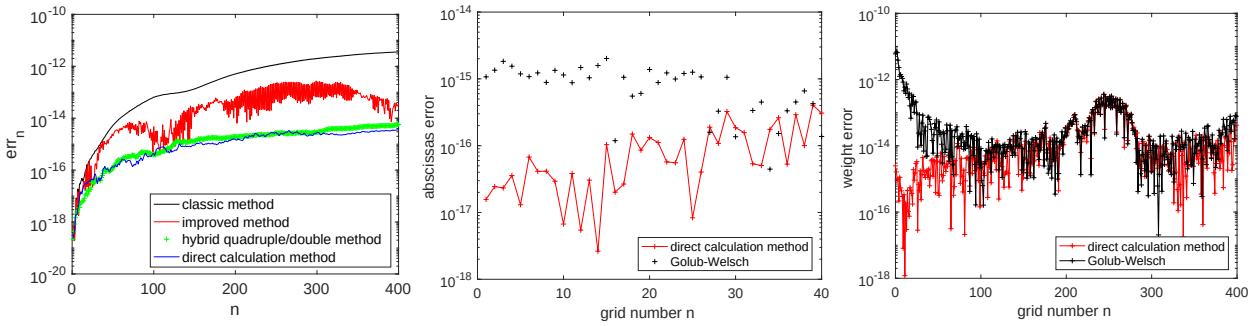

Figure 6.5: Evaluation error of Maxwell polynomial $\varphi_n(x)$ using 4 methods(left). Quadrature abscissas(middle) and weights(right) error using 'direct calculation method' and 'Golub-Welsch'.

Quadrature abscissas near endpoints can be calculated by solving for eigenvalues of $\tilde{J}_n$ as before, followed by one step of Newton-Raphson. Again, the weights can be calculated using (6.2.7). We find that they are more accurate near the left endpoint 0 than by Golub-Welsch.

6.5 Amplification factor analysis

To see why the new algorithm works better, let us first rewrite (6.1.4) in matrix form as

$$\phi_n = \begin{pmatrix} \frac{x-a_n}{\sqrt{b_{n-1}}} & -\sqrt{\frac{b_n}{b_{n+1}}} \\ 1 & 0 \end{pmatrix} \phi_{n-1} = B_{n,n-1}\phi_{n-1} \quad \text{where} \quad \phi_n = \begin{pmatrix} \varphi_{n+1} \\ \varphi_n \end{pmatrix}. \tag{6.5.1}$$

Using this notation, we also have

$$\phi_n =: B_{n,m}\phi_m, \tag{6.5.2}$$

with $B_{n,m} = B_{n,n-1}B_{n-1,n-2}\cdots B_{m+1,m}$. In numerical calculations, however, numerical error proportional to the input is brought in on each step of matrix multiplication and is amplified through (6.5.2). Since the numerical error in forming the matrix $B_{n,m}$ can be moved to the input vector ϕ_m, without loss of generality, we always consider the matrix multiplication to be exact with an input error proportional to ϕ_m. We now present an error analysis. Let ϵ denote a 2 by 2 matrix with $||\epsilon||_2 = \mathcal{O}(\varepsilon)$ where ε is the machine round-off error for single, double, quadruple or arbitrary precision floating-point arithmetic is used. We have the norm of the numerical error after (6.5.2) bounded by $||B_{n,m-1}|| \cdot ||\phi_{m-1}||\varepsilon$, with the relative error bounded by $\frac{||B_{n,m-1}||\cdot||\phi_{m-1}||\varepsilon}{||\phi_n||}$. We define the amplification factor A_n of ϕ_n to be

$$A_n = \frac{\sum_{0\le m<n} ||B_{n,m}|| \cdot ||\phi_m||}{||\phi_n||}, \tag{6.5.3}$$

which provides an upper bound on the amplification of the relative error compared to machine error ε for errors committed at each step of the recurrence. Similarly, applying the formula to our new algorithm we have

$$\tilde{A}_{2n} = \frac{\sum_{0 \le m < 2n} ||\tilde{B}_{2n,m}|| \cdot ||\tilde{\phi}_m||}{||\tilde{\phi}_{2n}||}.$$

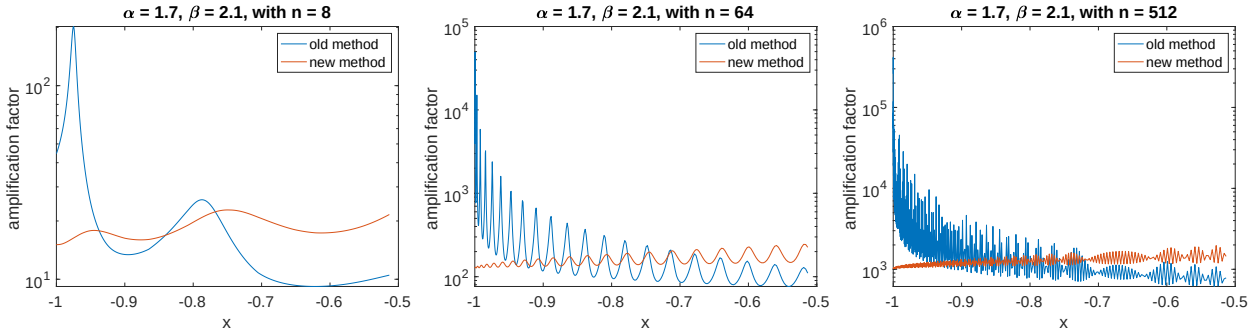

Figure 6.6: Amplification factors of Jacobi polynomial in the $(\alpha, \beta) = (1.7, 2.1)$ case with $n = 8$, 64, 512 and $y \in [-1, -0.5]$ obtained from the old and the new methods.

Both amplification factors for different n and at different evaluation points x are presented in Figure 6.6 for Jacobi polynomials with the most general parameters $(\alpha, \beta) = (1.7, 2.1)$. We find that when $n \ge 8$, $\tilde{A}_{2n}(y) < A_n(y)$ for $y \le -0.95$. Surprisingly, this threshold $y = -0.9$ also applies to Jacobi polynomials with general (α, β) pairs. This result validates our numerical results in the previous section and also gives us a threshold of when to use the new recurrence relations versus the original ones. To get more accurate evaluation of Jacobi polynomials at $y \in [-1, 1]$, we can first compare y with -0.95 (even -0.9 when n is large as seen from the Figure 6.6). If x is smaller, we use our new algorithm to evaluate. Otherwise we use the classic method. We have turned this idea into a package.

Chapter 7

Conclusion and future work

In the first part of the dissertation (Chapters 2-5), we model the 3D axisymmetric rising-bubble problem in the high Reynolds number regime. The novelty of our work lies in the following aspects: Potential theory in 3D is used to present the velocity potential and methods are devised to numerically integrate singular integrals with spectral accuracy; the HLS framework is applied to get uniform grid spacing on the bubble surface with respect to arc-length and a projection is devised to guarantee $\xi(\pi) = 0$ in both the steady and unsteady problem; steady bubble shapes characterized by the different number of humps are found. The importance of boundary layer effects is implied from the comparison between the inviscid model (using potential flow) and the viscous model (using viscous potential flow).

Our original motivation for modeling the rising bubble problem is to get a more accurate representation of the bubble shapes, so we use spectral methods to solve the discretized systems numerically throughout our work, but there are several places that we would like to refine more if we had more time. One future work is to study the compactness of layer potential operators on infinite cylinders. Our numerical method suggests that the discretized system is always solvable in our problem, but the compactness of D' has not been shown. Besides, the way we integrate on the infinite domain using the cotangent transform might bring in singularities at the finite endpoints, which we have not analyzed. Our inability to fully achieve round-off error accuracy might be related to not representing μ_2 at the endpoints well enough.

In the second part of the dissertation (Chapter 6), we introduce a new way to evaluate orthogonal polynomials more accurately near the endpoints of the integration interval by evaluating at corresponding points the newly created associated orthogonal polynomials. The connection between the (associated) orthogonal polynomials and the (even part of) continued fractions brings some insight into the transformation $x = t^2$. For evaluation close to the endpoint, our new methods (both analytic formula method and hybrid method) can achieve 3 more digits of accuracy than the classic recurrence method for general orthogonal polynomials when the degree is around 400. Furthermore, the higher the polynomial degree is, the more the new methods outperform the classic one. Based on the accurate evaluation, more accurate quadrature abscissas near endpoints and more accurate quadrature weights

are obtained compared to those by Golub-Welsch.

Besides the new method stated in Chapter 6, we have been exploring another new set of orthogonal polynomials associated with the odd part of continued fractions. They relate to the original monic orthogonal polynomials via $\tilde{p}_{2n+1}(t) = tp_n(t^2)$. The new data $\tilde{b}_n$ can be computed from a new recurrence relation similar to (6.2.16). However, so far this approach does not give better results than our new methods presented in Chapter 6. Although other transformations such as $x = t^4$ are not as natural as $x = t^2$, for future work it would be interesting to explore whether they will bring some new aspect to the problem.

Bibliography

[1] F. Audrey, E. Patricia, and R. Véronique. "Oscillatory motion and wake of a bubble rising in a thin-gap cell". In: *Journal of Fluid Mechanics* 778 (2015), pp. 60–88.

[2] J. S. Ball. "Half-range generalized Hermite polynomials and the related Gaussian quadrature". In: *SIAM Journal on Numerical Analysis* 40.6 (2002), pp. 2311–2317.

[3] S. Belmehdi. "Generalized Gegenbauer orthogonal polynomials". In: *Journal of Computational and Applied Mathematics* 133 (2001), pp. 195–205.

[4] D. Bhaga and M. E. Weber. "Bubbles in viscous liquids: shapes, wakes and velocities". In: *Journal of Fluid Mechanics* 105 (1980), pp. 61–85.

[5] J. Burke and E. Knobloch. "Snakes and ladders: localized states in the Swift-Hohenberg equation". In: *Physics Letter A* 360 (2007), pp. 681–688.

[6] R. E. Caflisch and X. F. Li. "Lagrangian theory for 3D vortex sheets with axial or helical symmetry". In: *Transport Theory and Statistical Physics* 21.4-6 (1992), pp. 559–578.

[7] R. Clift, J. R. Grace, and M. E. Weber. *Bubbles, Drops, and Particles*. New York, San Francisco, London: Academic Press, 1978.

[8] D. Colton and R. Kress. *Integral Equation Methods in Scattering Theory*. Philadelphia: Society for Industrial and Applied Mathematics, 1992.

[9] R. M. Davies and G. I. Taylor. "The mechanics of large bubbles rising through extended liquids and through liquids in tubes". In: *Proceedings of the Royal Society of London. Series A. Mathematical and Physical Sciences* 200.1062 (1950), pp. 375–390.

[10] C. H. Delaunay. "Sur la surface de révolution dont la courbure moyenne est constante". In: *Journal de Mathématiques Pures et Appliquées* 6 (1841), pp. 309–314.

[11] A. Doak and J. M. Vanden-Broeck. "Solution selection of axisymmetric Taylor bubbles". In: *Journal of Fluid Mechanics* 843 (2018), pp. 518–535.

[12] G. B. Folland. *Introduction to Partial Differential Equations*. Princeton, New Jersey: Princeton University Press, 1995.

[13] T. Fukushima. "Precise and fast computation of the general complete elliptic integral of the second kind". In: *Mathematics of Computation* 80.275 (2011), pp. 1725–1743.

[14] G. Szegö. *Orthogonal Polynomials*. New York City: American Mathematical Society, 1939.

[15] A. Gajewski. "Liquid-gas interface under hydrostatic pressure". In: *Advances in Fluid Mechanics* 9 (2012), pp. 251–261.

[16] P. R. Garabedian and M. Schiffer. "On existence theorems of potential theory and conformal mapping". In: *Annals of Mathematics* 52.1 (1950), pp. 164–187.

[17] W. Gautschi. "Construction of Gauss-Christoffel quadrature formulas". In: *Mathematics of Computation* 22.102 (1968), pp. 251–270.

[18] W. Gautschi. *Orthogonal Polynomials: Computation and Approximation*. Oxford: Oxford University Press, 2004.

[19] F. Gesztesy and B. Simon. "m-Functions and inverse spectral analysis for finite and semi-finite Jacobi matrices". In: *Journal d'Analyse Mathématique* 73.1 (1997), pp. 267–297.

[20] G. H. Golub and J. H. Welsch. "Calculation of Gauss quadrature rules". In: *Mathematics of Computation* 23.106 (1969), pp. 221–230.

[21] W. Hackbusch. *Integral Equations: Theory and Numerical Treatment*. Basel, Boston, Berlin: Birkhäuser, 1995.

[22] E. Hairer, S. Nørsett, and G. Wanner. *Solving Ordinary Differential Equations I*. Berlin Heidelberg: Springer, 1993.

[23] T. Y. Hou, J. S. Lowengrub, and M. J. Shelley. "The long-time motion of vortex sheets with surface tension". In: *Physics of Fluids* 9.7 (1997), pp. 1933–1954.

[24] J. Hua and J. Lou. "Numerical simulation of bubble rising in viscous liquid". In: *Journal of Computational Physics* 222.2 (2007), pp. 769–795.

[25] W. B. Jones and W. J. Thron. *Continued Fractions: Analytic Theory and Applications*. Cambridge: Cambridge University Press, 1984.

[26] D. D. Joseph. "Potential flow of viscous fluids: historical notes". In: *International Journal of Multiphase Flow* 32.3 (2006), pp. 285–310.

[27] N. D. Katopodes. *Free-Surface Flow: Environmental Fluid Mechanics*. Kidlington, Oxford: Butterworth-Heinemann, 2019.

[28] O. D. Kellogg. *Foundations of Potential Theory*. Berlin, Heidelberg, New York: Springer, 1967.

[29] R. Kress. *Linear Integral Equations*. New York: Springer, 1989.

[30] J. S. Lew and D. A. Quarles Jr. "Nonnegative solutions of a nonlinear recurrence". In: *Journal of Approximation Theory* 38.4 (1983), pp. 357–379.

[31] J. Ma, V. Rokhlin, and S. Wandzura. "Generalized Gaussian quadrature rules for systems of arbitrary functions". In: *SIAM Journal on Numerical Analysis* 33.3 (1996), pp. 971–996.

[32] C. Málaga and J. M. Rallison. "A rising bubble in a polymer solution". In: *Journal of Non-Newtonian Fluid Mechanics.* 141.1 (2007), pp. 59–78.

[33] S. Middleman. *Modeling Axisymmetric Flows, Dynamics of Films, Jets and Drops.* New York: Academic Press, 1995.

[34] M. Miksis, J. M. Vanden-Broeck, and J. B. Keller. "Axisymmetric bubble or drop in a uniform flow". In: *Journal of Fluid Mechanics* 108 (1981), pp. 89–100.

[35] M. Miksis, J. M. Vanden-Broeck, and J. B. Keller. "Rising bubbles". In: *Journal of Fluid Mechanics* 123 (1982), pp. 31–41.

[36] D. W. Moore. "Rising Bubbles". In: *Journal of Fluid Mechanics* 23.4 (1965), pp. 749–766.

[37] Q. Nie and G. Baker. "Application of adaptive quadrature to axi-symmetric vortex sheet motion". In: *Journal of Computational Physics* 143.1 (1998), pp. 49–69.

[38] M. Nitsche. "Axisymmetric vortex sheet motion: accurate evaluation of the principal value integral". In: *SIAM Journal on Scientific Computing* 21.3 (1999), pp. 1066–1084.

[39] M. Nitsche. "Singularity formation in a cylindrical and a spherical vortex sheet". In: *Journal of Computational Physics* 173.1 (2001), pp. 208–230.

[40] J. Nocedal and S. J. Wright. *Numerical Optimization.* New York: Springer, 1999.

[41] S. B. Pillapakkam et al. "Transient and steady state of a rising bubble in a viscoelastic fluid". In: *Journal of Fluid Mechanics* 589 (2007), pp. 215–252.

[42] L. Prandtl. "Zur berechnung der grenzschichten". In: *Journal of Applied Mathematics and Mechanics* 18.1 (1938), pp. 77–82.

[43] D. M. Sharaf et al. "Shapes and paths of an air bubble rising in quiescent liquids". In: *Physics of Fluids* 29.12 (2017), p. 122104.

[44] Y. Hou T, J. S. Lowengrub, and M. J. Shelley. "Removing the stiffness from interfacial flows with surface tension". In: *Journal of Computational Physics* 114.2 (1994), pp. 312–338.

[45] T. Erdélyi and A. P. Magnus and P. Nevai. "Generalized Jacobi weights, Christoffel functions, and Jacobi polynomials". In: *SIAM Journal on Mathematical Analysis* 25.2 (1994), pp. 602–614.

[46] L. N. Trefethen. *Approximation Theory and Approximation Practice.* Philadelphia: SIAM, 2019.

[47] M. K. Tripathi, K. C. Sahu, and R. Govindarajan. "Dynamics of an initially spherical bubble rising in quiescent liquid". In: *Nature Communications* 6.1 (2015), pp. 1–9.

[48] J. M. Vanden-Broeck. "Rising bubbles in a two-dimensional tube with surface tension". In: *The Physics of Fluids* 27.11 (1984), pp. 2604–2607.

[49] A. J. Wagner, L. Giraud, and C. E. Scott. "Simulation of a cusped bubble rising in a viscoelastic fluid with a new numerical method". In: *Journal of Fluid Mechanics* 129.1-3 (2000), pp. 227–232.

[50] J. Wilkening. "Harmonic stability of standing water waves". In: *Quarterly of Applied Math* 78.2 (2020), pp. 219–260.

[51] J. Wilkening and J. Yu. "Overdetermined shooting methods for computing standing water waves with spectral accuracy". In: *Computational Science & Discovery* 5.1 (2012), 014017:1–38.